Title

Cooperative carbon capture and steam regeneration with tetraamine-appended metal—organic frameworks

Journal
Science, 369(6502)

ISSN
0036-8075

Authors
Kim, Eugene J
Siegelman, Rebecca L
Jiang, Henry ZH
et al.

Publication Date
2020-07-24

DOI
10.1126/science.abb3976

Peer reviewed

Title: Cooperative carbon capture and steam regeneration with tetraamine-appended metal–organic frameworks

Authors: Eugene J. Kim,[1] Rebecca L. Siegelman,[1,6,†] Henry Z. H. Jiang,[1] Alexander C. Forse,[1,2,4,‡] Jung-Hoon Lee,[3,7,§] Jeffrey D. Martell,[1,¶] Phillip J. Milner,[1,∫] Joseph M. Falkowski,[8] Jeffrey B. Neaton,[3,5,7] Jeffrey A. Reimer,[2,6] Simon C. Weston,[8] Jeffrey R. Long[1,2,6,*]

Affiliations:

[1]Department of Chemistry, University of California, Berkeley, California 94720, United States

[2]Department of Chemical and Biomolecular Engineering, University of California, Berkeley, California 94720, United States

[3]Department of Physics, University of California, Berkeley, California 94720, United States

[4]Berkeley Energy and Climate Institute, University of California, Berkeley, California 94720, United States

[5]Kavli Energy Nanosciences Institute, University of California, Berkeley, California 94720, United States

[6]Materials Sciences Division, Lawrence Berkeley National Laboratory, Berkeley, CA 94720, United States

[7]Molecular Foundry, Lawrence Berkeley National Laboratory, Berkeley, CA 94720, United States

[8]Corporate Strategic Research, ExxonMobil Research and Engineering Company, Annandale, NJ 08801, United States

*Correspondence to: jrlong@berkeley.edu.

[†] Present address: DuPont de Nemours, Inc. 200 Powder Mill Rd, Wilmington, DE, 19803, United States

[‡] Present address: Department of Chemistry, University of Cambridge, Lensfield Road, Cambridge, CB2 1EW, United Kingdom

[§] Present address: Computational Science Research Center, Korea Institute of Science and Technology, Seoul 02792, Republic of Korea

[¶] Present address: Department of Chemistry, University of Wisconsin–Madison, Madison, WI, 53706, United States

[∫] Present address: Department of Chemistry and Chemical Biology, Cornell University, Ithaca, NY, 14853, United States

Abstract: Natural gas has become the dominant source of electricity in the United States, and technologies capable of efficiently removing CO_2 from natural gas-fired power plants emissions could reduce their emission intensity. However, given the low partial pressure of CO_2 in the flue stream, separation of CO_2 is particularly challenging. Taking inspiration from the crystal structures of diamine-appended metal–organic frameworks exhibiting two-step cooperative CO_2 adsorption, we report a family of robust tetraamine-functionalized frameworks that retain cooperativity, leading to the potential for exceptional efficiency in capturing CO_2 under the

extreme conditions relevant to natural gas flue emissions. The ordered, multimetal coordination of the tetraamines impart the materials with extraordinary stability to adsorption-desorption cycling with simulated humid flue gas and enable regeneration using low-temperature steam in lieu of costly pressure or temperature swings.

One Sentence Summary: Cooperative CO_2 adsorption under challenging conditions, together with steam regeneration, is achieved using tetraamine-functionalized metal–organic frameworks enabling novel CO_2 capture processes.

Carbon dioxide (CO_2) emissions from fossil fuel combustion and industrial processes account for as much as 65% of anthropogenic greenhouse gas emissions (*1-3*). Carbon capture and sequestration (CCS), wherein CO_2 is separated from the flue emissions of large point sources and permanently sequestered underground, is widely recognized as an essential component of strategies for meeting the ambitious climate targets established at the Paris Climate Conference (*4*). The development of capture technology has largely focused on coal flue emissions (*5*), but worldwide use of natural gas is projected to exceed that of coal by ~2032, necessitating the rapid development of CCS technology for natural gas emissions (*6*). The U.S. Department of Energy (DoE) has set an ambitious target of 90% capture of the CO_2 from natural gas flue streams (*7*), which is particularly challenging given that the CO_2 concentration in natural gas combined cycle (NGCC) emissions is typically only ~4%, compared to ~12 to 15% for coal emissions (*7*, *8*). Additionally, NGCC emissions contain high concentrations of O_2 (12.4%) and water (8.4%), and thus effective technologies must be stable and maintain CO_2 capture performance in the presence of these species (*7*, *9*).

Aqueous amine solutions, the most mature carbon capture technology to date (*10*), are susceptible to oxidative and thermal degradation and have low CO_2 cycling capacities (*11*). Porous solid adsorbents such as zeolites, silicas, and metal–organic frameworks are emerging as promising CO_2 capture materials because of their high surface areas, lower intrinsic regeneration energies, higher stabilities, and tunable surface chemistries (*12*, *13*). Taking inspiration from amine-functionalized silicas (*14*), we and others have shown that amine-functionalized metal–organic frameworks can capture CO_2 in the presence of water (*15*, *16*). A major consideration for adsorptive CO_2 capture from natural gas flue emissions is that the low partial pressure of CO_2 requires materials with high adsorption enthalpies. In turn, higher temperatures or lower pressures are needed to desorb captured CO_2, and these regeneration conditions are both costly and can substantially impact performance (*12*). The use of steam for CO_2 recovery has been proposed as a cost-effective strategy for amine-functionalized adsorbents (*17-22*), particularly because low-grade steam is inexpensive and readily available in most industrial processes. Unfortunately, engineering adsorbents with stability in the presence of steam is an ongoing issue (*19*, *23-25*).

We recently reported the promising CO_2 capture properties of the diamine-appended framework mmen–Mg_2(dobpdc) (mmen = *N*,*N*′-dimethylethylenediamine, dobpdc^{4-} = 4,4′-dioxidobiphenyl-3,3′-dicarboxylate) (Fig. 1A) (*26*). In this material, CO_2 adsorption proceeds through a cooperative mechanism in which the gas inserts into the Mg–N bonds to form chains of oxygen–bound carbamate species charge-balanced by neighboring ammonium groups running along the pores (*27*). This mechanism gives rise to unusual step-shaped CO_2 adsorption profiles and improved material CO_2 cycling capacities that can be achieved with smaller pressure or

temperature swings than are required for traditional adsorbents (*27*). The CO_2 capture properties can further be tuned by varying the appended diamine, leading to adsorbents with remarkable potential for CO_2 capture from coal flue gas emissions (Fig. 1B) (*28-31*) and even NGCC emissions (*32*).

Nonetheless, these materials are susceptible to diamine volatilization upon regeneration, which has limited their applicability in a practical capture processes (*30*). We now report that tetraamine-functionalized Mg_2(dobpdc) materials (Fig. 1C) exhibited high thermal stability and cooperatively captured CO_2 at concentrations as low as parts per million (ppm), enabled by a two-step ammonium carbamate chain-formation mechanism. The ordered, multimetal coordination mode achieved with the tetraamines dramatically increased the stability of these adsorbents and enables CO_2 desorption with inexpensive steam for the first time in amine-functionalized Mg_2(dobpdc).

Synthesis and structure of tetraamine-functionalized Mg_2(dobpdc)

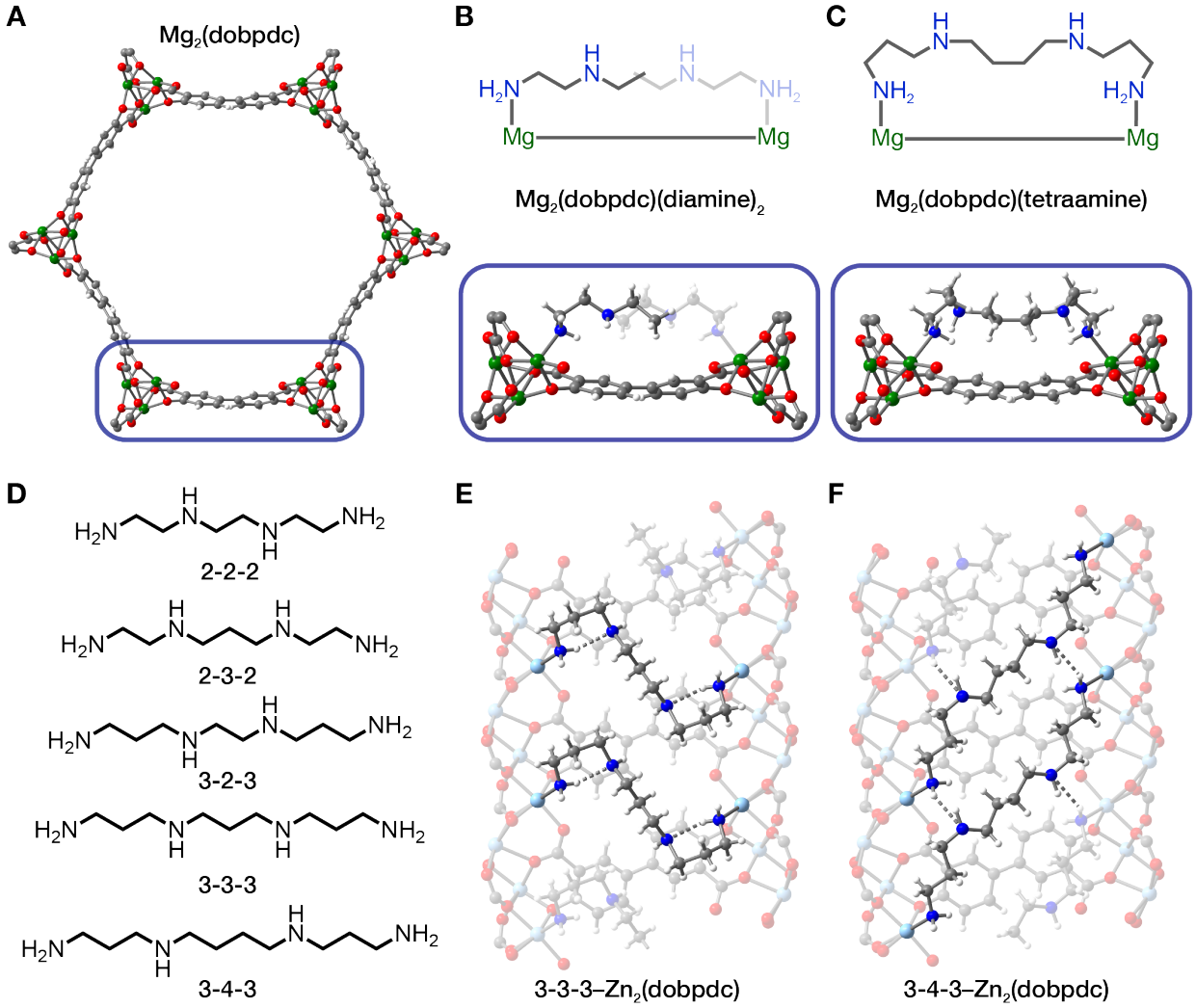

Fig. 1. Diamine versus tetraamine coordination in M_2(dobpdc). (**A**) Illustration of a hexagonal channel of Mg_2(dobpdc) viewed in the *ab*-plane, using single-crystal X-ray diffraction data for the isostructural framework Zn_2(dobpdc). (**B**) The diamine-functionalized material

features coordination of one diamine to each Mg^{2+} site (*28*) whereas (**C**) tetraamines can coordinate to two Mg^{2+} sites. (**D**) Tetraamines explored in this work and their abbreviations. (**E**,**F**) Single-crystal x-ray diffraction structures (100 K) of isostructural Zn_2(dobpdc) functionalized with 3-3-3 and 3-4-3 tetraamines, respectively. The tetraamines span metal centers across the pore that are 10.4637(11) Å apart (3-3-3) and 16.8312(19) Å apart (3-4-3). Green, light blue, gray, red, blue, and white spheres represent Mg, Zn, C, O, N, and H, respectively.

Our pursuit of tetraamine-functionalized Mg_2(dobpdc) was motivated by structural analysis of diamine-appended analogs, which indicated that tetraamines with chain lengths on the order of two *N*-alkylethylenediamines could bridge nearest neighbor metals across the pore (Fig. 1, B and C) (*28*). Such multiple metal coordination could yield adsorbents exhibiting cooperative CO_2 capture and greatly enhanced thermal and hydrolytic amine stability. Soaking Mg_2(dobpdc) with various tetraamines (Fig. 1D) in toluene (see the Supplementary Methods) produced loadings of ~1 tetraamine per Mg^{2+} site, or twice the desired 1:2 tetraamine:metal ratio (Fig. 1C), as determined by ^{1}H nuclear magnetic resonance (NMR) spectra of acid-digested samples. The desired loading could be achieved through subsequent thermal activation (see the Supplementary Methods and tables S1 and S2 and figs. S3 and S4). Thermogravimetric analysis indicated that the tetraamine-grafted Mg_2(dobpdc) materials were resistant to further diamine loss up to ~250 to 290°C (figs. S3 and S4). Here, we refer to the tetraamines using shorthand based on the number of carbon atoms in the alkyl groups bridging the amine moieties, for example *N,N′*-bis(3-aminopropyl)-1,3-diaminopropane and *N,N′*-bis(3-aminopropyl)-1,4-diaminobutane are referred to as 3-3-3 and 3-4-3, respectively (Fig. 1D).

Single-crystal x-ray diffraction (XRD) data obtained for 3-3-3 and 3-4-3-appended variants of the isostructural framework Zn_2(dobpdc) revealed that the tetraamines coordinate in a highly ordered fashion (Fig. 1, E and F). Tetraamine 3-3-3 bound two metal centers separated by a distance of 10.4637(11) Å (Fig. 1E) whereas 3-4-3 bridges metal sites were separated by 16.8312(19) Å (Fig. 1F). Longer tetraamines could ostensibly also be accommodated in the framework and bridge metal atoms at even greater distances. In 3-3-3-functionalized Zn_2(dobpdc), there was extensive intramolecular hydrogen bonding, whereas 3-4-3–Zn_2(dobpdc) primarily exhibited intermolecular hydrogen bonding between adjacent tetraamines along the pore direction. These experimental structures confirmed the tetraamine coordination mode in M_2(dobpdc) and accounted for the extremely high thermal stability of these materials (see below).

Adsorption properties and optimization for natural gas combined cycle post-combustion capture

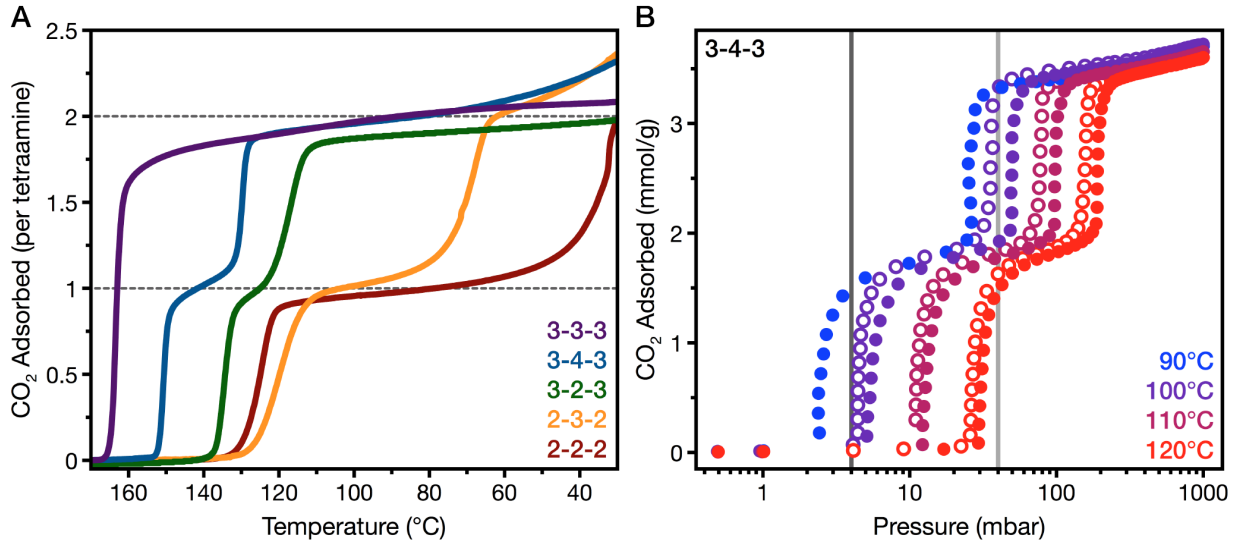

Fig. 2. CO_2 uptake in tetraamine-appended Mg_2(dobpdc). (A) Adsorption isobars obtained through thermogravimetric analysis of Mg_2(dobpdc)(tetraamine) under pure CO_2 at atmospheric pressure. Dashed lines indicate the theoretical capacities for binding of one and two CO_2 molecules per tetraamine. **(B)** Adsorption (filled circles) and desorption (open circles) isotherms for CO_2 uptake in Mg_2(dobpdc)(3-4-3) at 90°, 100°, 110°, and 120°C. The CO_2 pressures in an untreated NGCC flue emission stream (40 mbar) and following 90% capture (4 mbar) are indicated by light gray and dark gray lines, respectively.

Remarkably, all of the Mg_2(dobpdc)(tetraamine) variants exhibited sharp step-shaped CO_2 adsorption profiles consistent with cooperative adsorption and ammonium carbamate chain formation (Fig. 2 and figs. S14 to S16) (*27*, *28*, *30*, *32*). In each case, the CO_2 adsorption capacity at 30°C approached the theoretical capacity of two CO_2 molecules per tetraamine. Interestingly, with the exception of Mg_2(dobpdc)(3-3-3), the frameworks exhibited two-step adsorption profiles, with each step corresponding to half of the theoretical capacity. Analogous two-step adsorption profiles were previously observed in bulky diamine-appended variants of Mg_2(dobpdc) and was attributed to steric conflict between neighboring ammonium carbamate chains across the pore (*30*). In the case of tetraamine-appended Mg_2(dobpdc), we hypothesize that initial chemisorption of CO_2 occurred at one amine end, generating ammonium carbamates running along one vertex of the hexagonal pore. The formation of the second set of ammonium carbamate chains likely required reorientation of the unreacted, bound amines.

Consistent with this proposed mechanism, increasing tetraamine length coincides with a decrease in the material step separations up to 3-3-3, for which there is only a single adsorption step. Two-stepped adsorption returns in the case of slightly larger 3-4-3, which we attribute to this tetraamine likely bridging two metals at a longer distance than 3-3-3 and the other smaller tetraamines (Fig. 1E,F). Furthermore, when appended with triamines 3-3 (bis(3-aminopropyl)amine) and 3-4 (*N*-(3-aminopropyl)-1,4-diaminobutane), which can only form one set of ammonium carbamate chains, the Mg_2(dobpdc) frameworks exhibited CO_2 capacities that correspond to adsorption of one molecule of CO_2 for every two Mg^{2+} sites (figs. S12 and S13). For practical applications, a single-step adsorption profile, or a two-step adsorption with closely

spaced adsorption steps, is desirable to maximize the operating range over which the full material adsorption capacity can be accessed (*32*).

The temperature of the first adsorption step for Mg_2(dobpdc)(3-3-3) and Mg_2(dobpdc)(3-4-3) is 163° and 150°C, respectively. The temperatures are among the highest reported for any amine-appended variant of Mg_2(dobpdc) (*26*, *28-30*, *32*). Traditional adsorbents with Langmuir-type adsorption profiles typically show optimal performance at the lowest possible adsorption temperature, where the adsorption capacity is maximized. The high adsorption step temperatures for the tetraamine-appended materials directly correlated with adsorption steps at low pressures sufficient to enable 90% CO_2 capture from a NGCC flue stream (Fig. 2B and figs. S14 to S16) (*7*). For example, stepped CO_2 adsorption isotherm for Mg_2(dobpdc)(3-2-3) at 75°C indicated that the material should be able to reduce the CO_2 content in a NGCC flue stream to 0.4% (fig. S16). Additionally, our preliminary results (figs. S28 and S39) indicate that these materials may also be suitable for direct capture of CO_2 from air. While the majority of tetraamine-appended materials exhibit stable CO_2 cycling capacities, Mg_2(dobpdc)(3-3-3) shows a gradual decrease in CO_2 cycling capacity over time (fig. S10), thus Mg(dobpdc)(3-4-3) was chosen for further study due to its practical step position and fundamentally interesting two-step adsorption behavior.

The adsorption data for Mg_2(dobpdc)(3-4-3) suggested that in a post-combustion capture process from NGCC flue emissions, this framework could achieve a 90% CO_2 capture rate, referring to the removal of CO_2 to a residual concentration of 10% that of the feed (reduction from 40 mbar to 4 mbar at atmospheric pressure). Single-component isotherms collected between 90° and 120°C reveal that step-shaped CO_2 capture at 4 mbar (corresponding to 90% capture) was retained up to 90°C under dry conditions (Fig. 2B). Using the Clausius-Clapeyron relationship, we calculated differential adsorption enthalpy (Δh_{ads}) and entropy (Δs_{ads}) values of 99 ± 3 kJ/mol and 223 ± 8 J/mol·K, respectively, at a loading of 1 mmol CO_2/g (figs. S19 and S20). These values followed a correlation previously observed between Δh_{ads} and Δs_{ads} values determined for diamine-appended Mg_2(dobpdc) (fig. S21) (*28*). The Δh_{ads} value for Mg_2(dobpdc)(3-4-3) is among the highest reported for amine-functionalized materials. Such a high enthalpy of adsorption should enable CO_2 capture at high temperatures and result in lower energy consumption in a temperature-swing adsorption process by minimizing the required temperature swing (*33-37*). Additionally, Mg_2(dobpdc)(3-4-3) exhibited minimal adsorption-desorption hysteresis at atmospheric pressure (fig. S11).

Cooperative adsorption mechanism

We used in situ infrared (IR) and solid-state NMR spectroscopies to characterize Mg_2(dobpdc)(3-4-3) before and after CO_2 adsorption to investigate the two-step cooperative adsorption mechanism. In situ diffuse reflectance IR spectroscopy (DRIFTS) characterization of the framework in the presence of CO_2 revealed a characteristic carbamate C–N stretch at 1339 cm^{-1} and a C–O stretch at 1689 cm^{-1} (see isotopic difference spectrum, Fig. 3A) (*27-30*). In addition, spectra collected simultaneously with a volumetric, equilibrium CO_2 isotherm at 120°C indicated that the ammonium carbamate species was responsible for cooperative adsorption. Distinct features corresponding to hydrogen bonding between neighboring ammonium carbamate chains were observed in the N–H regions of the difference spectrum (3300 to 3000 and 3500 to 3400 cm^{-1}) and distinct hydrogen bonding environments were characterized for each of the two adsorption steps (fig. S26).

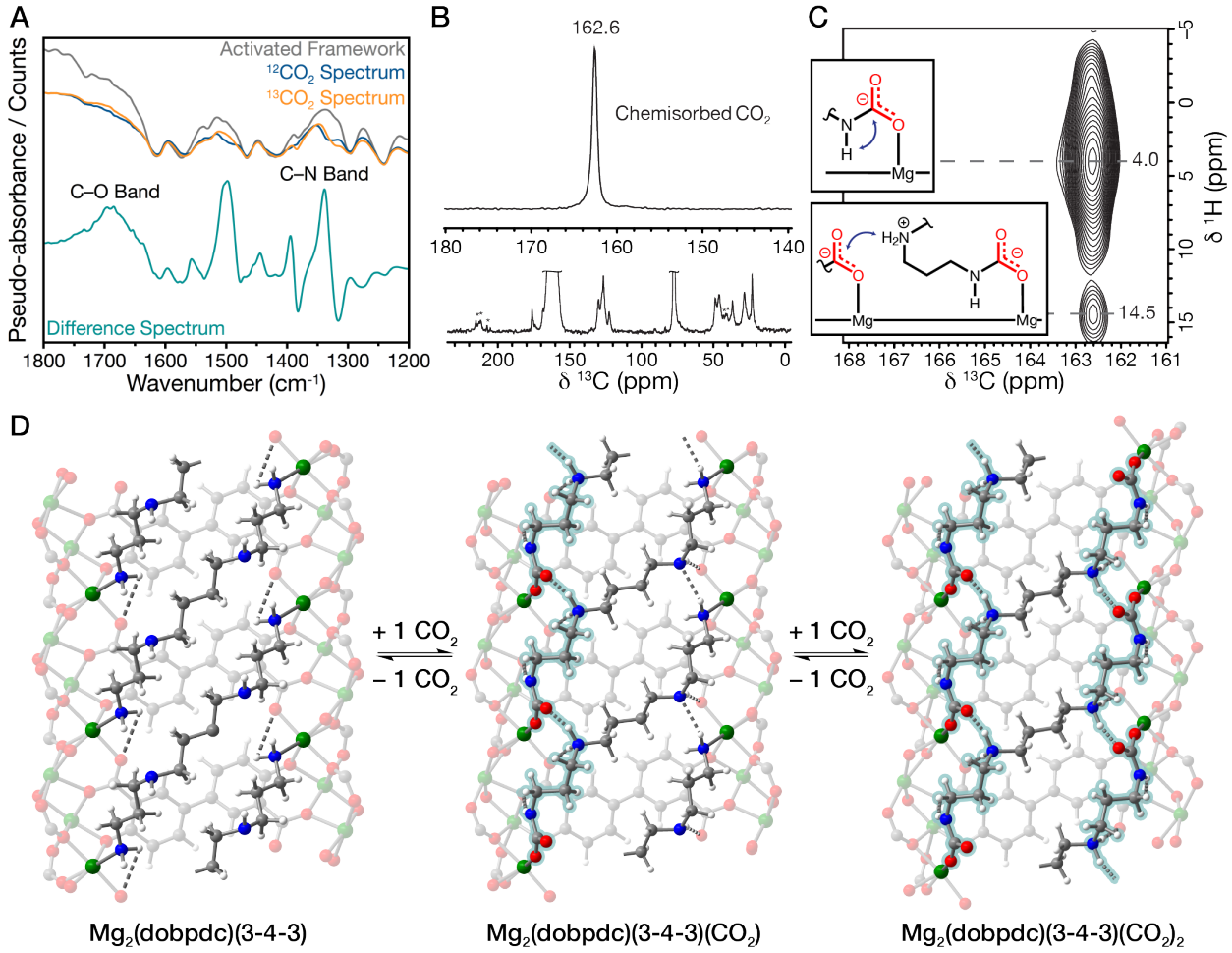

Fig. 3. Spectroscopic investigation of CO_2 adsorption in Mg_2(dobpdc)(3-4-3). (**A**) Raw in situ DRIFTS spectra of activated 3-4-3–Mg_2(dobpdc) (grey curve), 3-4-3–Mg_2(dobpdc) dosed with 400 mbar of $^{12}CO_2$ and $^{13}CO_2$ at 120°C (dark blue and yellow curves, respectively), and the isotopic difference spectrum (light blue curve). The $^{13}CO_2$ spectrum was used as a baseline, isolating vibrations caused by inserted CO_2. Vibrations corresponding to diagnostic carbamate bands are labeled. (**B**) Room-temperature ^{13}C solid-state magic angle spinning NMR (16.4 T) of Mg_2(dobpdc)(3-4-3) dosed with 1038 mbar of $^{13}CO_2$. The resonance at 162.6 ppm was assigned as carbamate. (**C**) $^{1}H \rightarrow ^{13}C$ heteronuclear correlation (contact time 100 μs) spectrum and correlation assignments. (**D**) Predicted structures of Mg_2(dobpdc)(3-4-3), Mg_2(dobpdc)(3-4-3)(CO_2), and Mg_2(dobpdc)(3-4-3)$(CO_2)_2$ obtained from structural relaxations with vdW-corrected DFT. Green, grey, red, blue, and white spheres represent Mg, C, O, N, and H atoms, respectively.

Corroborating evidence for ammonium carbamate formation was obtained from magic angle spinning solid-state NMR experiments. A single carbamate resonance was observed at 162.6 parts per million in the ^{13}C NMR spectrum of Mg_2(dobpdc)(3-4-3) dosed with 1.04 bar of $^{13}CO_2$ (Fig. 3B), which coincides with resonances reported previously for ammonium carbamate formed upon $^{13}CO_2$ adsorption in diamine-appended Mg_2(dobpdc) (*38*). The presence of a single carbamate feature suggested that all of the chemisorbed CO_2 was in the same chemical environment after adsorption at 1 bar. We also observed five resonances for the tetraamine alkyl

carbons, supporting a symmetric reaction between the tetraamine and CO_2 at full capacity (Fig. 3B). Two-dimensional heteronuclear correlation data further revealed that CO_2 reacted with the primary amine and that a secondary ammonium group formed nearby the carbamate (Fig. 3C) (*38*), and solid-state ^{15}N NMR data confirmed the symmetric formation of ammonium and carbamate species (fig. S27). The NMR and IR results confirmed that our tetraamine-functionalized Mg_2(dobpdc) variants operated through the envisaged two-step cooperative adsorption mechanism.

The structures of Mg_2(dobpdc)(3-4-3) after adsorption of CO_2 to half and full capacity were further investigated using van der Waals (vdW)-corrected density functional theory (DFT) calculations (Fig. 3D). Lattice parameters obtained from high-resolution powder XRD diffraction experiments under vacuum and after exposure to 1 bar CO_2 were used as starting points for structural relaxations (fig. S29 and table S4). The computed binding energies (ΔE_{ads}) for the structures are within ±10 kJ/mol of the corresponding experimental Δh_{ads} values (table S7) (*38*). At full CO_2 capacity (i.e., two molecules of CO_2 per tetraamine), our calculations support two-step cooperative insertion of CO_2, and the calculated NMR chemical shifts for this structure are in good agreement with the experimental values (table S8) (*38*). The computed ΔE_{ads} values indicate that the half capacity structure was more stable than the full capacity structure, which further supports our proposed two-step cooperative adsorption mechanism. In addition, the tetraamines in our optimized structure of activated Mg_2(dobpdc)(3-4-3) bridge the same set of metals spanning ~16.7 Å in the *ab*-plane of the framework, consistent with the single-crystal structure of Zn_2(dobpdc)(3-4-3). Comparing the activated and full CO_2 capacity structures to synchrotron PXRD patterns by Rietveld analysis show reasonable fits (figs. S32 and S33 and table S9). Taken together, our results from XRD, NMR, IR, and DFT data indicate that tetraamine-functionalized frameworks indeed enhance cooperative CO_2 adsorption relative to diamine-appended materials.

Carbon capture from flue gas with steam desorption

Because flue gas streams are saturated with water, any candidate carbon capture material must be able to adsorb CO_2 under humid conditions. When exposed to CO_2 streams with ~2.6% H_2O (see Supplementary Methods) (*32*), Mg_2(dobpdc)(3-4-3) again exhibited step-shaped isobars, with steps shifted to higher temperatures relative to those under dry CO_2 (fig. S40) as has been reported previously for diamine-appended Mg_2(dobpdc) (*29*, *30*, *32*). Notably, this temperature shift indicated that water enhanced CO_2 binding in the material and should promote CO_2 capture from a flue gas stream (*29*, *30*, *32*). Furthermore, essentially no changes in the CO_2 adsorption profile and capacity were observed after the material was held under flowing air at 100°C for 12 h, indicating the stability of the framework to oxygen in the flue gas stream (fig. S43).

We also performed larger scale breakthrough experiments at 100°C under the same humid conditions to simulate a real fixed-bed adsorption process. Under these conditions, Mg_2(dobpdc)(3-4-3) exhibited a high CO_2 capture rate of 90% with a breakthrough capacity of 2.0±0.2 mmol/g (Fig. 4A and figs. S45 to S48). It also exhibited minimal tetraamine volatilization during the course of 1000 CO_2 adsorption-desorption cycles performed under humid conditions using a thermogravimetric analyzer, and the material remains crystalline with a stable cycling capacity of 13.6 g/100 g (Fig. 4B and fig. S50 and S51). Thus, Mg_2(dobpdc)(3-4-3) could cycle a large quantity of CO_2 while meeting the U.S. DoE target for capturing 90% of the CO_2 from natural gas flue emissions (*7*).

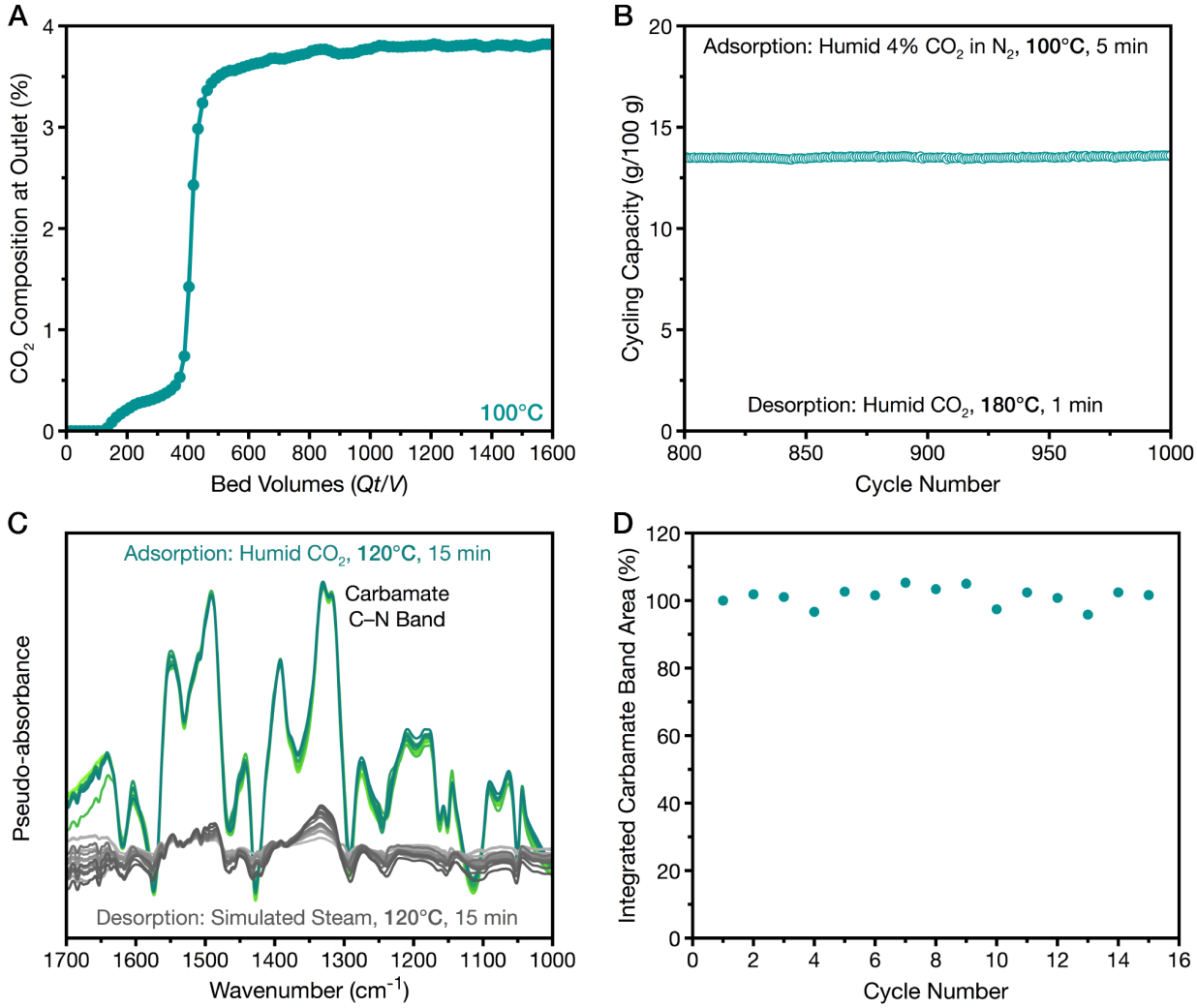

Fig. 4. CO_2 adsorption in Mg_2(dobpdc)(3-4-3) in the presence of water. (**A**) CO_2 breakthrough profile for Mg_2(dobpdc)(3-4-3) under simulated humid (~2.6% H_2O) natural gas flue gas (4% CO_2 in N_2) at 100°C and atmospheric pressure. (**B**) Extended temperature-swing cycling of Mg_2(dobpdc)(3-4-3) carried out using a thermogravimetric analyzer at atmospheric pressure. Adsorption conditions: humid (~2.6% H_2O) 4% CO_2 in N_2 for 5 min at 100°C; desorption conditions: humid (~2.6% H_2O) CO_2 stream at 180°C for 1 min. (**C**) Infrared spectra showing 15 cycles of adsorption under humid CO_2 (bright green spectra) and desorption under simulated steam (light grey spectra, estimated 51 to 65% water content, balance N_2). Increasingly darker colored curves indicate progressive cycles. Spectra of the activated framework under flowing steam/N_2 were used as a baseline. (**D**) Plot of the integrated area for the carbamate band in **C** (~1290–1360 cm^{-1}) versus adsorption cycle number, illustrating stable formation of the carbamate species across 15 cycles.

The high breakthrough capacity and exceptional stability of Mg_2(dobpdc)(3-4-3) motivated us to explore the use of steam in place of heating at 180°C to desorb CO_2 from the material. Low-grade steam could offer advantages over both temperature swing and pressure

swing adsorption processes for post-combustion CO_2 capture (*17-22*). The viability of using steam for CO_2 desorption was tested in a custom-built flow-through cell for in situ DRIFTS equipped to cycle between flowing humid CO_2 and simulated steam (estimated 51 to 65% water content, balance N_2, see table S10) at 120°C and ~1 atm (Fig. 4C,D). The IR spectra collected for Mg_2(dobpdc)(3-4-3) over the course of 15 cycles showed repeated growth and disappearance of both the ammonium (2800–1800 cm^{-1}) and C–N (1339 cm^{-1}) bands associated with carbamate chain formation, indicating the stability of the cooperative insertion mechanism to steam regeneration conditions. Postcycling isobaric analysis of the material revealed that step-shaped adsorption was retained to a high capacity (~16.6 g/100, see figs. S52 to S55 and table S11), and ^{1}H NMR analysis revealed that the tetraamine loading remained unchanged (table S12). In stark contrast, the representative diamine-appended material Mg_2(dobpdc)(e-2)$_2$ (e-2 = *N*-ethylethylenediamine) (*28*, *30*) exhibited substantial amine volatilization after only a single steam desorption cycle (table S13 and fig. S56). The impressive performance of Mg_2(dobpdc)(3-4-3) underscores the stabilization afforded by the multimetal coordination modes.

Outlook

We have developed a class of tetraamine-functionalized metal–organic frameworks that exhibit cooperative CO_2 adsorption and greatly enhanced stability compared to previous diamine-functionalized materials as a result of multiple, ordered metal–amine interactions. Critically, the nature of amine coordination in these materials gives rise to two-step adsorption of CO_2 and large adsorption enthalpies suitable for CO_2 capture from simulated natural gas flue streams. The top-performing material, Mg_2(dobpdc)(3-4-3), achieved a large CO_2 adsorption capacity of 2.0 ± 0.2 mmol/g in the presence of water while meeting the DoE target for 90% CO_2 capture from natural gas flue emissions. Most strikingly, however, the enhanced stability of these tetraamine-functionalized frameworks enables regeneration using direct steam contact, a pathway that could afford significant energy savings compared to traditional processes. Overall, the molecular-level design strategy implemented here represents a step-change in the industrial viability of adsorption-based CO_2 capture from natural gas flue emissions, a separation of growing importance in the global energy landscape.

References and Notes:

1. IPCC, "Climate Change 2013 - The physical science basis" (Cambridge University Press, Cambridge, United Kingdom and New York, NY, USA, 2013).
2. IPCC, "Climate change 2014: mitigation of climate change" (Cambridge University Press, Cambridge, United Kingdom and New York, NY, USA, 2014).
3. International Energy Agency, "CO_2 emissions from fuel combustion highlights" (2016), pp. 1–166.
4. M. Bui, C. S. Adjiman, A. Bardow, E. J. Anthony, A. Boston, S. Brown, P. S. Fennel, S. Fuss, A. Galindo, L. A. Hackett, J. P. Hallett, H. J. Herzog, G. Jackson, J. Kemper, S. Krevor, G. C. Maitland, M. Matuszewski, I. S. Metcalf, C. Petit, G. Puxty, J. Reimer, D. M. Reiner, E. S. Rubin, S. A. Scott, N. Shah, B. Smit, J. P. M. Trusler, P. Webley, J. Wilcox, N. M. Dowell, Carbon capture and storage (CCS): the way forward. *Energy Environ. Sci.* **11**, 1062–1176 (2018).
5. R. L. Siegelman, P. J. Milner, E. Kim, S. C. Weston, J. R. Long, Challenges and opportunities for adsorption-based CO_2 capture from natural gas combined cycle emissions. *Energy Environ. Sci.* **26**, 2161–2173 (2019).
6. U.S. Energy Information Administration, "International energy outlook 2019" (2019), pp. 1–85.
7. U.S. Department of Energy, National Energy Technology Laboratory, "Cost and performance baseline for fossil energy plants. Volume 1a: bituminous coal (PC) and natural gas to electricity. Revision 3" (2015).
8. E. S. Rubin, H. Zhai, The cost of carbon capture and storage for natural gas combined cycle power plants. *Environ. Sci. Technol.* **46**, 3076–3084 (2012).
9. U.S. Department of Energy, "Carbon capture opportunities for natural gas fired power systems" (2017), pp. 1–5.
10. G. T. Rochelle, Amine scrubbing for CO_2 capture. *Science*. **325**, 1652–1654 (2009).
11. S. A. Mazari, B. Si Ali, B. M. Jan, I. M. Saeed, S. Nizamuddin, An overview of solvent management and emissions of amine-based CO_2 capture technology. *Int J Greenh Gas Con*. **34**, 129–140 (2015).
12. T. C. Drage, C. E. Snape, L. A. Stevens, J. Wood, J. Wang, A. I. Cooper, R. Dawson, X. Guo, C. Satterley, R. Irons, Materials challenges for the development of solid sorbents for post-combustion carbon capture. *J. Mater. Chem.* **22**, 2815–2823 (2012).
13. H. Furukawa, K. E. Cordova, M. O'Keeffe, O. M. Yaghi, The chemistry and applications of metal–organic frameworks. *Science*. **341**, 1230444 (2013).
14. P. Bollini, S. A. Didas, C. W. Jones, Amine-oxide hybrid materials for acid gas separations. *J. Mater. Chem.* **21**, 15100–15120 (2011).
15. J. A. Mason, T. M. McDonald, T.-H. Bae, J. E. Bachman, K. Sumida, J. J. Dutton, S. S. Kaye, J. R. Long, Application of a high-throughput analyzer in evaluating solid adsorbents for post-combustion carbon capture via multicomponent adsorption of CO_2, N_2, and H_2O. *J. Am. Chem. Soc.* **137**, 4787–4803 (2015).
16. Y. Lin, C. Kong, L. Chen, Amine-functionalized metal–organic frameworks: structure, synthesis and applications. *RSC Adv.* **6**, 32598–32614 (2016).
17. W. Chaikittisilp, H.-J. Kim, C. W. Jones, Mesoporous alumina-supported amines as potential steam-stable adsorbents for capturing CO_2 from simulated flue gas and ambient air. *Energy Fuels*. **25**, 5528–5537 (2011).
18. R. Numaguchi, J. Fujiki, H. Yamada, F. A. Chowdhury, K. Kida, K. Goto, T. Okumura,

K. Yoshizawa, K. Yogo, Development of post-combustion CO_2 capture system using amine-impregnated solid sorbent. *Energy Procedia*. **114**, 2304–2312 (2017).
19. W. Li, S. Choi, J. H. Drese, M. Hornbostel, G. Krishnan, P. M. Eisenberger, C. W. Jones, Steam-stripping for regeneration of supported amine-based CO_2 adsorbents. *ChemSusChem*. **3**, 899–903 (2010).
20. E. S. Sanz-Pérez, C. R. Murdock, S. A. Didas, C. W. Jones, Direct capture of CO_2 from ambient air. *Chem. Rev.* **116**, 11840–11876 (2016).
21. A. R. Kulkarni, D. S. Sholl, Analysis of equilibrium-based TSA processes for direct capture of CO_2 from air. *Ind. Eng. Chem. Res.* **51**, 8631–8645 (2012).
22. C. Kim, H. S. Cho, S. Chang, S. J. Cho, M. Choi, An ethylenediamine-grafted Y zeolite: a highly regenerable carbon dioxide adsorbent via temperature swing adsorption without urea formation. *Energy Environ. Sci.*, **9**, 1803–1811 (2015).
23. M. Jahandar Lashaki, S. Khiavi, A. Sayari, Stability of amine-functionalized CO_2 adsorbents: a multifaceted puzzle. *Chem. Soc. Rev.* **119**, 3962–86 (2019).
24. D. Andirova, Y. Lei, X. Zhao, S. Choi, Functionalization of metal–organic frameworks for enhanced stability under humid carbon dioxide capture conditions. *ChemSusChem*. **8**, 3405–3409 (2015).
25. N. C. Burtch, H. Jasuja, K. S. Walton, Water stability and adsorption in metal–organic frameworks. *Chem. Rev.* **114**, 10575–10612 (2014).
26. T. M. McDonald, W. R. Lee, J. A. Mason, B. M. Wiers, C. S. Hong, J. R. Long, Capture of carbon dioxide from air and flue gas in the alkylamine-appended metal–organic framework mmen-Mg_2(dobpdc). *J. Am. Chem. Soc.* **134**, 7056–7065 (2012).
27. T. M. McDonald, J. A. Mason, X. Kong, E. D. Bloch, D. Gygi, A. Dani, V. Crocellà, F. Giordanino, S. O. Odoh, W. S. Drisdell, B. Vlaisavljevich, A. L. Dzubak, R. Poloni, S. K. Schnell, N. Planas, K. Lee, T. Pascal, L. F. Wan, D. Prendergast, J. B. Neaton, B. Smit, J. B. Kortright, L. Gagliardi, S. Bordiga, J. A. Reimer, J. R. Long, Cooperative insertion of CO_2 in diamine-appended metal–organic frameworks. *Nature*. **519**, 303–308 (2015).
28. R. L. Siegelman, T. N. McDonald, M. I. Gonzalez, J. D. Martell, P. J. Milner, J. A. Mason, A. H. Berger, A. S. Bhown, J. R. Long, Controlling cooperative CO_2 adsorption in diamine-appended Mg_2(dobpdc) metal–organic frameworks. *J. Am. Chem. Soc.* **139**, 10526–10538 (2017).
29. P. J. Milner, R. L. Siegelman, A. C. Forse, M. I. Gonzalez, T. Runčevski, J. D. Martell, J. A. Reimer, J. R. Long, A diaminopropane-appended metal–organic framework enabling efficient CO_2 capture from coal flue gas via a mixed adsorption mechanism. *J. Am. Chem. Soc.* **139**, 13541–13553 (2017).
30. P. J. Milner, J. D. Martell, R. L. Siegelman, D. Gygi, S. C. Weston, J. R. Long, Overcoming double-step CO_2 adsorption and minimizing water co-adsorption in bulky diamine-appended variants of Mg_2(dobpdc). *Chem. Sci*. **9**, 160–174 (2018).
31. J. H. Choe, D. W. Kang, M. Kang, H. Kim, J. R. Park, D. W. Kim, C. S. Hong, Revealing an unusual temperature-dependent CO_2 adsorption trend and selective CO_2 uptake over water vapors in a polyamine-appended metal–organic framework. *Mater. Chem. Front.* **48**, 2783 (2019).
32. R. L. Siegelman, P. J. Milner, A. C. Forse, J.-H. Lee, K. A. Colwell, J. B. Neaton, J. A. Reimer, S. C. Weston, J. R. Long, Water enables efficient CO_2 capture from natural gas flue emissions in an oxidation-resistant diamine-appended metal–organic framework. *J.*

Am. Chem. Soc. **141**, 13171–13186 (2019).
33. L. Joss, M. Gazzani, M. Hefti, D. Marx, M. Mazzotti, Temperature swing adsorption for the recovery of the heavy component: an equilibrium-based shortcut model. *Ind. Eng. Chem. Res.* **54**, 3027–3038 (2015).
34. L. Joos, K. Lejaeghere, J. M. Huck, V. Van Speybroeck, B. Smit, Carbon capture turned upside down: high-temperature adsorption & low-temperature desorption (HALD). *Energy Environ. Sci.* **8**, 2480–2491 (2015).
35. M.-W. Yang, N.-C. Chen, C.-H. Huang, Y.-T. Shen, H.-S. Yang, C.-T. Chou, Temperature swing adsorption process for CO_2 capture using polyaniline solid sorbent. *Energy Procedia*. **63**, 2351–2358 (2014).
36. A. Lee, G. Xiao, P. Xiao, K. Joshi, R. Singh, P. A. Webley, High temperature adsorption materials and their performance for pre-combustion capture of carbon dioxide. *Energy Procedia*. **4**, 1199–1206 (2011).
37. X. P. Wang, J. J. Yu, J. Cheng, Z. P. Hao, Z. P. Xu, High-temperature adsorption of carbon dioxide on mixed oxides derived from hydrotalcite-like compounds. *Environ. Sci. Technol.* **42**, 614–618 (2008).
38. A. C. Forse, P. J. Milner, J.-H. Lee, H. N. Redfearn, J. Oktawiec, R. L. Siegelman, J. D. Martell, B. Dinakar, L. B. Porter-Zasada, M. I. Gonzalez, J. B. Neaton, J. R. Long, J. A. Reimer, Elucidating CO_2 Chemisorption in diamine-appended metal–organic Frameworks. *J. Am. Chem. Soc.* **140**, 18016–18031 (2018).
39. Bruker Analytical X-ray Systems Inc., SAINT, APEX2, and APEX3 Software for CCD Diffractometers.
40. G. M. Sheldrick, SADABS; University of Göttingen: Göttingen, Germany (1996).
41. G. M. Sheldrick, SHELXT - Integrated space-group and crystal-structure determination. *Acta Cryst. A.* **71**, 3–8 (2015).
42. G. M. Sheldrick, Crystal structure refinement with SHELXL. *Acta Cryst. C.* **71**, 3–8 (2015).
43. O. V. Dolomanov, L. J. Bourhis, R. J. Gildea, J. A. K. Howard, H. Puschmann, OLEX2: a complete structure solution, refinement and analysis program. *J. Appl. Crystallogr.* **42**, 339–341 (2009).
44. S. Øien-Ødegaard, G. C. Shearer, D. S. Wragg, K. P. Lillerud, Pitfalls in metal–organic framework crystallography: towards more accurate crystal structures. *Chem. Soc. Rev.* **50**, 4867–4876 (2017).
45. S. Lee, H.-B. Bürgi, S. A. Alshmimri, O. M. Yaghi, Impact of disordered guest–framework interactions on the crystallography of metal–organic frameworks. *J. Am. Chem. Soc*. **140**, 8958–8964 (2018).
46. A. Coelho, Topas Academic v4.1 (2007).
47. March, A. Mathematische Theorie Der Regelung Nach Der Korngestah Bei Affiner Deformation. *Z. Kristallogr. Cryst. Mater.* **81**, 285–297 (1932).
48. Dollase, W. A. Correction of Intensities for Preferred Orientation in Powder Diffractometry: Application of the March Model. *J. Appl. Crystallogr.* **19**, 267–272 (1986).
49. P. E. Blöchl, Projector augmented-wave method. *Phys. Rev. B*. **50**, 17953 (1994).
50. G. Kresse, D. Joubert, From ultrasoft pseudopotentials to the projector augmented-wave method. *Phys. Rev. B*. **59**, 1758–1775 (1999).
51. G. Kresse, J. Furthmüller, Efficient iterative schemes for ab initio total-energy calculations

using a plane-wave basis set. *Phys. Rev. B*. **54**, 11169–11186 (1996).
52. G. Kresse, J. Furthmüller, Efficiency of ab-initio total energy calculations for metals and semiconductors using a plane-wave basis set. *Comput. Mater. Sci.* **6**, 15–50 (1996).
53. G. Kresse, J. Hafner, Ab initio molecular-dynamics simulation of the liquid-metal--amorphous-semiconductor transition in germanium. *Phys. Rev. B*. **49**, 14251–14269 (1994).
54. K. Lee, É. D. Murray, L. Kong, B. I. Lundqvist, D. C. Langreth, Higher-accuracy van der Waals density functional. *Phys. Rev. B*. **82**, 081101 (2010).
55. C. Elsässer, M. Fähnle, C. T. Chan, K. M. Ho, Density-functional energies and forces with Gaussian-broadened fractional occupations. *Phys. Rev. B*. **49**, 13975–13978 (1994).
56. C. T. Campbell, J. R. V. Sellers, Enthalpies and entropies of adsorption on well-defined oxide surfaces: experimental measurements. *Chem. Rev.* **113**, 4106–4135 (2012).
57. F. G. Helfferich, P. W. Carr, Non-Linear Waves in Chromatography. *J. Chromatogr. A*. **629**, 97–122 (1993).
58. W. Zhang, Y. Shan, A. Seidel-Morgenstern, Breakthrough Curves and Elution Profiles of Single Solutes in Case of Adsorption Isotherms with Two Inflection Points. *J. Chromatogr. A*. **1107**, 216–225 (2006).
59. M. Mazzotti, A. Rajendran, Equilibrium Theory-Based Analysis of Nonlinear Waves in Separation Processes. *Annu. Rev. Chem. Biomol. Eng.* **4**, 119–141 (2013).
60. M. Hefti, L. Joss, Z. Bjelobrk, M. Mazzotti, On the Potential of Phase-Change Adsorbents for CO_2 Capture by Temperature Swing Adsorption. *Faraday Discuss.* **192**, 153–179 (2016).
61. R. R. Krug, W. G. Hunter, R. A. Grieger, Statistical interpretation of enthalpy–entropy compensation. *Nature*. **261**, 566–567 (1976).

Acknowledgements:
We thank the Philomathia Foundation and Berkeley Energy and Climate Institute for support of A.C.F. through a postdoctoral fellowship. J.-H.L.'s work was supported by the KIST Institutional Program (Project No. 2E29910). We thank the Miller Institute for Basic Research in Science for postdoctoral fellowship support of J.D.M. We thank the National Institute of General Medical Science of the National Institutes of Health for a postdoctoral fellowship for P.J.M. (F32GM120799). We thank Halle N. Redfearn for carrying out initial NMR measurements on tetraamine-functionalized metal–organic frameworks, Dr. Hiroyasu Furukawa and Dr. Julia Oktawiec for helpful discussions, and Dr. Katie R. Meihaus for editorial assistance. **Funding:** We acknowledge ExxonMobil Research and Engineering Company for financial support of this work. The crystallographic studies of Zn_2(dobpdc) were carried out at the Advanced Light Source at Lawrence Berkeley National Laboratory, a user facility supported by the Director, Office of Science, Office of Basic Energy Sciences, of the DoE under Contract No. DE-AC02-05CH11231. Synchrotron powder X-ray diffraction data were collected on the 17-BM-B Beamline at the Advanced Photon Source, a U.S. Department of Energy Office of Science User Facility operated by Argonne National Laboratory. Use of the Advanced Photon Source at Argonne National Laboratory was supported by the U.S. Department of Energy, Office of Science, Office of Basic Energy Sciences, under Contract No. DE-AC02-06CH11357. Work at the Molecular Foundry was supported by the Office of Science, Office of Basic Energy Sciences, U.S. Department of Energy, under Contract DE-AC02-05CH11231. Additional computational resources were provided by the Department of Energy (NERSC). This research also used the

Savio computational cluster resource provided by the Berkeley Research Computing program at the University of California, Berkeley. **Author contributions:** E.J.K., R.L.S., J.D.M., P.J.M., J.M.F., S.C.W. and J.R.L. formulated the project. E.J.K. synthesized the materials. E.J.K. collected and analyzed the gas adsorption data. R.L.S. and E.J.K. collected and analyzed the single-crystal X-ray diffraction data. H.Z.H.J. and E.J.K. collected and analyzed the infrared spectra. A.C.F. and E.J.K. collected and analyzed the NMR spectra. J.-H.L. collected and analyzed the computational data. H.Z.H.J. collected and analyzed the powder X-ray diffraction data. R.L.S. collected and analyzed the breakthrough data. H.Z.H.J. and E.J.K. collected and analyzed the steam desorption cycling data. E.J.K. and J.R.L. wrote the manuscript and all authors contributed to revising the manuscript. **Competing interests:** The authors declare the following competing financial interest(s): J.R.L. has a financial interest in and serves on the board of directors of Mosaic Materials, Inc., a start-up company working to commercialize metal−organic frameworks for gas separations. S.C.W., J.M.F., J.R.L., E.J.K., R.L.S., J.D.M., and P.J.M. are inventors on patent application US16/175,708 (International: PCT/US2018/058287) held/submitted by the University of California, Berkeley and ExxonMobil Research and Engineering Co. that covers polyamine-appended metal–organic frameworks for carbon dioxide separations. **Disclaimers:** The content is solely the responsibility of the authors and does not necessarily represent the official views of the National Institutes of Health. **Data and materials availability:** The supplementary materials contain complete experimental and spectral details for all new compounds reported herein. Crystallographic data will be made available free of charge from the Cambridge Crystallographic Data Centre under reference numbers CCDC 1996313 and 1996314.

Supplementary Materials:

Materials and Methods

Figures S1-S56

Tables S1-S14

References (*39-61*)

Science
AAAS

Supplementary Materials for

Cooperative carbon capture and steam regeneration with tetraamine-appended metal–organic frameworks

Eugene J. Kim, Rebecca L. Siegelman, Henry Z. H. Jiang, Alexander C. Forse, Jung-Hoon Lee, Jeffrey D. Martell, Phillip J. Milner, Joseph M. Falkowski, Jeffrey B. Neaton, Jeffrey A. Reimer, Simon C. Weston, Jeffrey R. Long*

Correspondence to: jrlong@berkeley.edu

This PDF file includes:

Materials and Methods
Figs. S1 to S56
Tables S1 to S14
References (*39-61*)

Materials and Methods

General procedures. All reagents and solvents were purchased from commercial sources and used as received. The ligand H_4dobpdc was purchased from Hangzhou Trylead Chemical Technologies Co. The metal–organic framework Mg_2(dobpdc) was synthesized following the literature procedure (*29*). The 77 K N_2 isotherm and powder X-ray diffraction pattern of Mg_2(dobpdc) (Figures S1 and S2 below) are consistent with those reported in the literature. Infrared spectra were collected on a PerkinElmer Avatar Spectrum 400 FTIR spectrometer with a Pike attenuated total reflectance accessory. Powder X-ray diffraction data were obtained on a Bruker D8-Advance diffractometer using Cu Kα (λ = 1.5406 Å) radiation unless noted otherwise. ^{1}H NMR spectra were collected on a Bruker AV-300 spectrometer at ambient temperature and all chemical shifts are given in relation to residual solvent peaks or tetramethylsilane. Tetraamine-appended M_2(dobpdc) was digested using dimethyl sulfoxide-d_6 and deuterium chloride solution (35 wt % in D_2O). Tetraamine loadings were determined by comparing ^{1}H NMR integrations of framework ligand peaks to the amine peaks.

Synthesis of Tetraamine-Appended Mg_2(dobpdc). The following procedure was used for each tetraamine analogue. A 20 mL scintillation vial was charged with a 20% v/v solution of amine in toluene. Separately, approximately 20 mg of methanol-solvated Mg_2(dobpdc) was filtered from the methanol mother liquor and washed with toluene (3 × 10 mL). After the toluene washes and subsequent drying on the filter for 2 min under vacuum, Mg_2(dobpdc) was added to the tetraamine solution and the vial was left at room temperature for 24 h (60 °C for 24 h in the case of 3-4-3). The 3-4-3 amine is solid at room temperature and was therefore melted using a heat gun prior to preparation of the amine solution. After soaking, the mixture was filtered and washed with toluene (3 × 10 mL). Tetraamine-appended Mg_2(dobpdc) was recovered as an off-white powder after 2 minutes of drying on the filter. To achieve desired 1:2 tetraamine:metal ratio, the as-synthesized material was then heated at activation temperatures given in Table S2 while under flowing N_2 for 1 h. In all cases, ^{1}H NMR digestion experiments were used to confirm tetraamine to Mg^{2+} site ratios. Tetraamine-appended M_2(dobpdc) was digested by suspending 2–5 mg of the powder in 0.7 mL of dimethyl sulfoxide-d_6 and adding 25 μL of deuterium chloride solution (35 wt % in D_2O) followed by sonication and heating by a heat gun. Tetraamine loadings were determined by comparing ^{1}H NMR peak integrations of framework aromatic resonances (7–8 ppm) to the methylene resonances of the tetraamine (1.6–3 ppm). For all of the tetraamine-appended metal–organic frameworks, powder X-ray diffraction patterns, infrared spectra, pure CO_2 adsorption isobars and isotherms, and thermogravimetric decomposition profiles under N_2 are given below.

Single-Crystal X-ray Diffraction Structures. Single crystals of Zn_2(dobpdc) were synthesized following two different literature procedures (*28*, *32*). Single crystals of 3-3-3-appended Zn_2(dobpdc) were synthesized and post-synthetically functionalized following a modified literature procedure in which tetraamines were used in place of diamines (*28*). Single crystals of Zn_2(dobpdc) for 3-4-3-appended Zn_2(dobpdc) were synthesized following a more recent literature procedure and then stored in a glovebox solvated in hexanes before use (*32*). A solution of 3-4-3 in toluene (25 μL of 3-4-3 in 4 mL toluene) was dried using CaH_2 and then cannula transferred onto molecular sieves (3Å) in a schlenk flask under an Ar atmosphere. The single crystals of Zn_2(dobpdc) were taken out of the glovebox and the dried 3-4-3 solution was cannula

transferred onto them to soak for at least 12 h at 60 °C. The crystals were washed with dry toluene (3 × 15 mL) for at least 1 h each at room temperature. Thermal activation was unnecessary for the single crystals of tetraamine-appended Zn_2(dobpdc) because the initial tetraamine loadings were not in excess of the desired 1:2 tetraamine:metal ratio. We note that single crystals of 3-4-3-appended Zn_2(dobpdc) were also prepared via a similar method to 3-3-3-appended Zn_2(dobpdc), resulting in a structure with a lower occupancy of 3-4-3 (58.6%, vs. 84.7%). The same binding mode of 3-4-3 was observed in both structures, suggesting that this specific multimetal coordination mode is thermodynamically favored across a range of tetraamine loadings. X-ray diffraction data were collected at the Advanced Light Source Station 11.3.1 or 12.2.1, Lawrence Berkeley National Laboratory, as specified in Table S14. The data were collected using synchrotron radiation (λ = 0.7293 or 0.7288 Å; see Table S14 for crystallographic data) and a Bruker AXS D8 diffractometer with a Bruker PHOTON II CMOS detector. The single-crystal structures of the tetraamine-appended Zn_2(dobpdc) frameworks were collected at 100 K using an Oxford Cryosystems Cryostream 700 Plus. The crystals were refined as inversion twins in either $P3_221$ or $P3_121$ space groups based on Flack parameter values of approximately 0.5. Bruker AXS Saint software (*39*) was used to correct for Lorentz and polarization effects. SADABS (*40*) was used for absorption corrections. The structures were solved with SHELXT (*41*) and refined with SHELXL (*42*) operated in the OLEX2 interface (*43*). All hydrogen atoms were placed geometrically and refined with a riding model. The thermal parameters for all non-hydrogen atoms were refined anisotropically. For each structure, the occupancy of the nitrogen atom bound to Zn (atom N1 in the .cif) was kept at full occupancy to account for solvent or water bound at sites where the amine is absent. The reported formulas, however, reflect the nitrogen content for the tetraamines alone. In both cases, solvent molecules within the pore could not be modeled. Solvent masking was not used for either structure.

For the single-crystal structure of 3-3-3-appended Zn_2(dobpdc), the chemical occupancy of the tetraamine freely refined to an occupancy of 0.423(9), which was fixed in the final refinement. Several reflections for which $F_o << F_c$ were omitted from the final refinement: (0 2 0), (2 3 0), (0 3 1), (−2 5 0), (−1 6 0), (1 5 0), (0 1 1), (−3 6 0), (−6 6 1), (0 7 0), (3 3 0), and (0 1 0). A subset of these reflections was suspected to be affected by the beamstop. The remaining disagreeable reflections may have resulted from an additional complication with the model, such as residual solvent within the pores that may have interfered with data quality. (We note that complications arising from solvent in the pores of metal–organic framework single crystals have been demonstrated previously (*44*), particularly for structures collected at cryogenic temperatures (*45*).) Nonetheless, we believe the structure as modeled to be representative of the dominant conformation of the framework and appended tetraamine.

For the single-crystal structure of 3-4-3-appended Zn_2(dobpdc), the chemical occupancy of the tetraamine freely refined to an occupancy of 0.85(4), which was fixed in the final refinement. The middle alkyl linker (C11, C12, C13, and C14) of the tetraamine was found to be disordered over two positions, requiring distance (DFIX) and displacement parameter restraints (DELU and SIMU). Two reflections were suspected to be affected by the beamstop and were omitted from the final refinement: (−1 2 0), (1 1 0).

Thermogravimetric Analysis and Cycling Measurements. All dry thermogravimetric analysis (TGA) studies were completed on either a TA Instruments TGA Q5000 or a TA Instruments

Discovery TGA. All humid TGA studies were completed on a TA Instruments TGA Q50 modified with two air-free water bubblers at room temperature to pre-humidify gas streams prior to the furnace inlet. The water content resulting using this method was previously estimated to be 2.6% at 25 °C (*32*). Decomposition experiments were collected under dry N_2 (flow rate = 25 mL/min) at a ramp rate of 2 °C/min. Dry isobars were collected under the relevant gas (flow rate = 25 mL/min) at a ramp rate of 1 °C/min unless noted otherwise. All gases used for isobars, including pre-mixed cylinders of CO_2 in N_2, were purchased from Praxair. Samples were activated to achieve appropriate tetraamine to M^{2+} ratios under flowing N_2 for 60 min at various temperatures outlined in Table S2 that were determined from decomposition analyses found in Figures S3 and S4.

Solid-State Magic Angle Spinning (MAS) NMR Experiments. Activation of Mg_2(dobpdc)(3-4-3) with appropriate tetraamine loading (1 tetraamine for every 2 Mg^{2+} sites) was carried out under flowing N_2 at 180 °C for 15 min. Activated Mg_2(dobpdc)(3-4-3) was packed into a 3.2 mm rotor inside a N_2-filled glove bag and evacuated inside a home-built gas manifold for 10 min at room temperature. This manifold enables gas dosing of rotors at controlled pressures, as well as the subsequent sealing of dosed rotors inside the manifold (*38*). The Mg_2(dobpdc)(3-4-3) sample was dosed with $^{13}CO_2$ gas (Sigma-Aldrich, 99 atom % ^{13}C, <3 atom % ^{18}O) at 22 °C and allowed to equilibrate for 19 h prior to NMR measurements, with a final gas pressure of 1038 mbar immediately before the rotor was sealed. All solid-state NMR experiments were carried out at 16.4 T using a Bruker 3.2 mm probe, and MAS rates were 15 kHz in all cases. All solid-state ^{13}C and ^{15}N NMR spectra were acquired by cross-polarization from ^{1}H, and with continuous wave ^{1}H decoupling during acquisition, and with the contact times stated in the figure captions. The ^{1}H, ^{13}C, and ^{15}N chemical shifts were referenced to 1.8 ppm (adamantane), 38.5 ppm (adamantane tertiary carbon, left-hand resonance), and 33.4 ppm (glycine), respectively.

***In situ* Diffuse Reflectance Infrared Spectroscopy**. *In situ* Diffuse Reflectance Infrared Fourier Transform Spectroscopy (DRIFTS) data were collected using a Bruker Vertex 70 spectrometer equipped with a glowbar source, KBr beamsplitter, and a liquid nitrogen cooled mercury-cadmium-telluride detector. A custom-built diffuse reflectance system with an IR-accessible gas dosing cell was used for all measurements. The gas cell can be operated under flow or static modes and is equipped with a thermocouple in the sample space and a button heater for temperature control. In a typical static experiment, activated framework was dispersed in dry KBr (10 wt %) in an argon-filled glovebox and evacuated at 120 °C overnight. Spectra were collected *in situ* under $^{12}CO_2$ gas (99.998%) and $^{13}CO_2$ gas (Sigma-Aldrich, 99 atom % ^{13}C, <3 atom % ^{18}O) at 4 cm^{-1} resolution continually until equilibrium was reached.

***In situ* Powder X-ray Diffraction Studies**. High-resolution powder X-ray diffraction patterns were collected at Beamline 17-BM-B at the Advanced Photon Source of Argonne National Laboratory, with an average wavelength of 0.45415 Å. Scattered intensity was recorded by a Varex 4343CT a-Si Flat Panel detector. Diffraction patterns were analyzed using TOPAS-Academic v4.1 (*46*). Prior to measurement, samples were packed in borosilicate glass capillaries of 1.0 mm diameter under a N_2 atmosphere. Each capillary was attached to a custom-designed gas-dosing cell equipped with a gas valve, which was then mounted onto the goniometer head and connected to a gas-dosing manifold for *in situ* diffraction measurements. Sample temperature was controlled by an Oxford CryoSystems Cryostream. The sample was activated

under vacuum at 180 °C for 15 min and then cooled to 25 °C. The sample was then heated to 180 °C and the gas-dosing manifold was used to dose the frameworks with CO_2 (1 bar). After reaching equilibrium (typically less than five min as confirmed by diffraction patterns), the samples were cooled at 1 °C per min until 100 °C, then rapidly cooled to 25 °C. Diffraction patterns at select temperatures were indexed and Pawley refinements performed to extract unit cell parameters.

Rietveld refinement details. DFT structures of activated and CO_2-inserted Mg_2(dobpdc)(3-4-3) were compared against synchrotron *in situ* powder diffraction patterns in order to determine the structural validity of the calculated models. Rietveld refinements were performed in TOPAS Academic 4.1 (*46*) using X-ray powder diffraction patterns of activated Mg_2(dobpdc)(3-4-3) collected under vacuum at 30°C and under 1 bar of CO_2 at 30°C. DFT calculated structures of Mg_2(dobpdc)(3-4-3) and Mg_2(dobpdc)(3-4-3)$(CO_2)_2$ were used as starting points for each refinement respectively. As a comparison, an alternative DFT-calculated structure of Mg_2(dobpdc)(3-4-3) (Figure S34) with the tetraamine in a different bridging conformation was also used to probe the effects of differing tetraamine conformations on the PXRD patterns (Figure S35). Preferred orientation in the [001] direction was treated by a single March-Dollase parameter (*47, 48*). In the final stages of each refinement, the occupancies of the appended tetraamine or carbamate chains, all non-hydrogen atomic displacement parameters, and the unit cell parameters were fully refined with no constraints and convoluted with the sample and instrument parameters and Chebyshev background polynomials.

Computational Details. First-principles density functional theory (DFT) calculations were carried out on Mg_2(dobodc)(3-4-3) using a plane-wave basis and projector augmented-wave (PAW) (*49*, *50*) pseudopotentials with the Vienna ab-initio Simulation Package (VASP) code (*50-53*). To include the effect of the van der Waals (vdW) dispersive interactions on binding energies, we performed structural relaxations with vdW dispersion-corrected functionals (vdW-DF2) (*54*) as implemented in VASP. For all calculations, we used (i) a Γ-point sampling of the Brillouin zone and (ii) a 600-eV plane-wave cutoff energy. We explicitly treated two valence electrons for Mg ($3s^2$), six for O ($2s^22p^4$), five for N ($2s^22p^3$), four for C ($2s^22p^2$), and one for H ($1s^1$). All structural relaxations were performed with a Gaussian smearing of 0.05 eV (*55*). The ions were relaxed until the Hellmann-Feynman forces were less than 0.02 eVÅ^{-1}.

To compute CO_2 binding energies, we optimized Mg_2(dobpdc)(3-4-3) prior to CO_2 adsorption ($E_{3\text{-}4\text{-}3\text{–}MOF}$), interacting with CO_2 in the gas phase (E_{CO2}) within a 15 Å × 15 Å × 15 Å cubic supercell, and Mg_2(dobpdc)(3-4-3) with an adsorbed CO_2 molecule ($E_{CO_2\text{–}3\text{-}4\text{-}3\text{–}MOF}$) using vdW-corrected DFT. The binding energies (E_B) were obtained via the difference (Eq. 1).

$$E_{\mathrm{B}} = E_{\mathrm{CO_2-3-4-3-MOF}} - \left(E_{\mathrm{3-4-3-MOF}} + E_{\mathrm{CO_2}}\right). \qquad (1)$$

For NMR simulations, we performed structural relaxations with (i) a 1000 eV plane-wave cutoff energy, (ii) a 0.01 eVÅ^{-1} force criterion, (iii) a 1 × 1 × 3 k-point, and (iv) a 10^{-7} eV self-consistency criterion. In these input criteria, the isotropic chemical shielding (σ_{iso}) is converged within 0.1 ppm. To compare our computed values to the experimental chemical shifts (δ_{iso}), we need the σ_{ref} values for ^{1}H, ^{13}C, and ^{15}N since the isotropic chemical shift (δ_{iso}) is obtained from

$\delta_{iso} = -(\sigma_{iso} - \sigma_{ref})$ where σ_{ref} is a reference value. To do this, we used previously-determined values of ($^{1}H(\sigma_{ref})$ = 31.4 ppm, $^{13}C(\sigma_{ref})$ = 160.1 ppm, $^{15}N(\sigma_{ref})$ = 21.9 ppm) (*38*).

Initial calculations of Mg_2(dobpdc)(3-4-3) resulted in structures featuring two different tetraamine coordination modes where the tetraamines bind metals that are ~16.7 Å apart (Fig. 3D, left) and ~13.1 Å apart (Figure S34). The structure with the longer tetraamine coordination mode was optimized further because it was found to be more consistent with experimental NMR, PXRD, single-crystal X-ray diffraction, and gas adsorption data. Moreover, the longer tetraamine coordination mode is more stable by 0.311 eV. Thus, the structure with the shorter tetraamine coordination mode was discarded.

Gas Adsorption Measurements. Adsorption isotherms for CO_2, N_2, O_2, CH_4, and H_2O were collected using a Micromeritics ASAP 3-Flex gas adsorption analyzer. The 77 K N_2 adsorption isotherms for activated Mg_2(dobpdc) was collected using a Micromeritics ASAP 2420 gas adsorption analyzer. All gases were purchased from Praxair with a purity of 99.998% or higher. For the H_2O isotherms, deionized water was degassed via three freeze–pump–thaw cycles prior to use. Isotherms collected at 40–120 °C were measured using a temperature-controlled hot plate and a well-stirred silicone oil bath. Isotherm temperatures were selected individually for each material using the CO_2 adsorption isobar data in order to ensure that the isotherm step position occurred within a well-resolved pressure range. Samples were activated prior to each isotherm by heating at 100 °C under dynamic vacuum (<10 μbar) for 1−3 h.

Calculation of Differential Enthalpies and Entropies of Adsorption and Desorption. Isotherms were fit by linear interpolation and specific CO_2 loadings (q) at exact pressures (p_q) were determined at various temperatures. The differential enthalpy of adsorption (Δh_{ads}) and differential entropy of adsorption (Δs_{ads}) were calculated using the Clausius–Clapeyron relationship (Eq. 2). Plotting $\ln(p_q)$ vs. $1/T$ at constant values of q yields a slope that can be used to calculate the differential enthalpy of adsorption. The y-intercept can then be used to calculate the corresponding differential entropy of adsorption (*56*).

$$\ln(p_q) = \left(\frac{\Delta h_{ads}}{R}\right)\left(\frac{1}{T}\right) + \left(\frac{-\Delta s_{ads}}{R}\right) \qquad (2)$$

Breakthrough Measurements. Mg_2(dobpdc)(3-4-3) was prepared on large-scale by soaking ~5 g of toluene-solvated Mg_2(dobpdc) in a toluene solution of 3-4-3 (5 g of amine in 20 mL of toluene). After soaking for 12 h in the amine solution, the resulting powder was soaked in 25 mL of fresh toluene at 60 °C for at least 1 h a total of three times. The powder was then heated to 240 °C under flowing Ar for 1 h to achieve the appropriate tetraamine loading, as verified by ^{1}H NMR. Semi-spherical pellets (350–700 μm diameter) of Mg_2(dobpdc)(3-4-3) were prepared for breakthrough by compression of ~1 g of the as-synthesized powder to form a tablet, which was then sieved between 25 and 45 mesh grids. A CO_2 isobar collected on the pellets (Figure S44) is essentially indistinguishable from the powder material (Figure S11), confirming pelletization does not alter the CO_2 adsorption properties.

Similar to previous procedures, a stainless steel column (6" length, 0.25" OD, and 0.035" wall thickness) was packed with ~0.67 g of activated material (desolvated and containing 1 tetraamine per 2 metal sites) (*29*, *32*). The column was modified to include an internal thermocouple that

extends 1.5" through the bottom of the column. The thermocouple was held in place through the use of a Swagelok 1/4" stainless steel union tee sealed with epoxy (JB Weld, work life: 1 min; rated to 175 °C). It should be noted that a high temperature epoxy was required to ensure the integrity of the seal at the high desorption temperatures of 100–120 °C. The reported experimental breakthrough temperatures correspond to the internal read temperature of the column equilibrated under He at the start of the experiment. The column temperature was controlled using external heat tape that was adjusted in temperature to achieve the desired internal read temperature. External heat tape temperatures of 42, 63, 106, and 130 °C were required to achieve internal column temperatures of 40, 60, 100, and 120 °C. Internal temperature excursions of <1 °C were measured upon exothermic adsorption during breakthrough experiments. Glass wool was added to both ends of the column to ensure the pellets were secured. The schematic of the breakthrough apparatus has been described in a previous report (*32*).

The breakthrough profile was monitored by an SRI Instruments 8610C GC equipped with a 6' Haysep-D column and a thermal conductivity detector (TCD), with 1 scan collected per min. The GC was calibrated using a series of pre-mixed CO_2 balanced by N_2 cylinders (5, 10, 15, 20, 30, and 50%) as well as pure CO_2 and N_2 cylinders from Praxair. Deadspace for the system was estimated using Ar after the system had been pre-equilibrated under He. A total inlet flow of 30 sccm was used for all gases and gas mixtures for both calibration and experiments. Flow rates were monitored every 0.5 s using an Agilent ADM2000 Universal Flow Meter at the GC outlet. The material was activated under 30 sccm of flowing He for 30 min at 140 °C prior to each breakthrough experiment to ensure that CO_2 was desorbed. All breakthrough experiments were conducted at atmospheric pressure, with a backpressure of ≤0.02 bar measured using an Ashcroft pressure gauge. Dry and humid breakthrough experiments and data processing were performed following previously reported procedures (*32*). Humid experiments were performed by flowing the inlet gas through a room-temperature dispersion tube that was assumed to produce a saturated stream of water at room temperature (~2.6% H_2O).

Breakthrough curves can be predicted from step-shaped adsorption isotherms. We have included a detailed explanation of this phenomenon in previous studies (*32*), building upon the analysis of several other groups who have developed general relationships between isotherm shapes and breakthrough profiles (*57-60*).

Steam Desorption Studies. The aforementioned DRIFTS setup was used for steam desorption studies in flow-through mode. An oven containing a bubbler was used as the boiler, which was connected to the sample cell by stainless steel tubing wrapped in heat tape and covered by aluminum foil and glass wool to ensure even heat distribution and to provide insulation. A bypass was constructed so dry gas could be used for sample activation. For all experiments, the oven and heat tape were kept at 110 °C while the sample was kept at 120 °C to prevent condensation. CO_2 (99.998%) and N_2 (UHP) were flowed through a Restek Alicat Flow Calibrator (0–50 sccm) into the bubbler through an Idex Fluidics Inline Solvent Filter (10 micron porosity) acting as a diffuser. Typically, carrier gas flow rates varied between 20 and 40 sccm. Samples (~10 wt % in diamond powder) were activated by heating under flowing dry N_2 at 140 °C. Following activation, samples were subjected to a 15 min adsorption period under steam/CO_2 (estimated 51–65% water content, balance CO_2) and 15 min desorption period under steam

(estimated 51–65% water content, balance N_2) over 15 total cycles. Concurrent IR spectra were collected at 1-min intervals with 4 cm^{-1} resolution. After the final cycle, the sample was re-activated under dry N_2 for ~15 minutes at 180 °C before TGA analysis. Steam content was estimated to be between 51% and 65% by measuring the amount of water consumed from the boiler (~1.2 mL per full cycle) during the course of the experiment and converting to the appropriate units.

Analysis of Samples Post-Steam Desorption Studies. Amounts of Mg_2(dobpdc)(3-4-3) in the Mg_2(dobpdc)(3-4-3) and diamond powder mixture were quantified using thermogravimetric decomposition with a TA Instruments TGA Q5000. Decompositions were performed under O_2 (flow rate = 25 mL/min). Initial sample weights for the diluted Mg_2(dobpdc)(3-4-3) mixtures were measured after heating to 180 °C (ramp rate = 10 °C/min) and holding for 1 h. Samples were then heated to 500 and 530 °C (ramp rate = 2 °C/min) and held at each temperature for 1 h. The weight of diamond and MgO was measured in the flat region between these two temperatures. The sample was then heated to 940 °C (ramp rate = 2 °C/min) and held for 30 min. to measure the weight of the MgO. The amount of diamond was determined by subtracting the weight of residual MgO from the diamond and MgO mixture to yield the amount of Mg_2(dobpdc)(3-4-3). These weights were used to correct the activated sample weights used in collecting the CO_2 isobars prior to thermogravimetric decomposition.

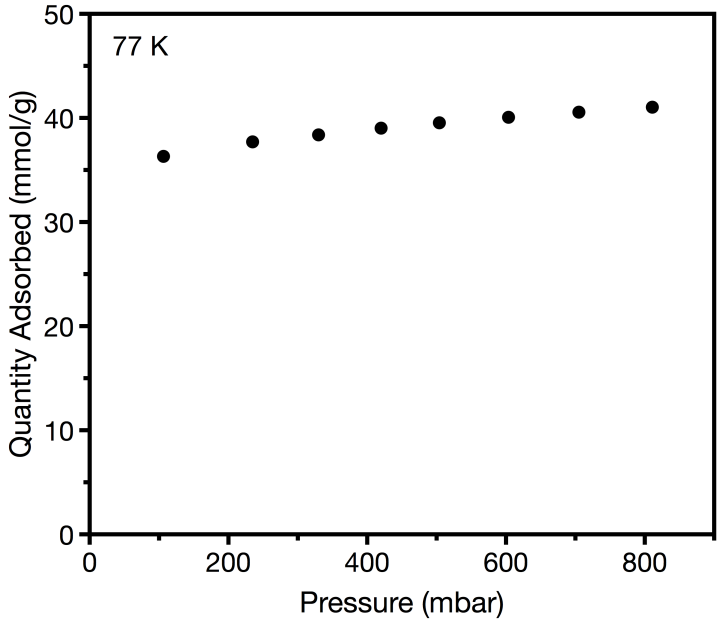

Figure S1. 77 K N_2 adsorption isotherm of activated Mg_2(dobpdc). The Langmuir surface area calculated from this isotherm is 3980 ± 40 m^2/g.

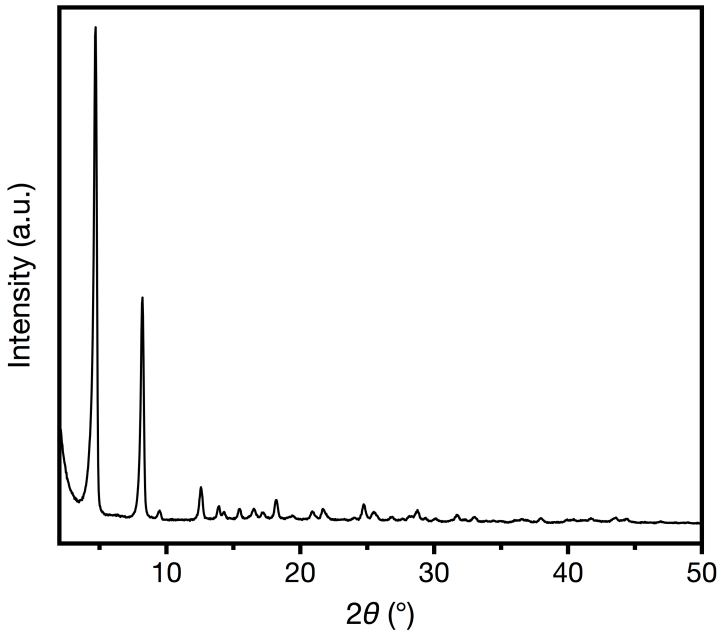

Figure S2. Powder X-ray diffraction pattern (CuKα radiation, λ = 1.5418 Å) for gram-scale synthesis of toluene-solvated Mg_2(dobpdc).

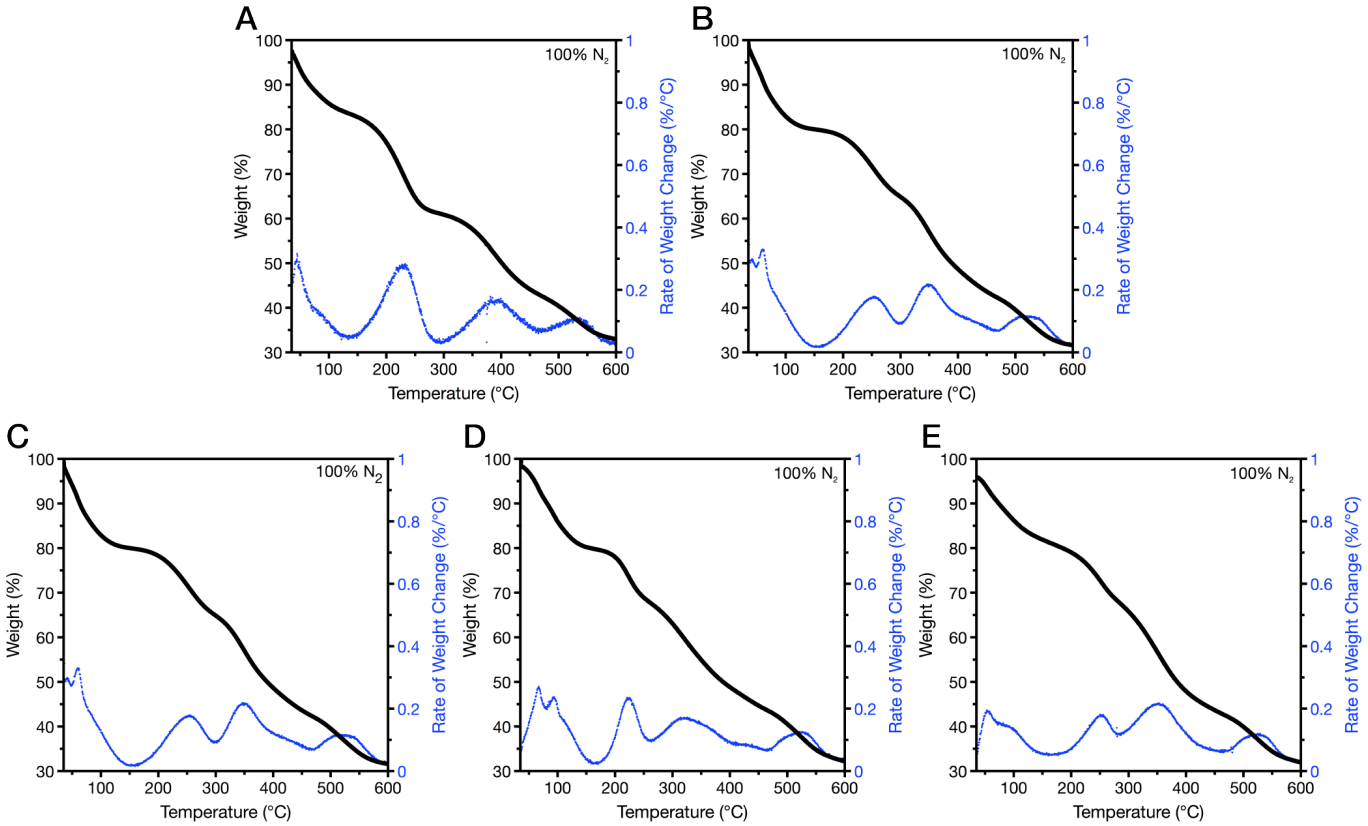

Figure S3. Decomposition profiles of Mg_2(dobpdc) functionalized with (**A**) 2-2-2, (**B**) 2-3-2, (**C**) 3-2-3, (**D**) 3-3-3, and (**E**) 3-4-3 obtained at a ramp rate of 2 °C/min.

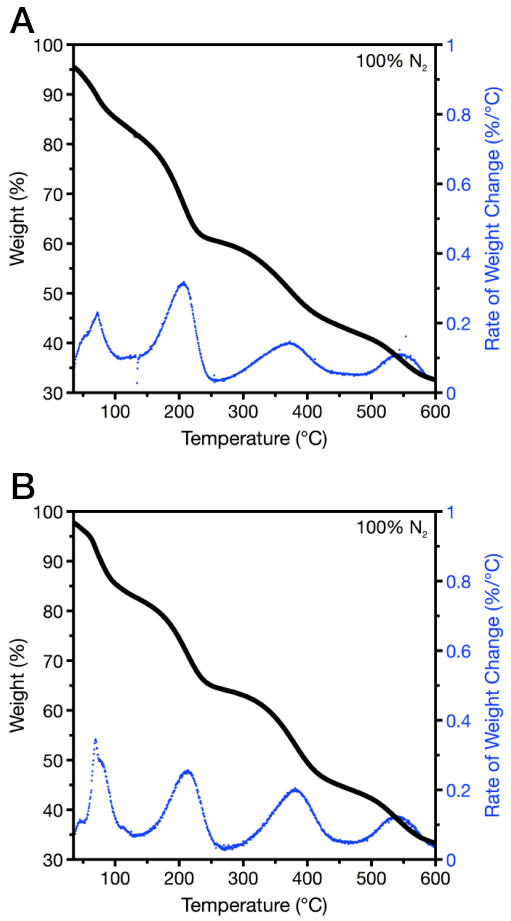

Figure S4. Decomposition profiles of Mg_2(dobpdc) functionalized with (**A**) 3-3 and (**B**) 3-4 obtained at a ramp rate of 2 °C/min.

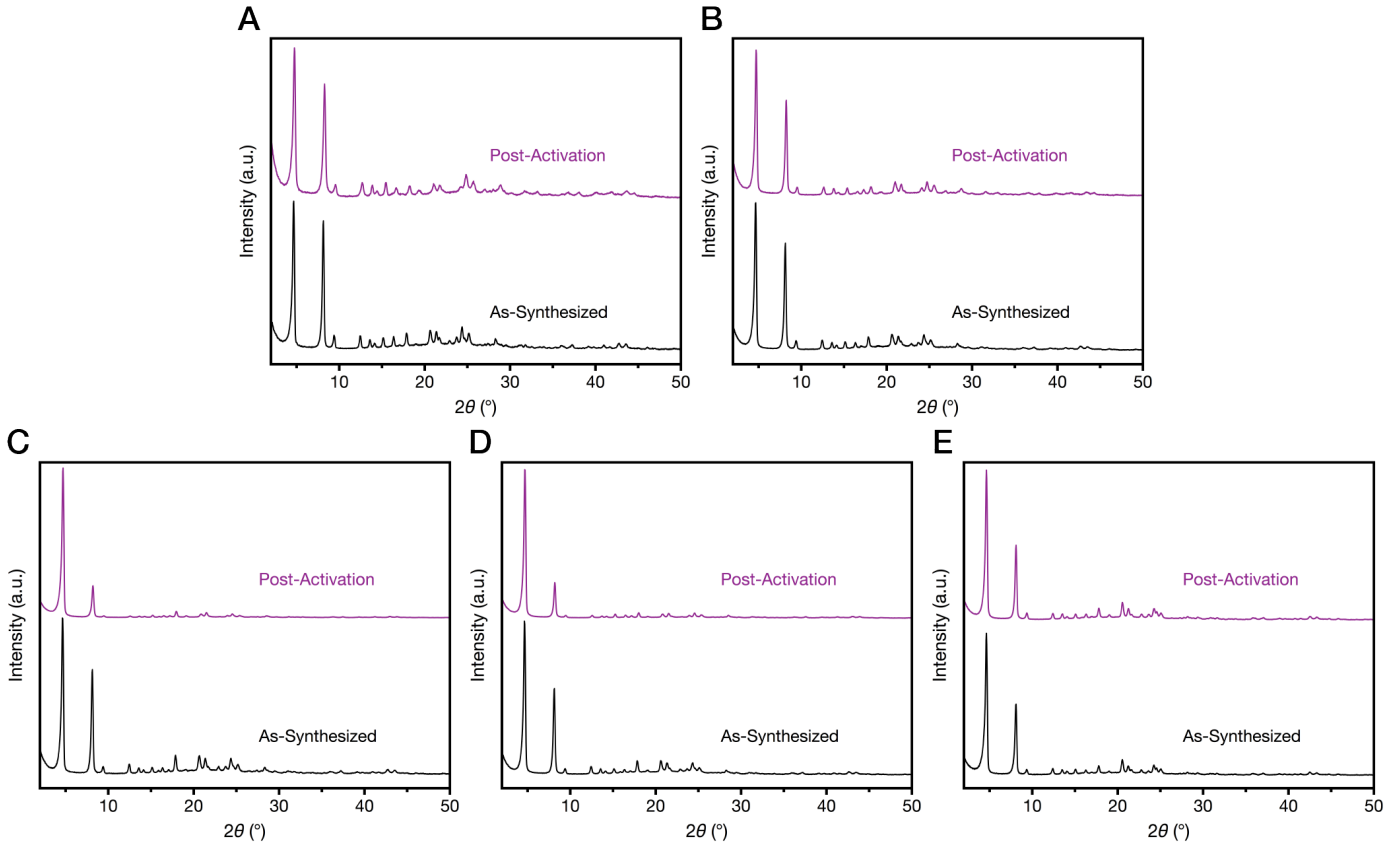

Figure S5. Powder X-ray diffraction patterns (CuKα radiation, λ = 1.5418 Å) of as-synthesized (black) and activated (purple, after obtaining the appropriate tetraamine loading of 1 tetraamine per 2 two metal sites) Mg_2(dobpdc)(tetraamine) for (**A**) 2-2-2, (**B**) 2-3-2, (**C**) 3-2-3, (**D**) 3-3-3, and (**E**) 3-4-3.

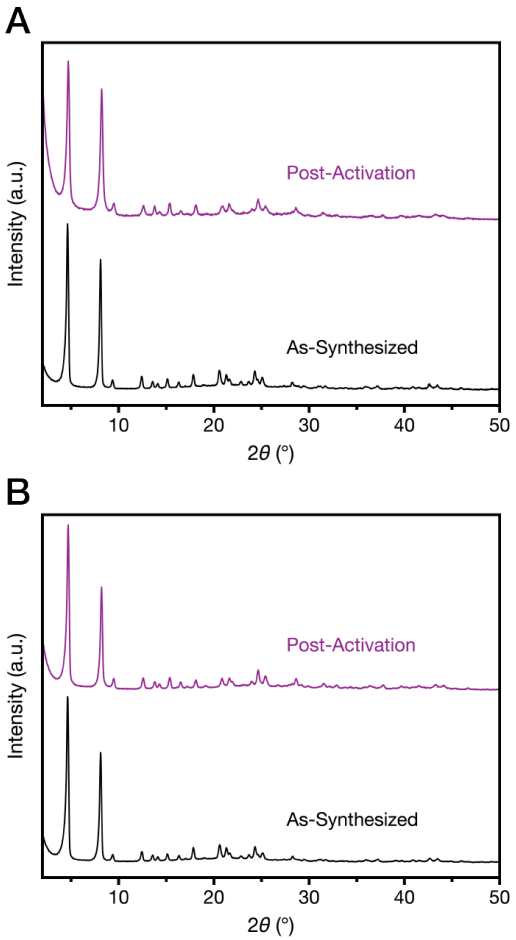

Figure S6. Powder X-ray diffraction patterns (CuKα radiation, λ = 1.5418 Å) as-synthesized (black) and activated Mg_2(dobpdc)(triamine) (purple, after obtaining the appropriate loading of 1 triamine per 2 two metal sites) for (**A**) 3-3 and (**B**) 3-4.

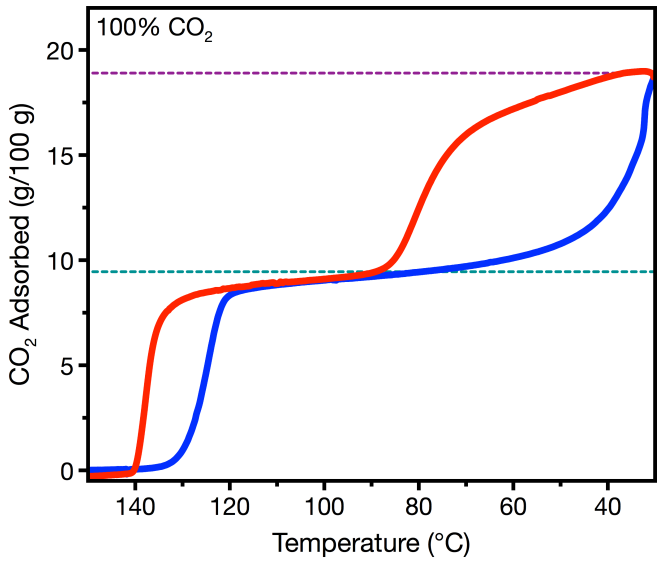

Figure S7. Pure CO_2 adsorption (cooling, blue) and desorption (heating, red) isobars for Mg_2(dobpdc)(2-2-2) at atmospheric pressure. A temperature ramp rate of 1 °C/min was used. Measurements were collected after activation at 225 °C under N_2 for 1 h. The dotted purple and teal lines represent the theoretical CO_2 uptake if each tetraamine could capture two CO_2 molecules and one CO_2 molecule, respectively.

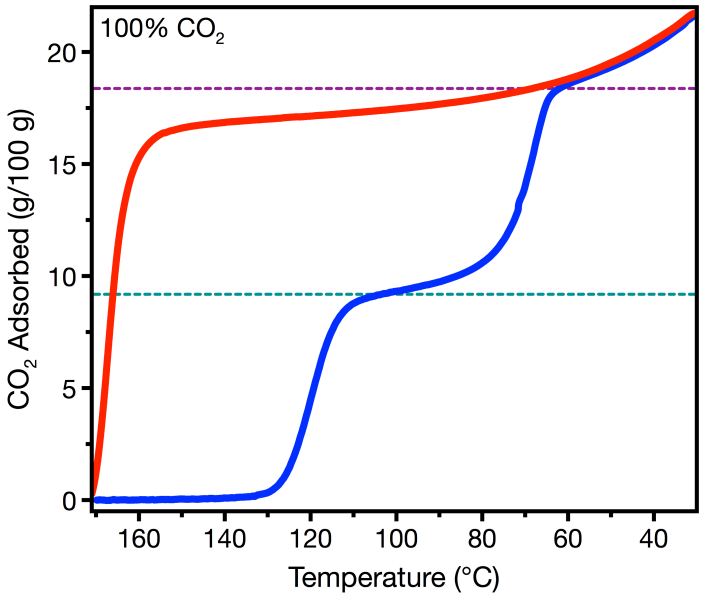

Figure S8. Pure CO_2 adsorption (cooling, blue) and desorption (heating, red) isobars for Mg_2(dobpdc)(2-3-2) at atmospheric pressure. A temperature ramp rate of 1 °C/min was used. Measurements were collected after activation at 225 °C under N_2 for 1 h. The dotted purple and teal lines represent the theoretical CO_2 uptake if each tetraamine could capture two CO_2 molecules and one CO_2 molecule, respectively.

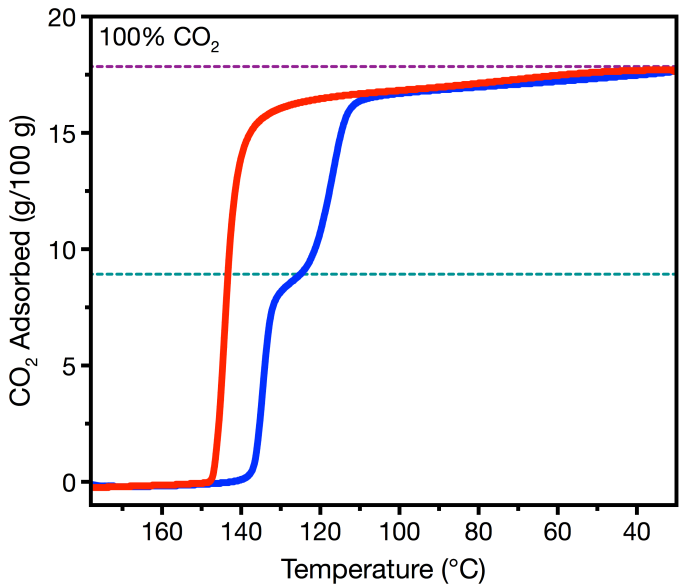

Figure S9. Pure CO_2 adsorption (cooling, blue) and desorption (heating, red) isobars for Mg_2(dobpdc)(3-2-3) at atmospheric pressure. A temperature ramp rate of 1 °C/min was used. Measurements were collected after activation at 225 °C under N_2 for 1 h. The dotted purple and teal lines represent the theoretical CO_2 uptake if each tetraamine could capture two CO_2 molecules and one CO_2 molecule, respectively.

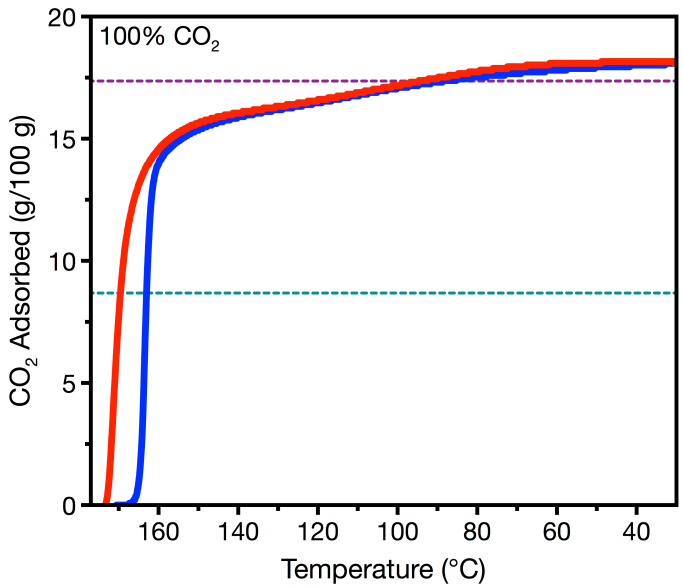

Figure S10. Pure CO_2 adsorption (cooling, blue) and desorption (heating, red) isobars for Mg_2(dobpdc)(3-3-3) at atmospheric pressure. A temperature ramp rate of 1 °C/min was used. Measurements were collected after activation at 225 °C under N_2 for 1 h. It should be noted that, while the other tetraamine-appended materials exhibit stable capacities over the course of multiple runs, the CO_2 adsorption capacity of Mg_2(dobpdc)(3-3-3) decreases. Further studies are underway to understand this behavior. The dotted purple and teal lines represent the theoretical CO_2 uptake if each tetraamine could capture two CO_2 molecules and one CO_2 molecule, respectively.

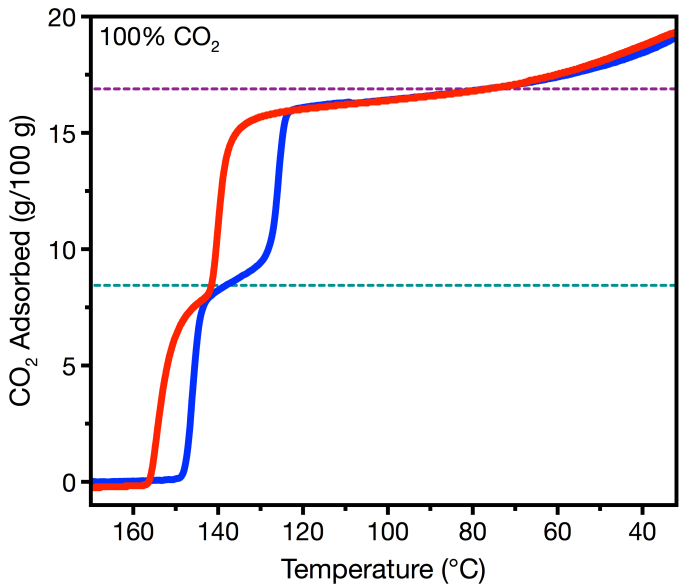

Figure S11. Pure CO_2 adsorption (cooling, blue) and desorption (heating, red) isobars for Mg_2(dobpdc)(3-4-3) at atmospheric pressure. A temperature ramp rate of 1 °C/min was used. Measurements were collected after activation at 240 °C under N_2 for 1 h. The dotted purple and teal lines represent the theoretical CO_2 uptake if each tetraamine could capture two CO_2 molecules and one CO_2 molecule, respectively.

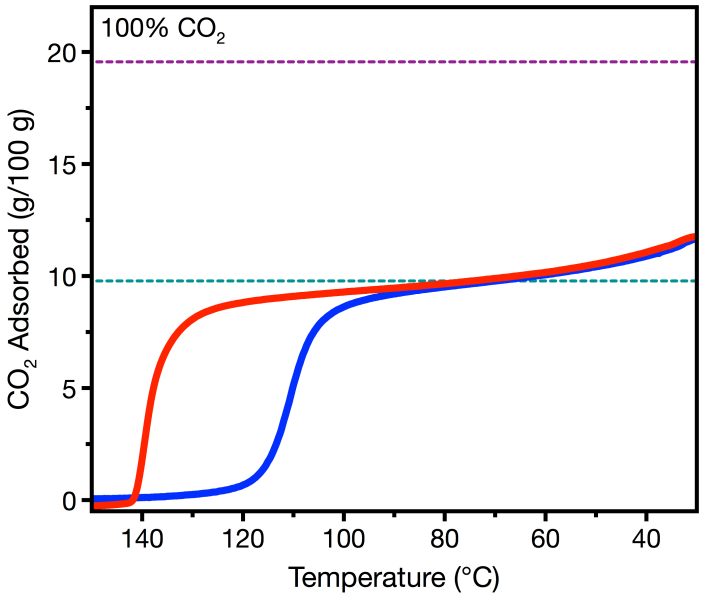

Figure S12. Pure CO_2 adsorption (cooling, blue) and desorption (heating, red) isobars collected at atmospheric pressure for Mg_2(dobpdc)(3-3) (bis(3-aminopropyl)amine). A temperature ramp rate of 1 °C/min was used. Measurements were collected after activation at 240 °C under N_2 for 1 h. The dotted purple and teal lines represent the theoretical CO_2 uptake if each triamine could capture two CO_2 molecules and one CO_2 molecule, respectively.

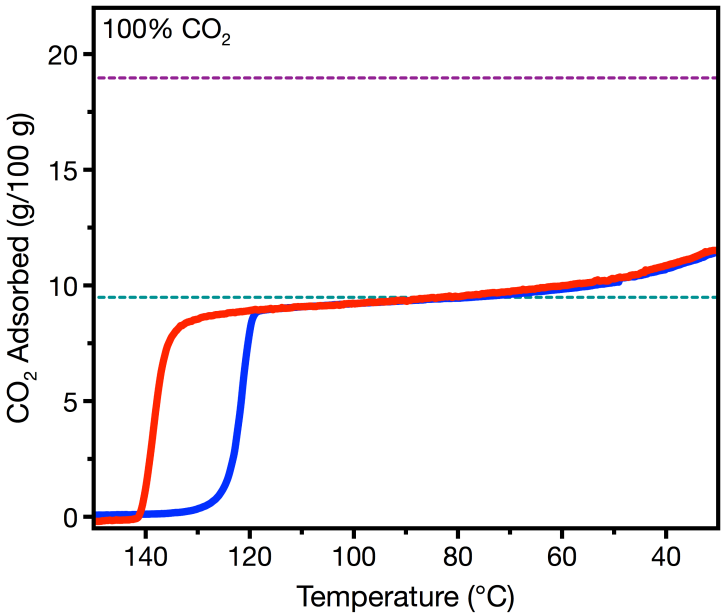

Figure S13. Pure CO_2 adsorption (cooling, blue) and desorption (heating, red) isobars collected at atmospheric pressure for the Mg_2(dobpdc)(3-4) (*N*-(3-aminopropyl)-1,4-diaminobutane). A temperature ramp rate of 1 °C/min was used. Measurements were collected after activation at 240 °C under N_2 for 1 h. The dotted purple and teal lines represent the theoretical CO_2 uptake if each triamine could capture two CO_2 molecules and one CO_2 molecule, respectively.

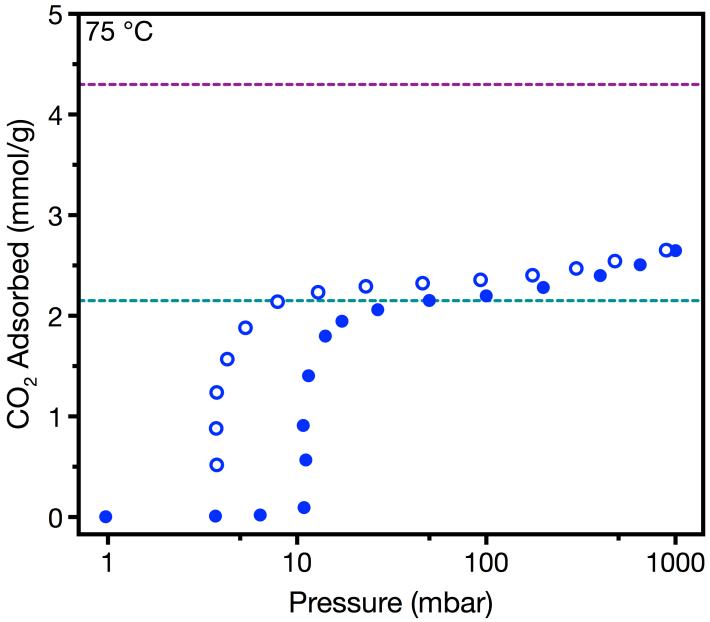

Figure S14. CO_2 adsorption (filled circles) and desorption (open circles) isotherms of Mg_2(dobpdc)(2-2-2) at 75 °C. Only the lower-pressure step is observed at this temperature as the higher-pressure step likely occurs at a pressure above 1000 mbar. The dotted purple and teal lines represent the theoretical CO_2 uptake if each tetraamine could capture two CO_2 molecules and one CO_2 molecule, respectively.

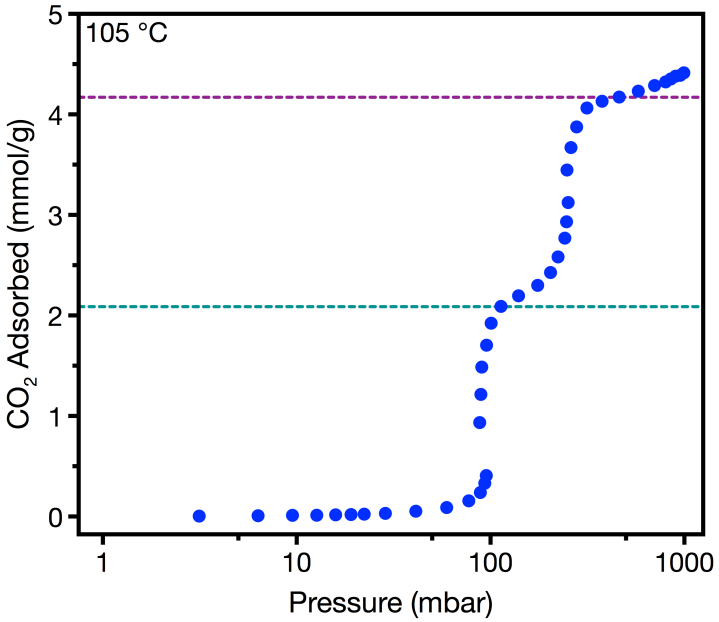

Figure S15. The CO_2 adsorption isotherm of Mg_2(dobpdc)(2-3-2) at 105 °C. The dotted purple and teal lines represent the theoretical CO_2 uptake if each tetraamine could capture two CO_2 molecules and one CO_2 molecule, respectively.

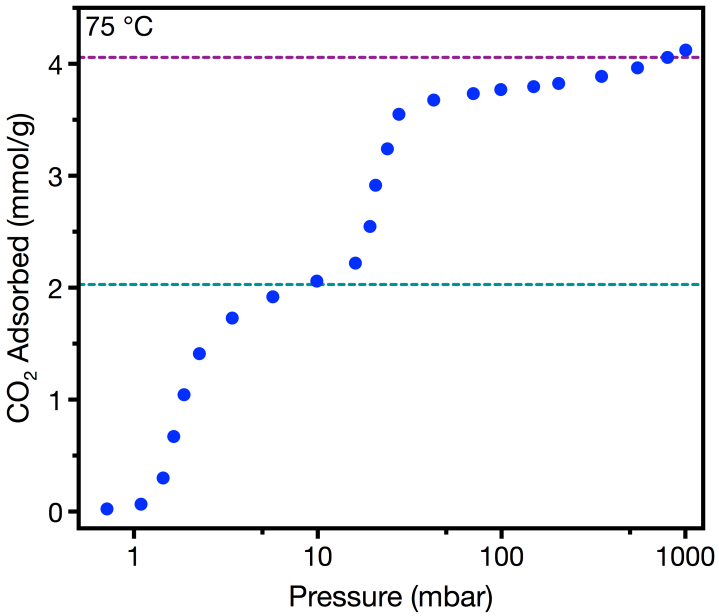

Figure S16. The CO_2 adsorption isotherm of Mg_2(dobpdc)(3-2-3) at 75 °C. The dotted purple and teal lines represent the theoretical CO_2 uptake if each tetraamine could capture two CO_2 molecules and one CO_2 molecule, respectively.

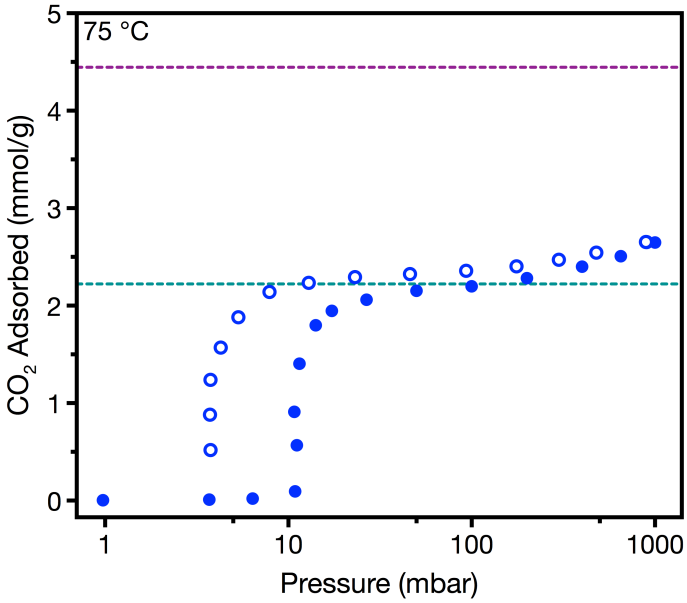

Figure S17. The CO_2 adsorption (filled circles) and desorption (open circles) isotherms of Mg_2(dobpdc)(3-3) at 75 °C. The dotted purple and teal lines represent the theoretical CO_2 uptake if each triamine could capture two CO_2 molecules and one CO_2 molecule, respectively.

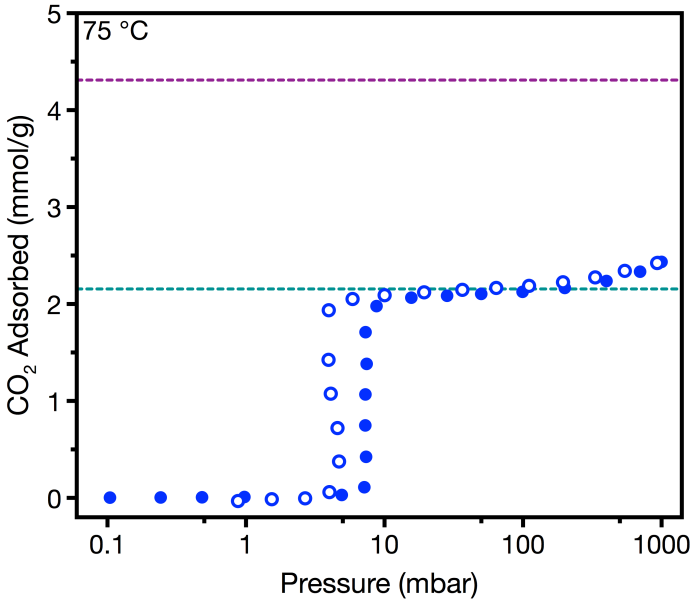

Figure S18. CO_2 adsorption (filled circles) and desorption (open circles) isotherms Mg_2(dobpdc)(3-4) at 75 °C. The dotted purple and teal lines represent the theoretical CO_2 uptake if each triamine could capture two CO_2 molecules and one CO_2 molecule, respectively.

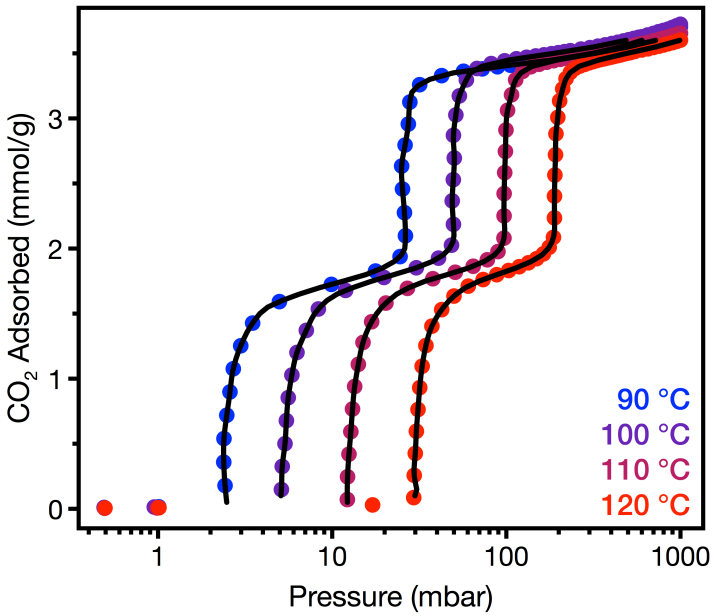

Figure S19. CO_2 adsorption isotherms at 90–120 °C for Mg_2(dobpdc)(3-4-3). Black lines depict the spline interpolation used to calculate the differential enthalpy and entropy of adsorption. The sample was activated under high vacuum (<10 μbar) at 135 °C for at least 1 h prior to each measurement.

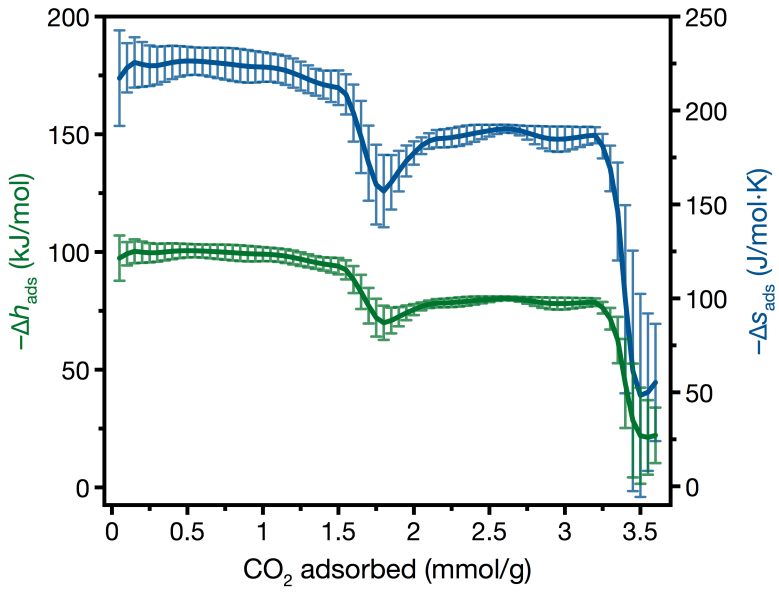

Figure S20. The $-\Delta h_{ads}$ (green) and $-\Delta s_{ads}$ (blue) for Mg_2(dobpdc)(3-4-3) determined using the Clausius–Clapeyron equation and the spline interpolation shown in Figure S19. One CO_2 per tetraamine and two CO_2 per tetraamine correspond to loadings of 1.92 and 3.84 mmol/g respectively.

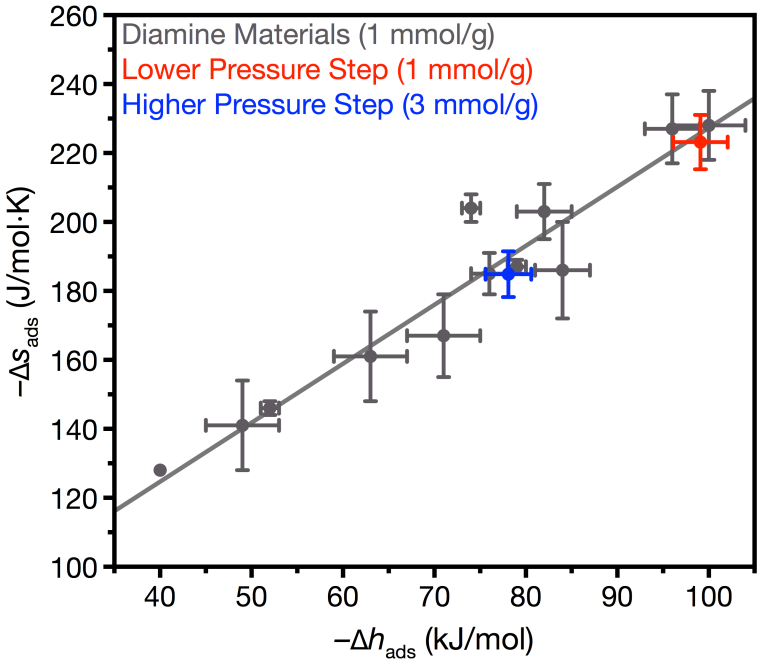

Figure S21. The differential enthalpy and differential entropy of adsorption for the lower pressure step, shown in red, and the higher pressure step, shown in blue, of Mg_2(dobpdc)(3-4-3), shown on a plot of the trend between the $-\Delta h_{ads}$ and $-\Delta s_{ads}$ for CO_2 adsorption in diamine-appended variants of Mg_2(dobpdc), as reported previously (*28*, *29*). The gray line is included to guide the eye, but the statistical significance of a linear correlation has not been definitively proven in this case (*61*).

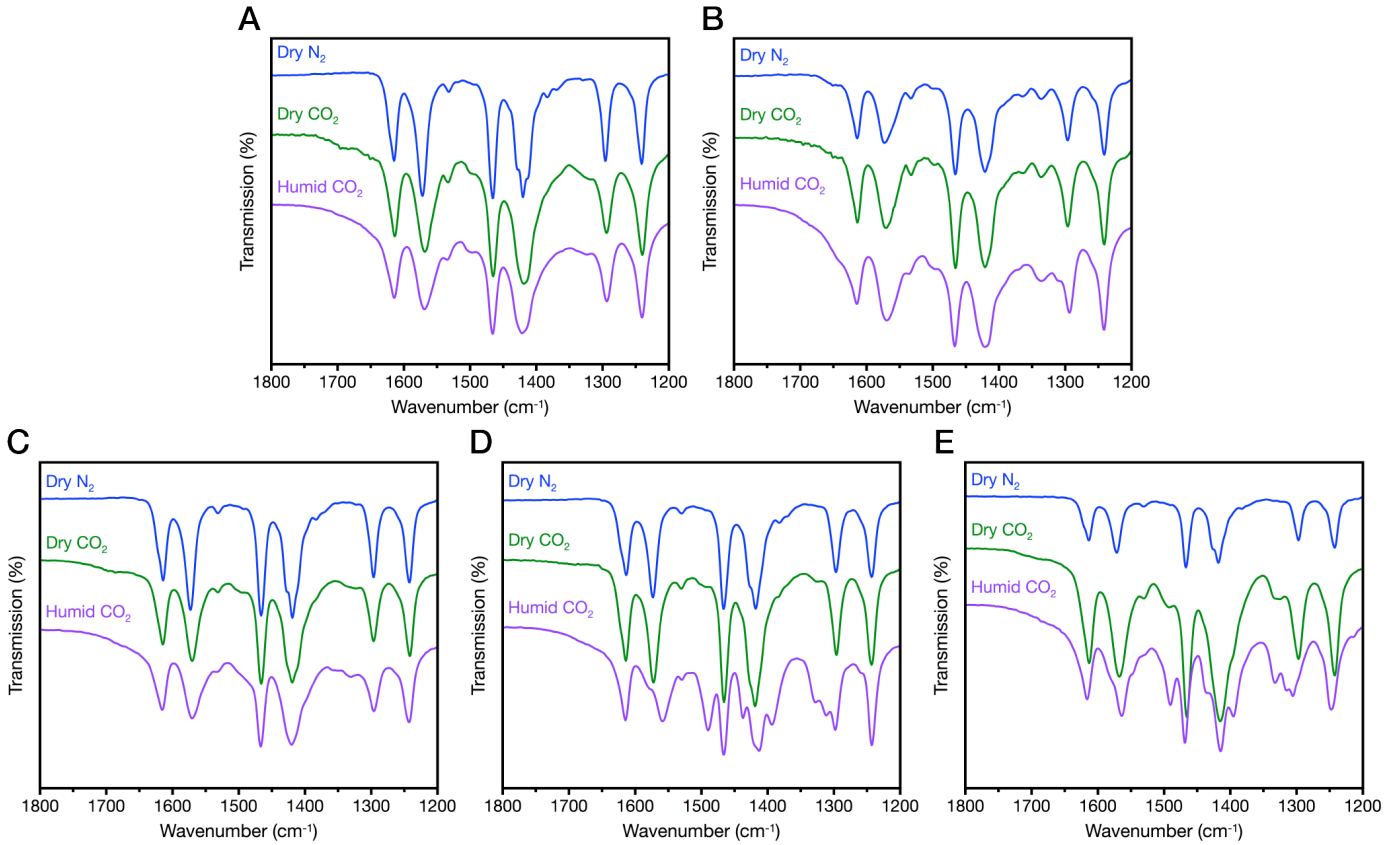

Figure S22. IR spectra of (**A**) 2-2-2, (**B**) 2-3-2, (**C**) 3-2-3, (**D**) 3-3-3, and (**E**) 3-4-3 functionalized Mg_2(dobpdc), under an atmosphere of dry N_2 (blue), dry CO_2 (green), and simulated humid CO_2 (purple). The simulated humid CO_2 spectra were collected by via a vapor dosing method where an open 4 mL scintillation vial containing the sample was placed in a closed 20 mL scintillation vial containing 3 mL water for at least 10 min prior to measurement. Previous work has revealed that diamine-functionalized variants of Mg_2(dobpdc) have characteristic C=O (1650–1700 cm^{-1}) and C–N (1320–1340 cm^{-1}) bands upon adsorption of CO_2 (*27*, *28*, *32*).

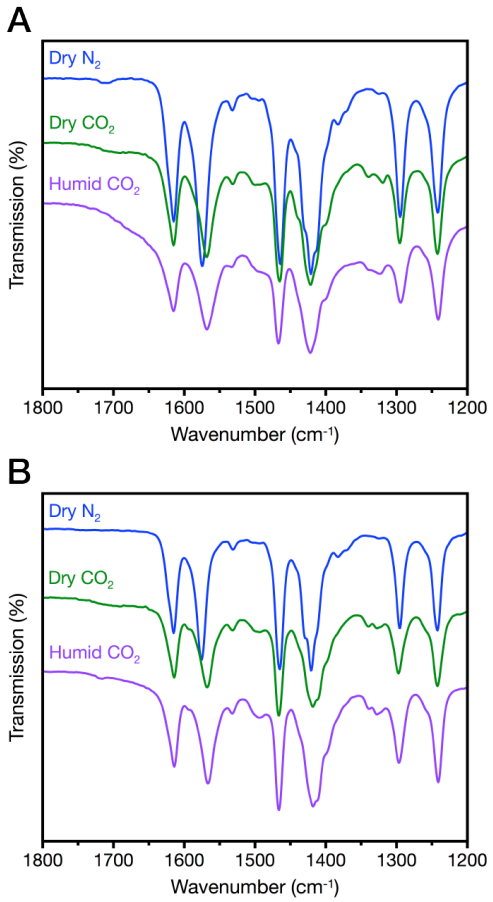

Figure S23. IR spectra of (**A**) 3-3 and (**B**) 3-4 functionalized Mg_2(dobpdc), under an atmosphere of dry N_2 (blue), dry CO_2 (green), and simulated humid CO_2 (purple). The simulated humid CO_2 spectra were collected by via a vapor dosing method where an open 4 mL scintillation vial containing the sample was placed in a closed 20 mL scintillation vial containing 3 mL water for at least 10 min prior to measurement. Previous work has revealed that diamine-functionalized variants of Mg_2(dobpdc) have characteristic C=O (1650–1700 cm^{-1}) and C–N (1320–1340 cm^{-1}) bands upon adsorption of CO_2 (*27*, *28*, *32*).

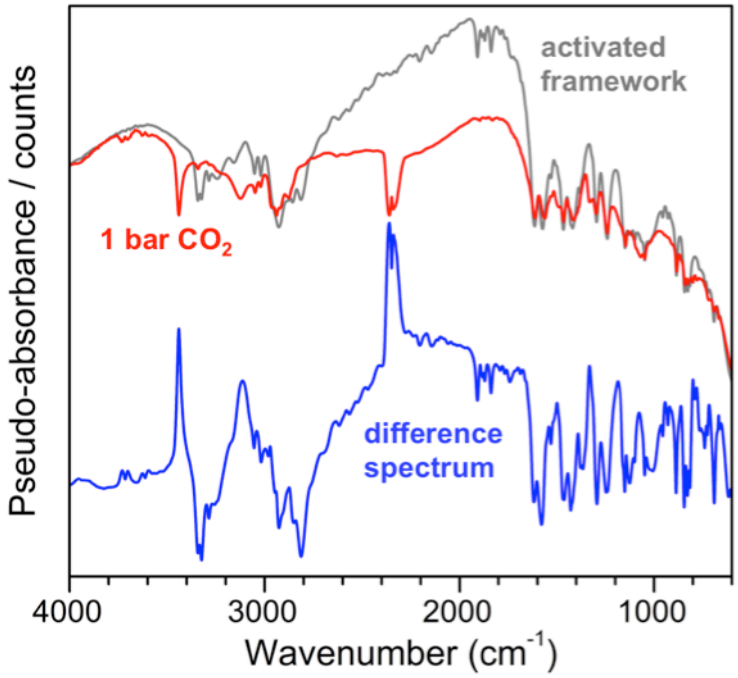

Figure S24. Infrared spectra for Mg_2(dobpdc)(3-4-3) collected using an IR spectrometer coupled to a gas sorption analyzer. The activated framework is shown in gray and the CO_2-dosed framework is shown in red. The difference spectrum is shown in blue.

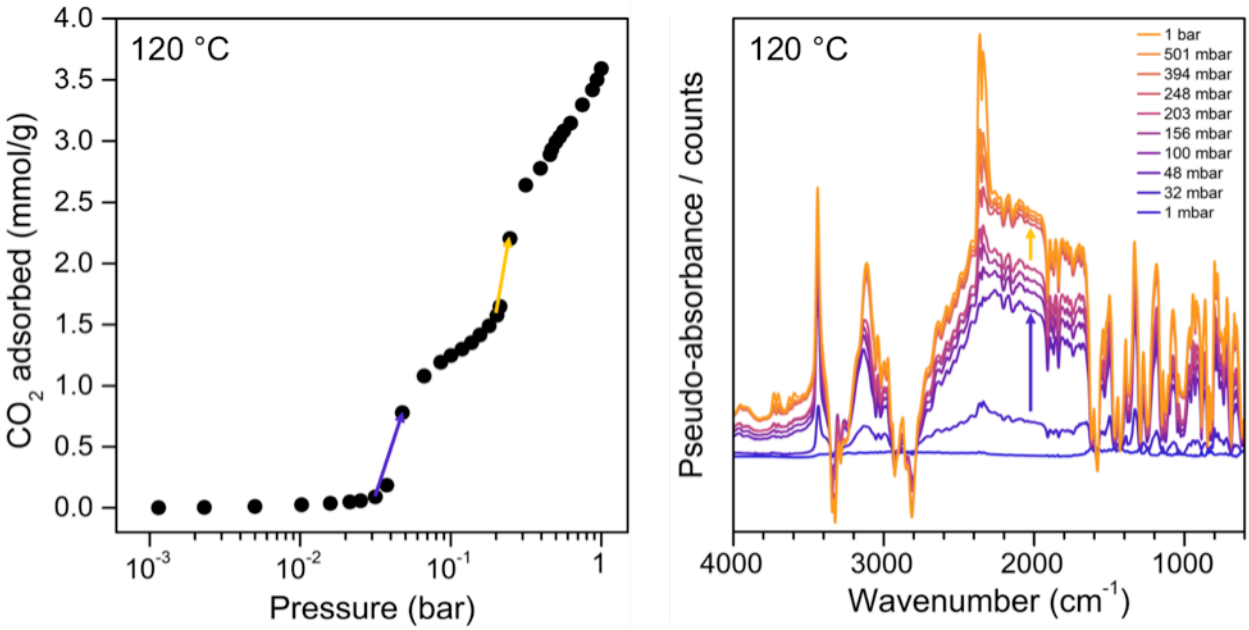

Figure S25. Infrared spectra for Mg_2(dobpdc)(3-4-3) (right) collected in tandem with the collection of a volumetric, equilibrium CO_2 isotherm (left).

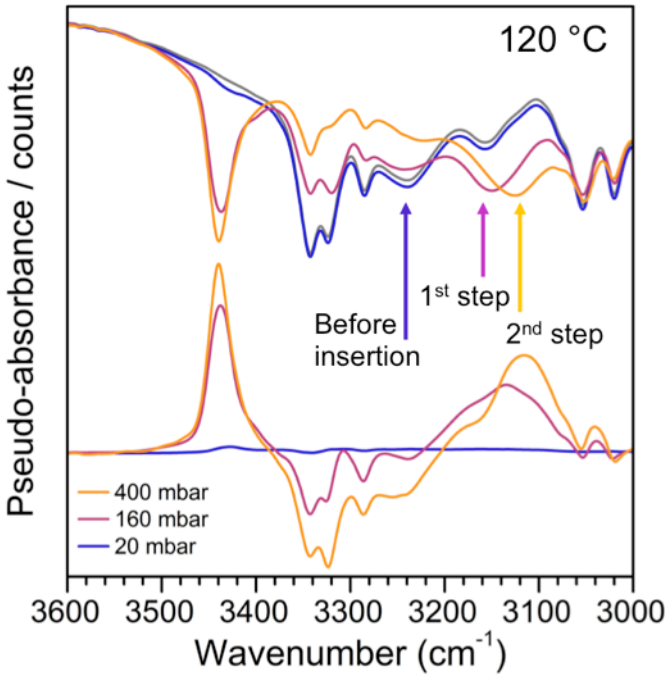

Figure S26. Infrared spectra showing the hydrogen bonding region of Mg_2(dobpdc)(3-4-3) collected at 120 °C under specific pressures of $^{12}CO_2$. Raw spectra (top) were collected at 20, 160, and 400 mbar (blue, purple, and orange respectively) corresponding to the pre-step, post 1st step and post 2nd step regions of the framework isotherm shown in Figure S25. Difference spectra at each pressure using the activated framework (gray) as background are shown (bottom). Broad peaks corresponding to distinct hydrogen bonding configurations can be clearly seen at each state of CO_2 adsorption in the framework (arrows).

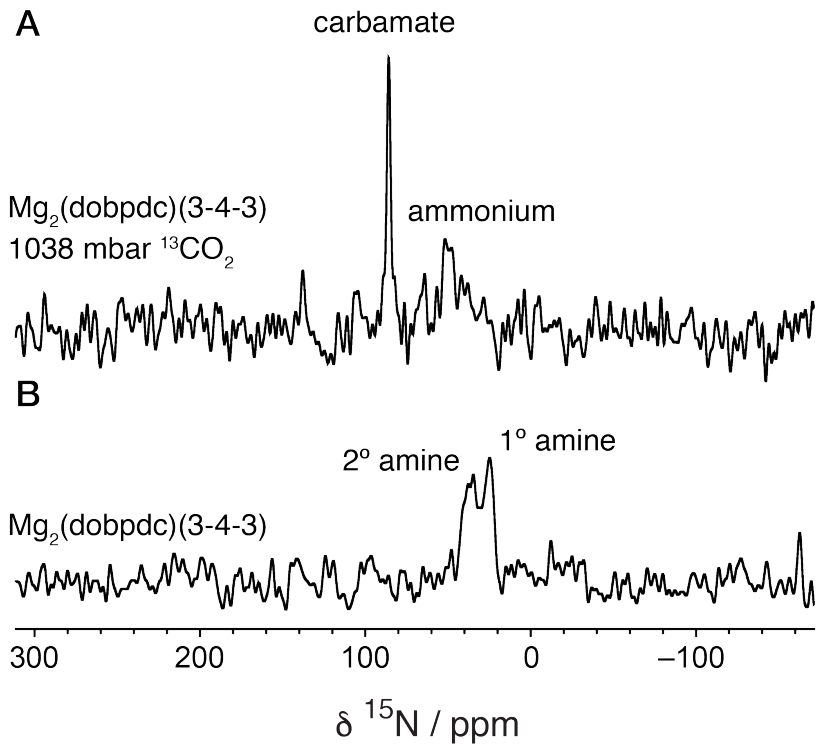

Figure S27. (**A**) Room-temperature ^{15}N NMR (16.4 T) spectrum (at natural isotopic abundance) of Mg_2(dobpdc)(3-4-3) after reaction with $^{13}CO_2$ (1 bar). (**B**) Reference spectrum collected before CO_2 dosing. The spectrum in A is consistent with insertion of CO_2 at a primary amine.

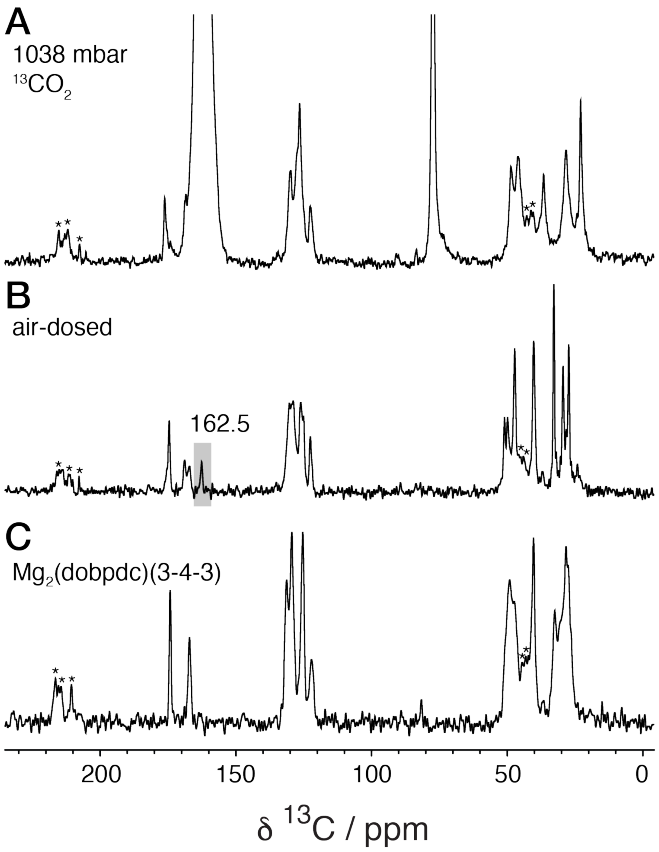

Figure S28. (**A**) Room-temperature ^{13}C MAS NMR spectrum (16.4 T) of (**A**) Mg_2(dobpdc)(3-4-3) dosed with 1038 mbar of $^{13}CO_2$, (**B**) Mg_2(dobpdc)(3-4-3) dosed with air, and (**C**) activated Mg_2(dobpdc)(3-4-3). The resonance at 162.6 ppm in the spectrum in **A** was assigned as a carbamate (note that this resonance is truncated here to allow the much weaker framework and amine resonances to be observed). The spectrum in **B** reveals formation of the same carbamate species as in **A**. For air-dosing, activated Mg_2(dobpdc)(3-4-3) was packed into a 3.2-mm rotor (with both caps removed), and compressed air was flowed over the uncapped rotor for at least 12 h, after which time the rotor was capped for NMR measurements. Asterisks mark spinning sidebands.

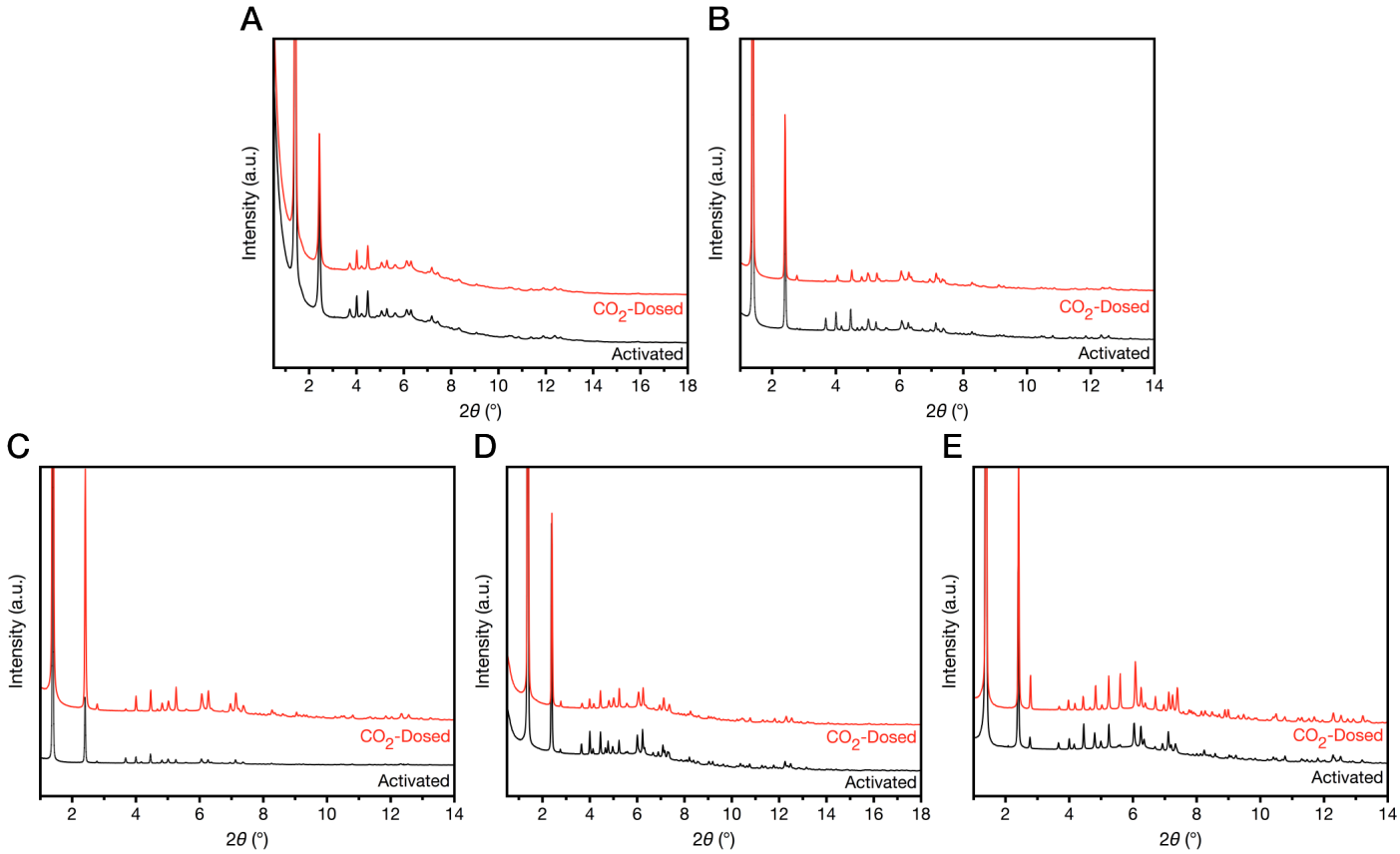

Figure S29. Powder X-ray diffraction patterns for evacuated Mg_2(dobpdc)(tetraamine) (black) and Mg_2(dobpdc)(tetraamine) dosed with 1 bar of CO_2 at 300 K (red) for (**A**) 2-2-2, (**B**) 2-3-2, (**C**) 3-2-3, (**D**) 3-3-3, and (**E**) 3-4-3. (λ = 0.45118 Å for **A** and **D**, 0.45399 Å for **B**, **C**, and **E**).

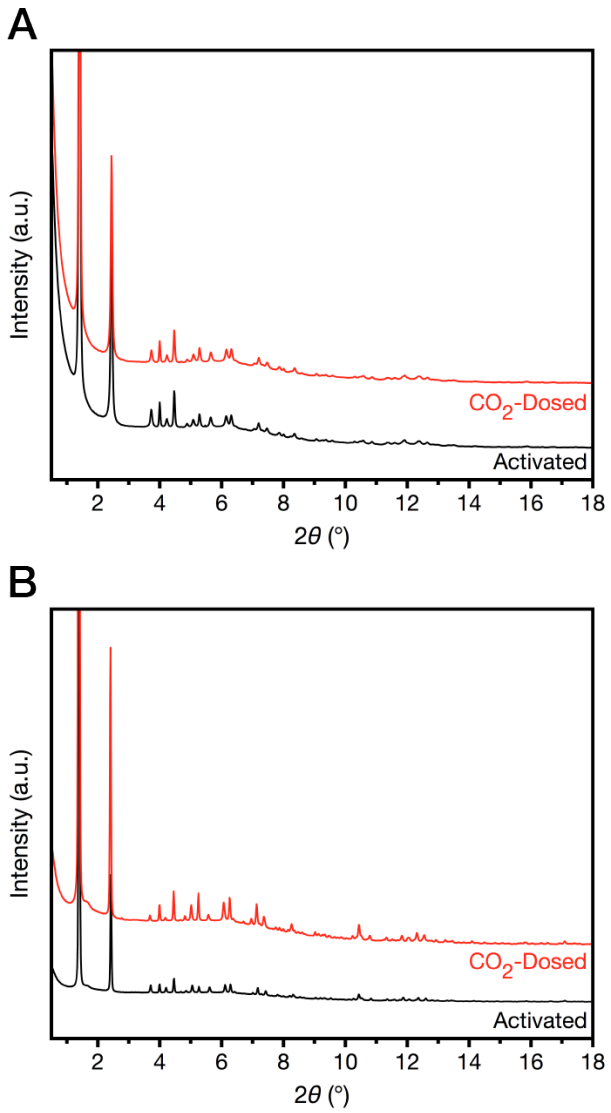

Figure S30. Powder X-ray diffraction patterns (λ = 0.45118 Å) for evacuated Mg_2(dobpdc)(triamine) (black) and Mg_2(dobpdc)(triamine) dosed with 1 bar of CO_2 at 300 K (red) for (**A**) triamine 3-3 and (**B**) triamine 3-4.

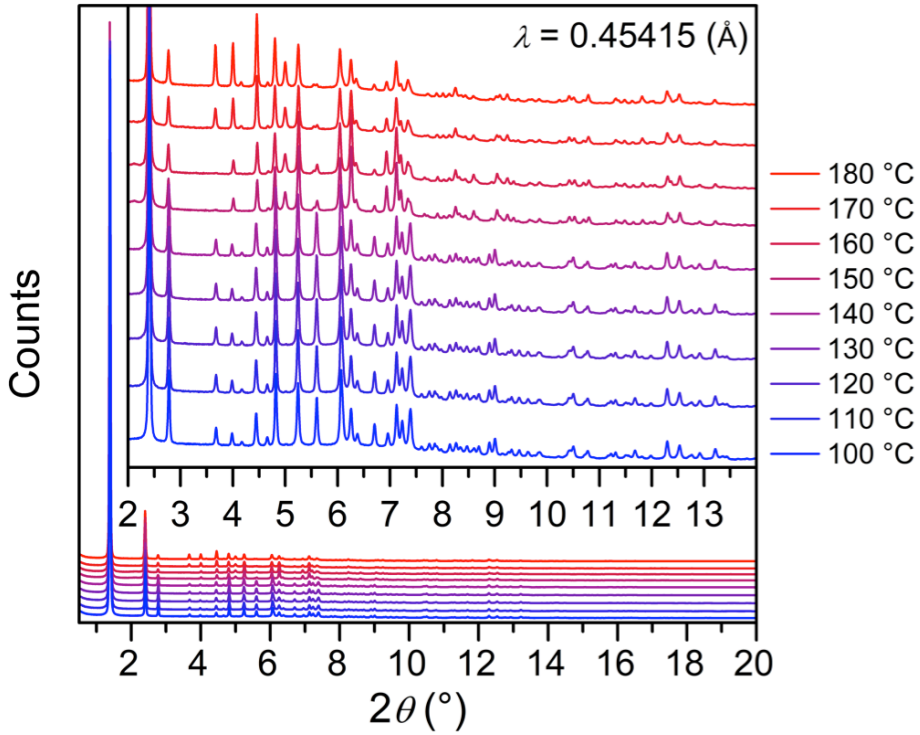

Figure S31. Variable-temperature powder X-ray diffraction data for Mg_2(dobpdc)(3-4-3) under 1 bar of CO_2. A sample of Mg_2(dobpdc)(3-4-3) was loaded into a capillary, activated at 180 °C, then dosed with 1 bar of CO_2. The temperature was ramped down to 100 °C (1 °C/min) and diffraction patterns were collected continuously. Two clear transitions corresponding to insertion of CO_2 at the 1st and 2nd steps can be seen from 160 to 150 °C and 140 to 130 °C, respectively. Discrepancies between the step temperature during the experiment and the TGA experiments are attributed to inaccuracies in the diffraction temperature sensor, which is located at the cryostream head instead of at the sample, resulting in sample temperatures around 10–15 °C lower than indicated.

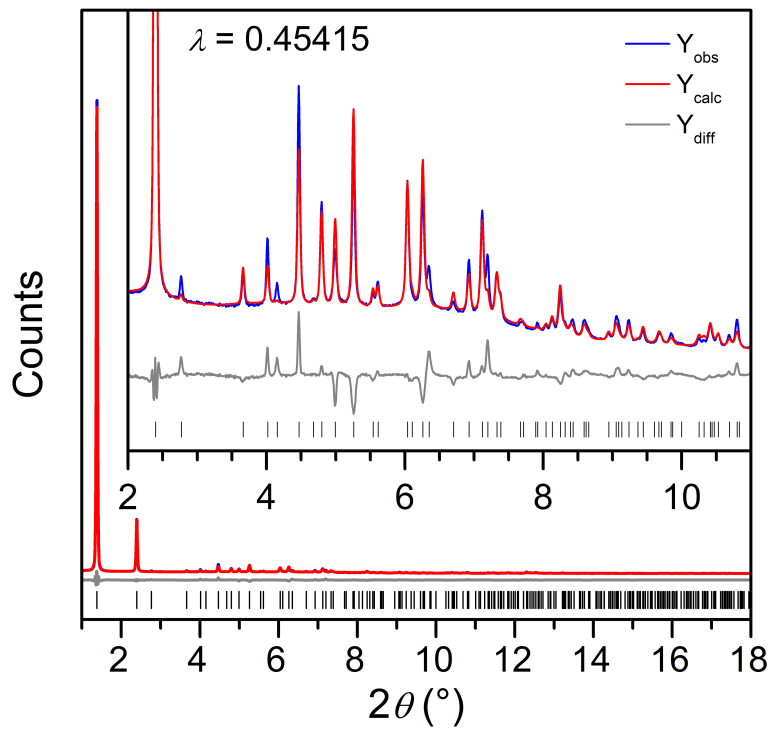

Figure S32. Rietveld refinement of activated Mg_2(dobpdc)(3-4-3) under vacuum, measured at 30°C from 0.5º to 18º. Blue and red lines represent the observed pattern and the pattern calculated using the optimized DFT structure as a starting point, respectively. The gray line represents the difference between observed and calculated patterns, and the black tick marks indicate calculated Bragg peak positions. The inset shows the high angle region at a magnified scale. While we were unable to freely refine atom positions of the appended tetraamines, and restraining the atom positions resulted in high thermal displacement parameters, a low R_{wp} value of 4.58% was still obtained. This indicates that overall the DFT structure is a reasonable approximation to the true structure, however it does not capture the disorder in the aliphatic portions of the tetraamines observed in SCXRD structures of the Zn congener. Figures-of-merit (as defined by TOPAS): R_{wp}= 4.58%, R_p= 3.08%, R_{exp}= 2.45%, R_{Bragg}= 0.96%, GoF = 1.87. The wavelength of measurement was 0.45415 Å.

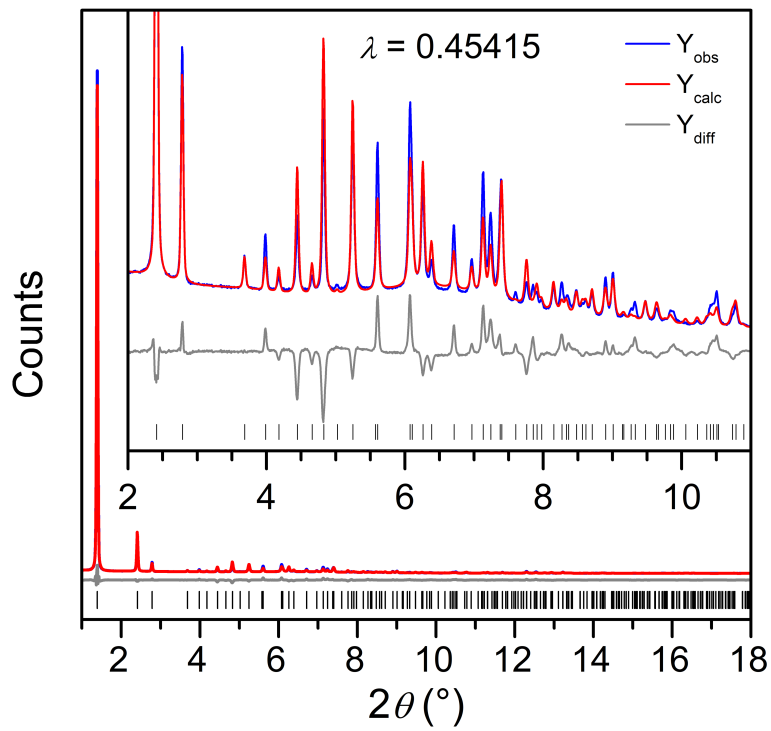

Figure S33. Rietveld refinement of activated $Mg_2(dobpdc)(3\text{-}4\text{-}3)(CO_2)_2$ under 1 bar CO_2, measured at 30°C from 0.5º to 18º. Blue and red lines represent the observed and calculated diffraction patterns, respectively. The gray line represents the difference between observed and calculated patterns, and the black tick marks indicate calculated Bragg peak positions. The inset shows the high angle region at a magnified scale. While allowing the atom positions of the appended tetraamine to freely refine resulted in unreasonable structures, a low R_{wp} value of 7.04% was still obtained. This indicates that overall the DFT structure is a reasonable approximation to the real structure, however the exact nature of any disorder found in the carbamate chains is not captured by this model. Figures-of-merit (as defined by TOPAS): Rwp= 7.04%, R_p= 4.54%, R_{exp}= 2.31%, R_{Bragg}= 3.36%, GoF = 3.05. The wavelength of measurement was 0.45415 Å.

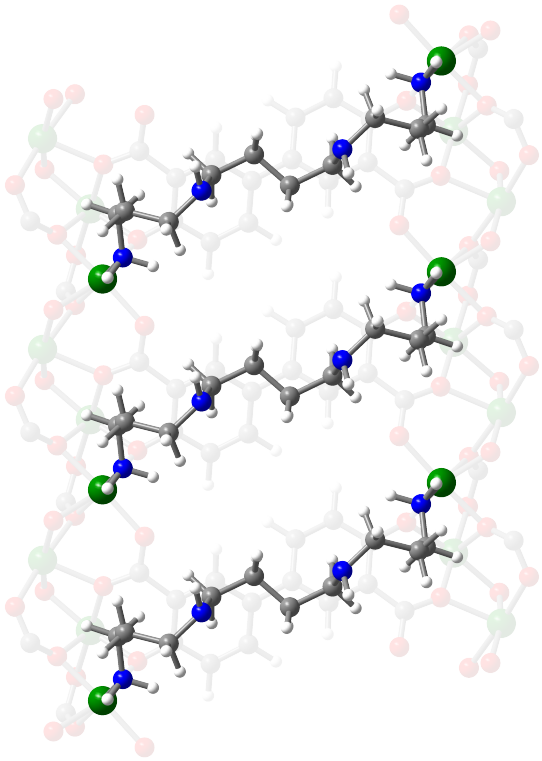

Figure S34. An alternative structural model of Mg_2(dobpdc)(3-4-3) where the tetraamines bind metals ~13.1 Å apart that was obtained from structural relaxations with vdW-corrected DFT. This structure was discarded due to inconsistencies with the experimental data (R_{wp} = 10.7% and GoF = 4.38, see below) and instability compared to the longer tetraamine coordination mode. Green, grey, red, blue, and white spheres represent Mg, C, O, N, and H atoms, respectively.

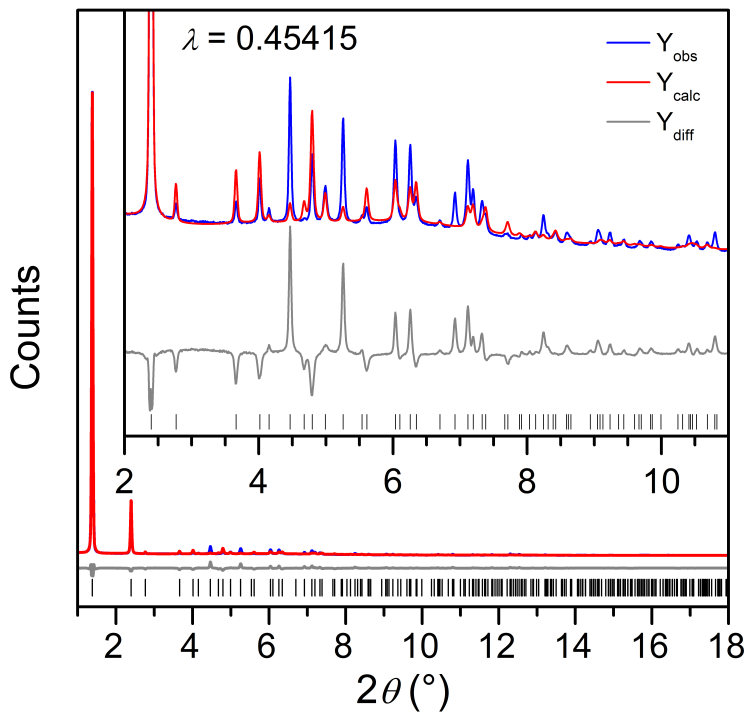

Figure S35. Rietveld refinement of activated Mg_2(dobpdc)(3-4-3) under vacuum, measured at 30°C from 0.5º to 18º. Blue and red lines represent the observed pattern and the pattern calculated using the discarded DFT structure (Figure S34) as a starting point, respectively. The gray line represents the difference between observed and calculated patterns, and the black tick marks indicate calculated Bragg peak positions. The inset shows the high angle region at a magnified scale. Despite performing the refinement using the same procedure as the previous refinement based on the optimized DFT structure, the occupancy of the appended tetraamine was unreasonably low (76%) and the R_{wp} remained high at 10.7%. Visual inspection also reveals many major discrepancies between the calculated and observed patterns. This suggests that the PXRD data does not support this tetraamine conformation. Figures-of-merit (as defined by TOPAS): R_{wp}= 10.7%, R_p= 6.00%, R_{exp}= 2.45%, R_{Bragg}= 2.51%, GoF = 4.38. The wavelength of measurement was 0.45415 Å.

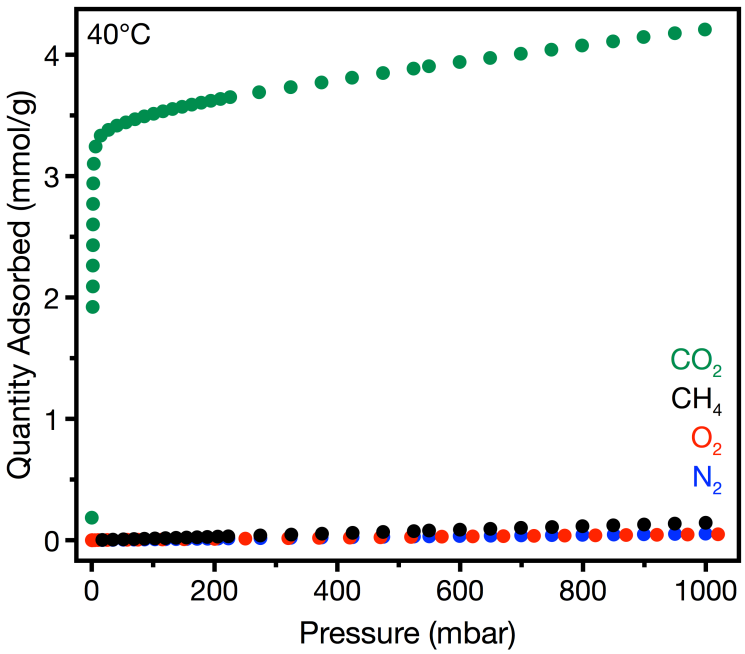

Figure S36. CO_2 (green), CH_4 (black), O_2 (red), and N_2 (blue) adsorption isotherms of Mg_2(dobpdc)(3-4-3) at 40 °C.

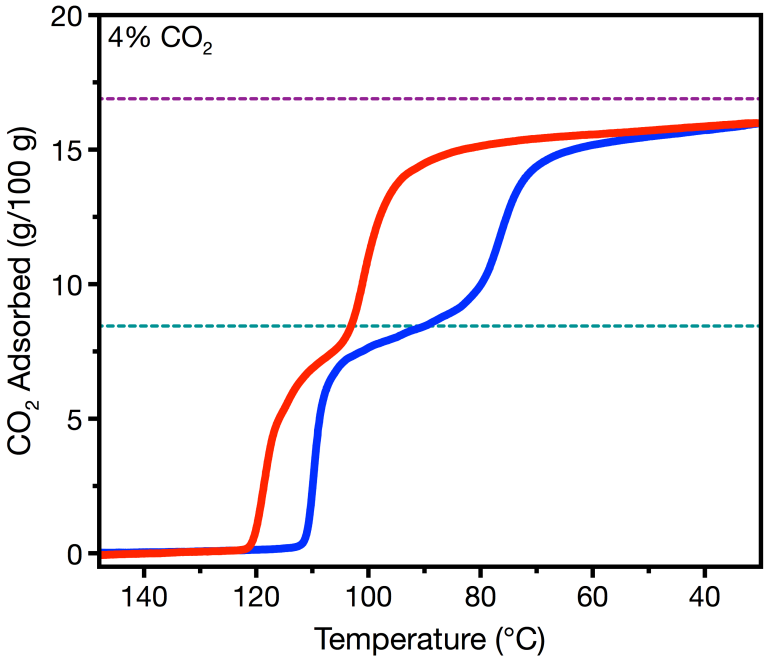

Figure S37. Thermogravimetric adsorption (cooling, blue) and desorption (heating, red) isobars at atmospheric pressure under 4% CO_2 for Mg_2(dobpdc)(3-4-3). A temperature ramp rate of 1 °C/min was used. The dotted purple and teal lines represent the theoretical CO_2 uptake if each tetraamine could capture two CO_2 molecules and one CO_2 molecule, respectively.

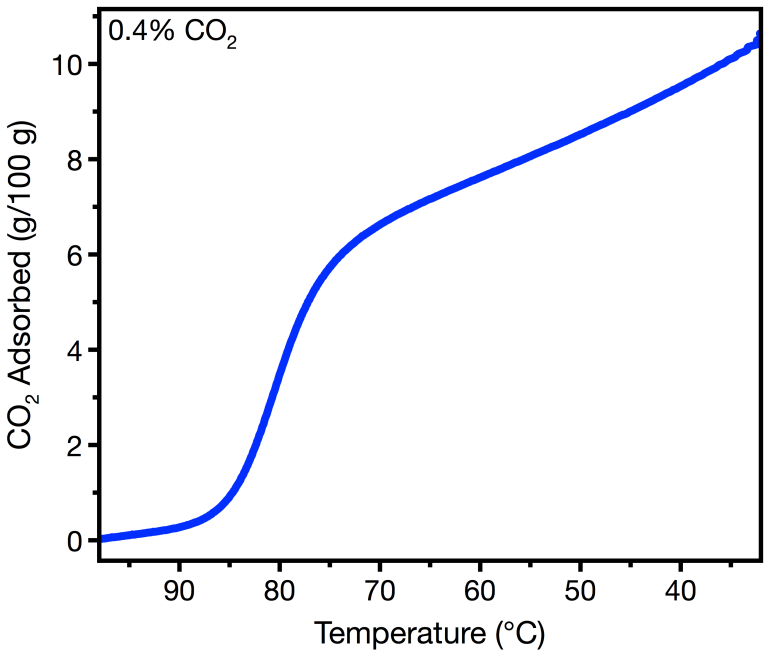

Figure S38. Thermogravimetric adsorption isobar at atmospheric pressure under 0.4% CO_2 for Mg_2(dobpdc)(3-4-3). A temperature ramp rate of 0.1 °C/min was used.

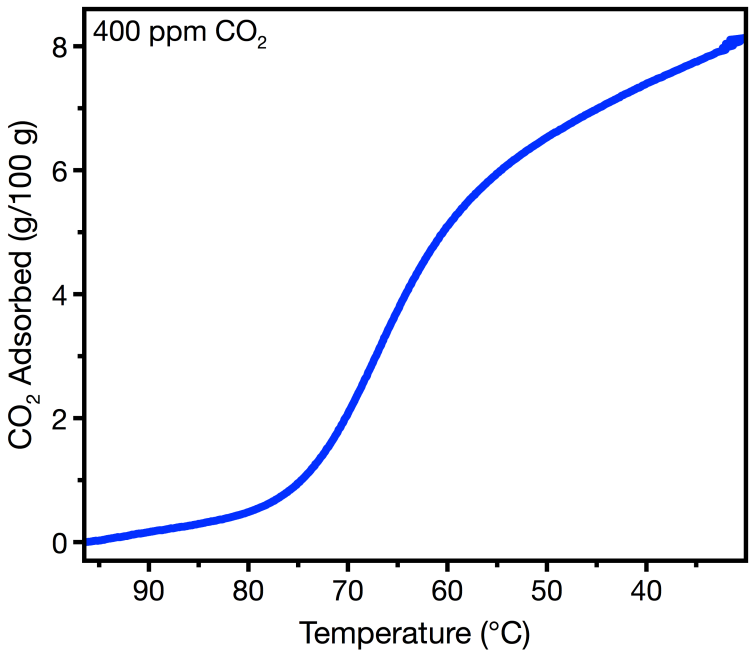

Figure S39. Thermogravimetric adsorption isobar at atmospheric pressure under 400 ppm CO_2 for Mg_2(dobpdc)(3-4-3). A temperature ramp rate of 0.1 °C/min was used.

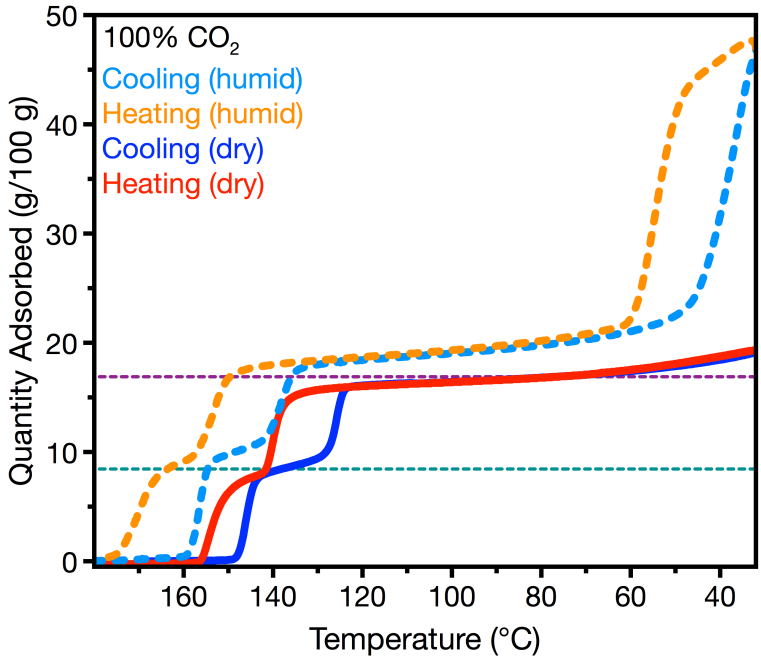

Figure S40. Pure CO_2 isobars for Mg_2(dobpdc)(3-4-3) under ~30% relative humidity with adsorption shown in light blue and desorption shown in orange. The dry pure CO_2 adsorption (blue) and desorption (red) isobars are shown for comparison. A temperature ramp rate of 1 °C/min was used. The dotted purple and teal lines represent the theoretical CO_2 uptake if each tetraamine could capture two CO_2 molecules and one CO_2 molecule, respectively.

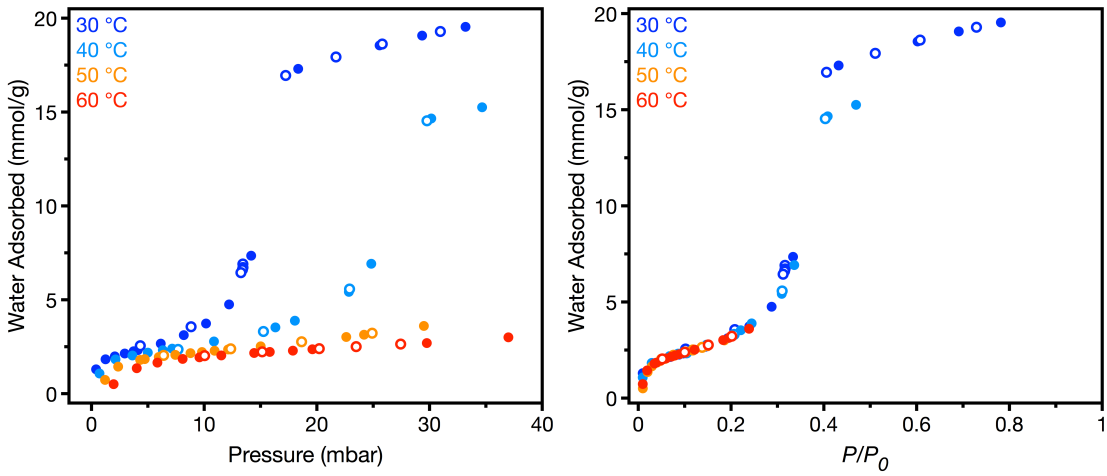

Figure S41. H_2O adsorption (filled circles) and desorption (open circles) isotherms of Mg_2(dobpdc)(3-4-3) at 30, 40, 50, and 60 °C shown with the *x*-axis in absolute (left) and relative (right) pressure.

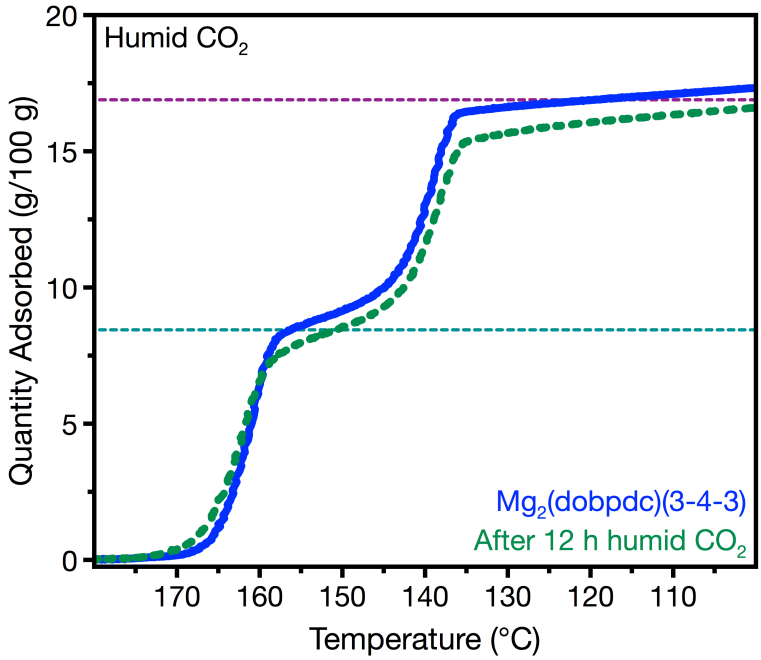

Figure S42. Humid CO_2 isobars for Mg_2(dobpdc)(3-4-3) generated by passing the CO_2 feed through a water bubbler at 25 °C. Blue and green curves represent the adsorption isobar before and after treatment under humid flowing CO_2 at 180 °C (1 atm) for 12 h, respectively. The dotted purple and teal lines represent the theoretical CO_2 uptake if each tetraamine could capture two CO_2 molecules and one CO_2 molecule, respectively. In a recent report, a similar study was performed on PEI-MCM-41, a representative amine-functionalized silica, where CO_2 adsorption isobars were collected after exposure to humid flowing CO_2 at 140 °C for 12 h and a 17% decrease in dry CO_2 adsorption capacity at 40 °C was observed (*32*).

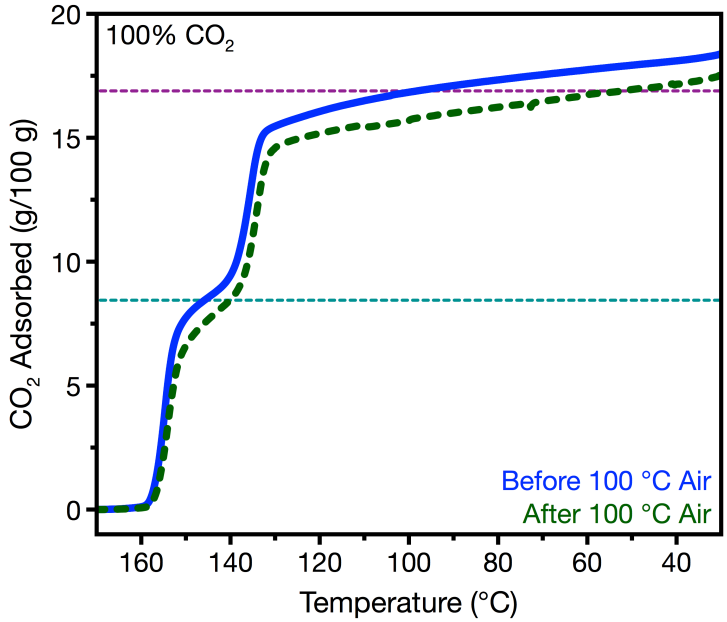

Figure S43. Pure CO_2 adsorption isobars for Mg_2(dobpdc)(3-4-3) before (blue) and after (green) treatment under flowing air at 100 °C (1 atm) for 12 h. The dotted purple and teal lines represent the theoretical CO_2 uptake if each tetraamine could capture two CO_2 molecules and one CO_2 molecule, respectively.

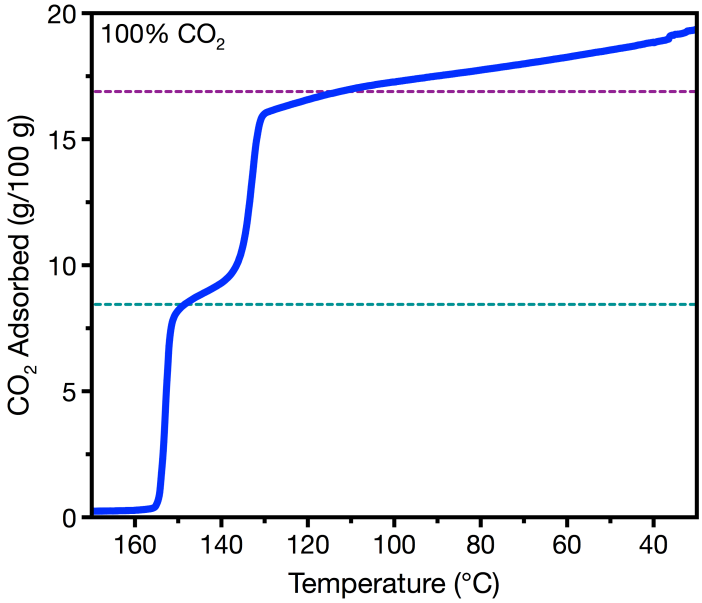

Figure S44. Pure CO_2 adsorption isobar obtained for Mg_2(dobpdc)(3-4-3) at atmospheric pressure after pelletization for breakthrough measurements. No significant change in the adsorption profile is observed after pelletization relative to the powder material (Figure S11). The dotted purple and teal lines represent the theoretical CO_2 uptake if each tetraamine could capture two CO_2 molecules and one CO_2 molecule, respectively.

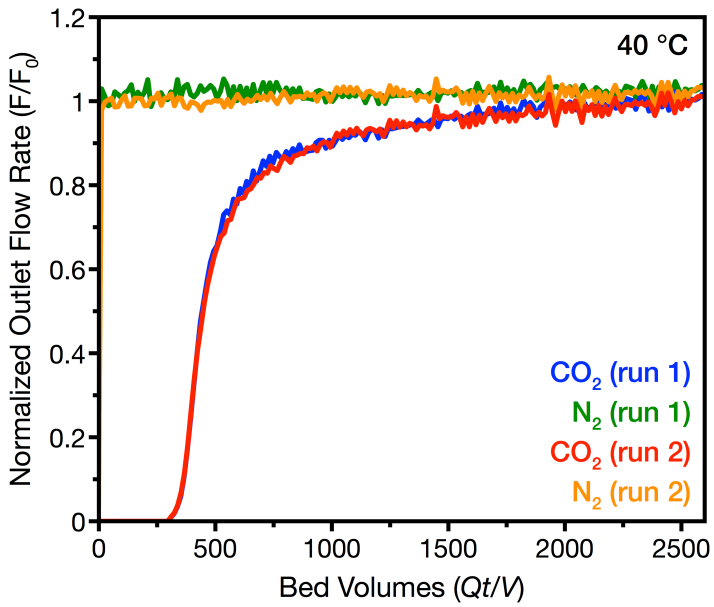

Figure S45. Breakthrough profiles for Mg_2(dobpdc)(3-4-3) under 30 sccm of dry 4% CO_2 in N_2 at 40 °C and atmospheric pressure. Data for each run were collected in succession after activation under 30 sccm of flowing He for 30 min at 140 °C prior to each breakthrough experiment to ensure that CO_2 was desorbed. Immediate breakthrough of N_2 (green and orange) is observed followed by breakthrough of CO_2 (blue and red).

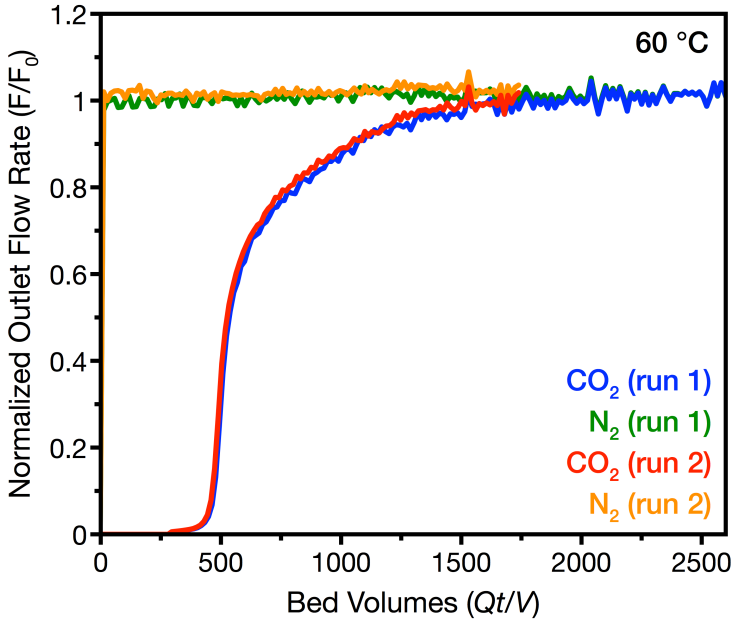

Figure S46. Breakthrough profiles for Mg_2(dobpdc)(3-4-3) under 30 sccm of dry 4% CO_2 in N_2 at 60 °C and atmospheric pressure. Data for each run were collected in succession after activation under 30 sccm of flowing He for 30 min at 140 °C prior to each breakthrough experiment to ensure that CO_2 was desorbed. Immediate breakthrough of N_2 (green and orange) is observed followed by breakthrough of CO_2 (blue and red).

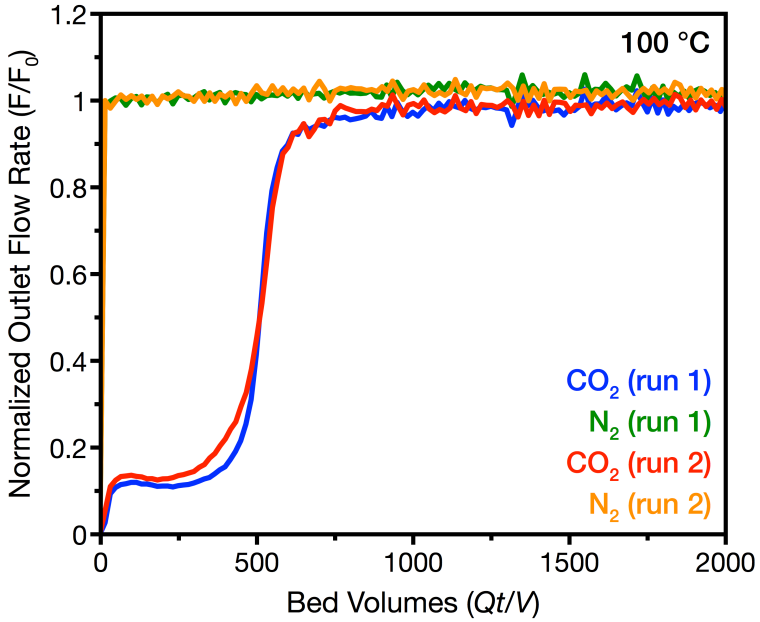

Figure S47. Breakthrough profiles for Mg_2(dobpdc)(3-4-3) under 30 sccm of dry 4% CO_2 in N_2 at 100 °C and atmospheric pressure. Data for each run were collected in succession after activation under 30 sccm of flowing He for 30 min at 140 °C prior to each breakthrough experiment to ensure that CO_2 was desorbed. Immediate breakthrough of N_2 (green and orange) is observed followed by breakthrough of CO_2 (blue and red).

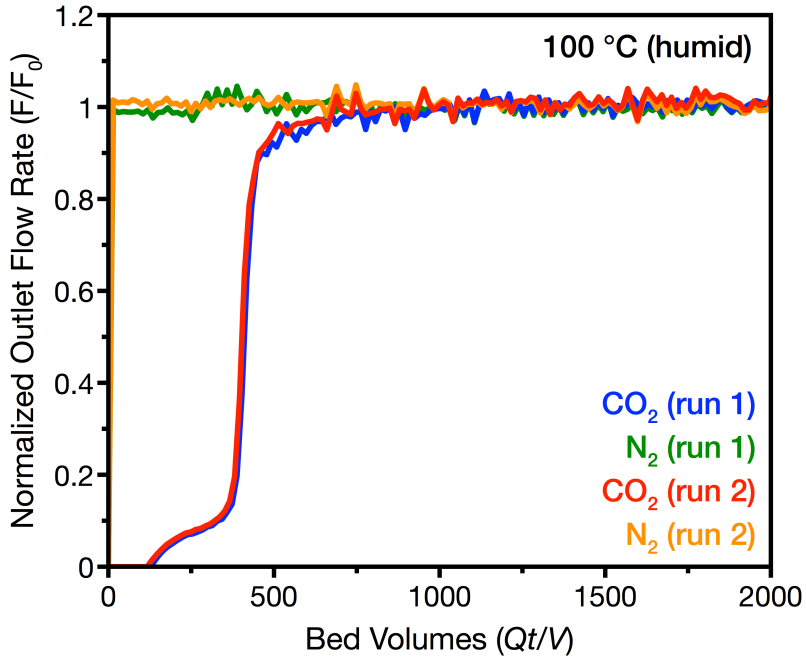

Figure S48. Breakthrough profiles for Mg_2(dobpdc)(3-4-3) under 30 sccm of humid (~2.6% H_2O) 4% CO_2 in N_2 at 100 °C and atmospheric pressure. Data for each run were collected in succession after activation under 30 sccm of flowing He for 30 min at 140 °C prior to each breakthrough experiment to ensure that CO_2 was desorbed. Immediate breakthrough of N_2 (green and orange) is observed followed by breakthrough of CO_2 (blue and red). Recently, a new diamine-appended framework, 2-ampd–Mg_2(dobpdc), was reported to possess optimal properties for CO_2 capture from NGCC emissions (*32*). In humid 4% CO_2 breakthrough experiments, we found that Mg_2(dobpdc)(3-4-3) has a similar useable CO_2 capacity at 100 °C to the capacity for 2-ampd–Mg_2(dobpdc), 2.2 ± 0.1 mmol/g, at 40 °C. Additionally, the higher adsorption temperatures possible for the 3-4-3-functionalized framework versus the 2-ampd-functionalized framework may afford enhanced process efficiency by reducing costs associated with flue gas cooling**.**

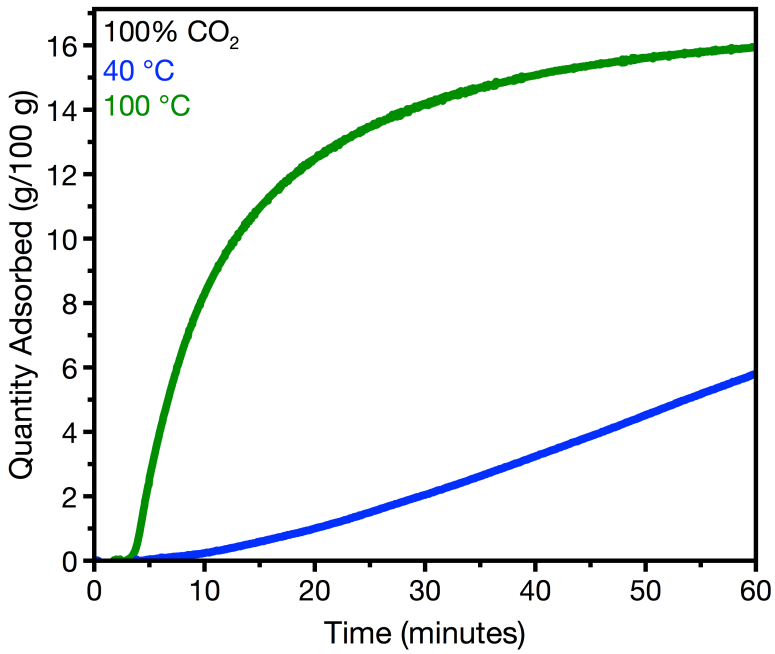

Figure S49. Humid CO_2 rate of adsorption experiments for Mg_2(dobpdc)(3-4-3) at 40 and 100 °C measured using a thermogravimetric analyzer. The sample was activated at 150 °C under nitrogen for 30 min and then cooled to temperatures of interest before switching to a humidified stream (2.6% H_2O) of CO_2 at atmospheric pressure. Hindered desorption kinetics are observed under humid conditions at 40 °C.

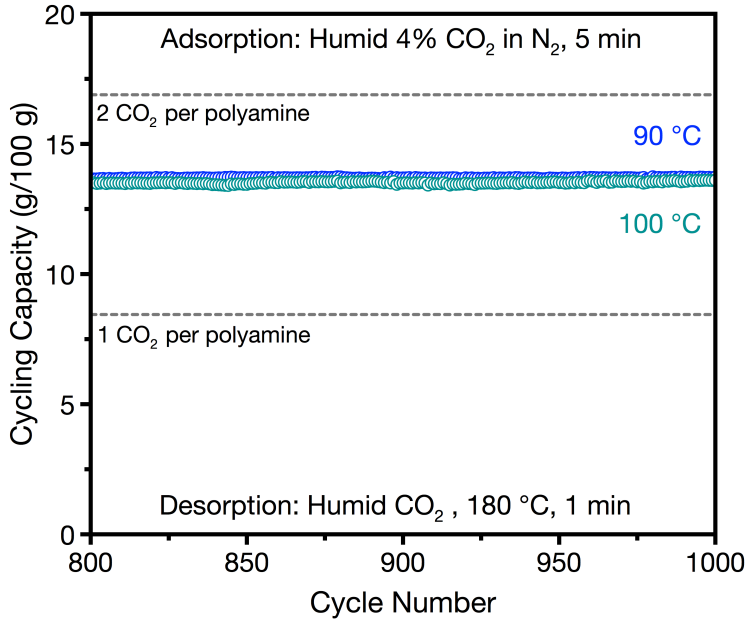

Figure S50. Extended thermogravimetric temperature-swing cycling of Mg_2(dobpdc)(3-4-3) with adsorption under humid 4% CO_2 for 5 min at 90 °C (blue) and desorption under humid 100% CO_2 at 180 °C for 1 min (~2.6% H_2O) at atmospheric pressure. Cycling with adsorption at 100 °C (teal) is shown for comparison. Ramp rates of 20°C/min were used to cycle between the adsorption and desorption temperatures. Tetraamine loading after cycling with adsorption at 90 °C and 100 °C was found to be 98 ± 5% and 100 ± 5% as determined by ^{1}H NMR spectroscopy, respectively.

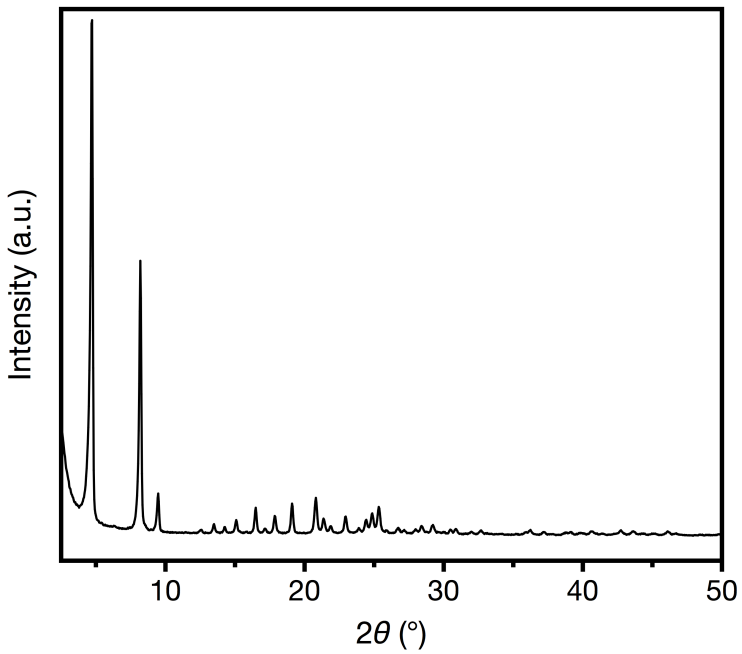

Figure S51. Powder X-ray diffraction pattern (CuKα radiation, λ = 1.5418 Å) of Mg_2(dobpdc)(3-4-3) post extended thermogravimetric temperature-swing cycling with adsorption under humid 4% CO_2 for 5 min at 100 °C (teal, Figure S50).

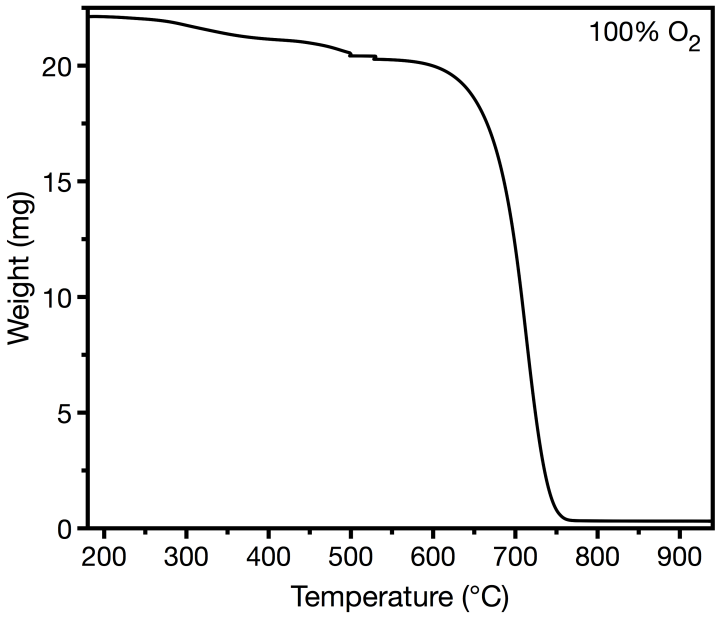

Figure S52. Thermogravimetric decomposition of the diamond+Mg_2(dobpdc)(3-4-3) mixture (15 steam cycles) under pure O_2 at atmospheric pressure.

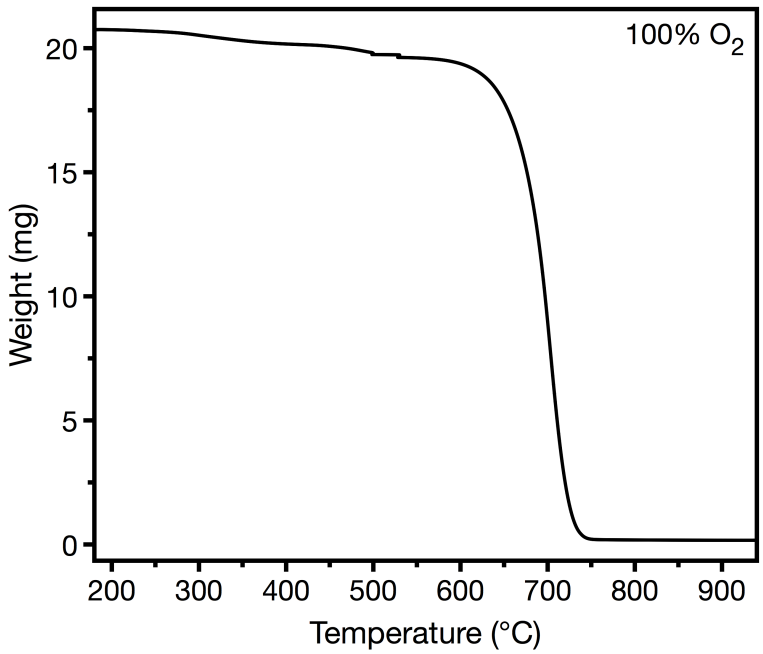

Figure S53. Thermogravimetric decomposition of the diamond+Mg_2(dobpdc)(3-4-3) mixture (5 steam cycles) under pure O_2 at atmospheric pressure.

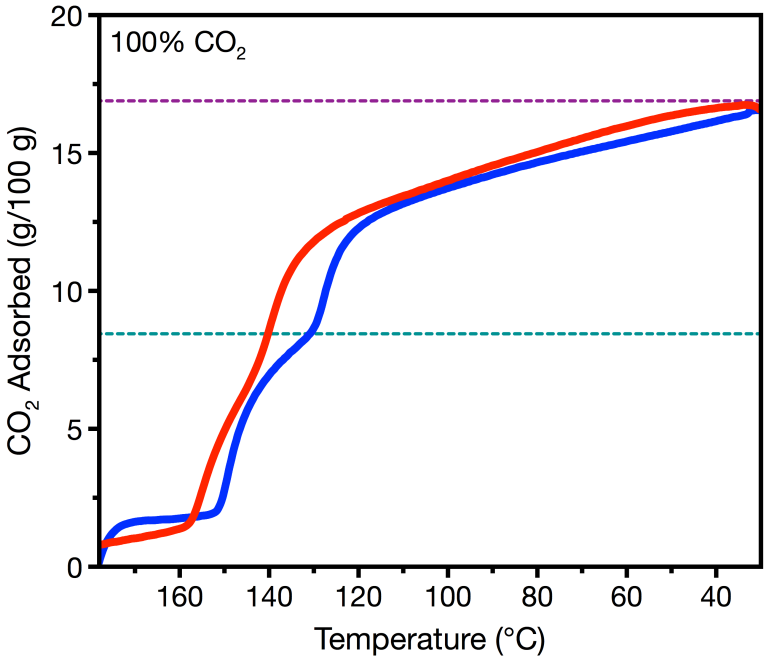

Figure S54. Pure CO_2 isobars at atmospheric pressure for the diamond+Mg_2(dobpdc)(3-4-3) mixture (collected after 15 adsorption/desorption cycles under humid conditions, as specified in the main text). The data have been normalized to the quantity of Mg_2(dobpdc)(3-4-3) in the sample. Adsorption is shown in blue and desorption is shown in red. The dotted purple and teal lines represent the theoretical CO_2 uptake if each tetraamine could capture two CO_2 molecules and one CO_2 molecule, respectively.

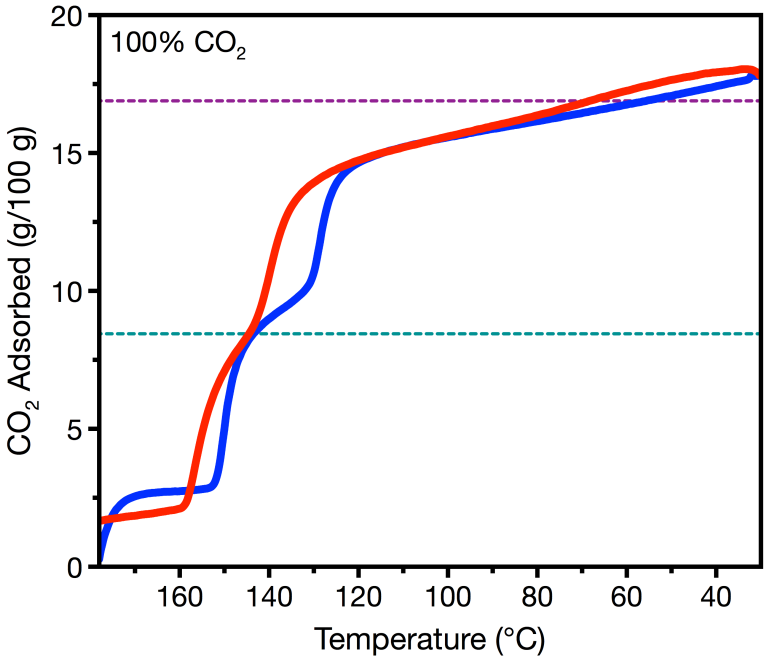

Figure S55. Pure CO_2 isobars at atmospheric pressure for the diamond+Mg_2(dobpdc)(3-4-3) mixture (5 steam cycles) that have been corrected to the amount of Mg_2(dobpdc)(3-4-3) in the mixture. Adsorption is shown in blue and desorption is shown in red. The dotted purple and teal lines represent the theoretical CO_2 uptake if each tetraamine could capture two CO_2 molecules and one CO_2 molecule, respectively.

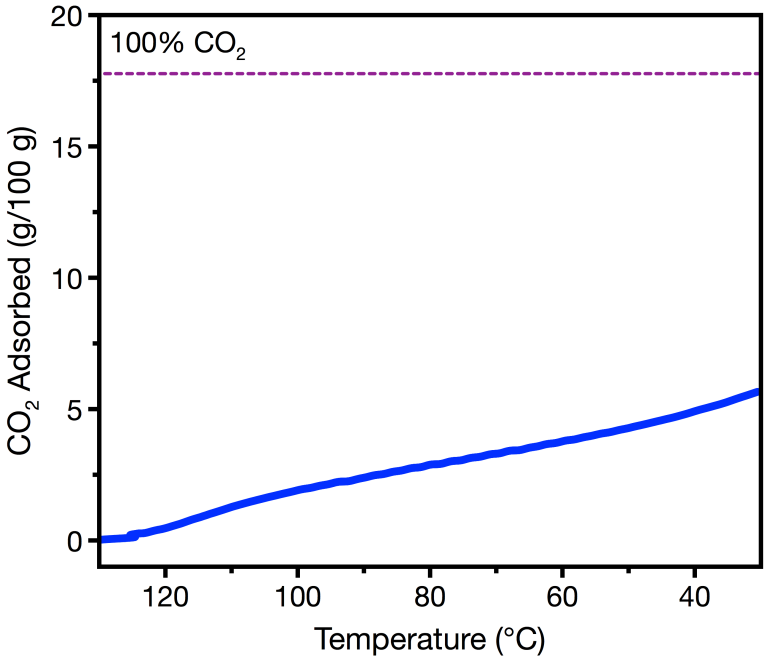

Figure S56. The pure CO_2 adsorption isobar at atmospheric pressure for the diamond+Mg_2(dobpdc)(e-2)$_2$ mixture after 5 steam cycles. Due to clear decomposition of the sample (no adsorption step is observed), the exact amount of Mg_2(dobpdc)(e-2)$_2$ was not quantified. The dotted purple line represents the theoretical CO_2 uptake for this material.

Table S1. Abbreviations, names, and structures of tetraamines used in this study.

Abbreviation	Name	Structure
2-2-2	triethylenetetramine	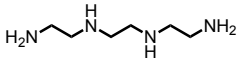
2-3-2	*N,N′*-bis(2-aminoethyl)-1,3-propanediamine	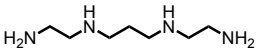
3-2-3	*1,2*-bis(3-aminopropylamino)ethane	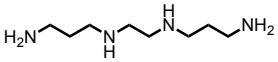
3-3-3	*N,N′*-bis(3-aminopropyl)-1,3-diaminopropane	
3-4-3	*N,N′*-bis(3-aminopropyl)-1,4-diaminobutane	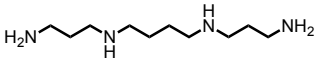
3-3	diethylenetriamine	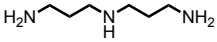
3-4	*N*-(3-aminopropyl)-1,4-diaminobutane	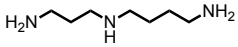

Table S2. Tetraamine loadings following synthesis and after material activation (thermal activation at temperatures obtained from thermogravimetric decomposition studies, Figures S3 and S4). Loadings were determined by ^{1}H NMR analysis following digestion of the Mg_2(dobpdc)(tetraamine) materials as outlined under "General Procedures" and "Synthesis of Tetraamine-Appended Mg_2(dobpdc)" above. Loadings were determined by comparing tetraamine peaks to framework ligand peaks (error is estimated to be ± 5%).

	Activation Temperature (°C)	**As-Synthesized Loading (% per 2 Mg^{2+})**	**Post-Activation Loading (% per 2 Mg^{2+})**
2-2-2	225	284%	98%
2-3-2	225	238%	100%
3-2-3	240	182%	106%
3-3-3	225	156%	106%
3-4-3	240	148%	94%
3-3	200	237%	114%
3-4	200	233%	103%

Table S3. Experimental conditions, unit cell parameters, and figures-of-merit as determined by performing a structureless Pawley refinement of powder X-ray diffraction patterns of 2-2-2 and 2-3-2 functionalized Mg_2(dobpdc) activated and dosed with CO_2.

	2-2-2 activated	2-2-2 CO_2-dosed	2-3-2 activated	2-3-2 CO_2-dosed
λ (Å)	0.45118	0.45118	0.45399	0.45399
Temp. (K)	300	300	300	300
Space Group	$P3_221$	$P3_221$	$P3_221$	$P3_221$
a, b (Å)	21.332(3)	21.329(3)	21.5930(9)	21.6269(13)
c (Å)	6.911(1)	6.9068(13)	6.931(4)	6.8474(7)
α, β, γ (°)	90, 90, 120	90, 90, 120	90, 90, 120	90, 90, 120
V (Å^3)	2723.5(8)	2721.1(8)	2798.8(3)	2773.6(4)
R_{wp}	2.198%	2.110%	2.189%	2.239%
R_{exp}	1.403%	1.398%	2.132%	2.087%
R_p	1.479%	1.425%	1.539%	1.577%
GoF	1.566	1.509	1.027	1.073

Table S4. Experimental conditions, unit cell parameters, and figures-of-merit as determined by performing a structureless Pawley refinement of powder X-ray diffraction patterns of 3-2-3, 3-3-3, and 3-4-3 functionalized Mg_2(dobpdc) activated and dosed with CO_2.

	3-2-3 activated	3-2-3 CO_2-dosed	3-3-3 activated	3-3-3 CO_2-dosed	3-4-3 activated	3-4-3 CO_2-dosed
λ (Å)	0.45399	0.45399	0.45118	0.45118	0.45399	0.45399
Temp. (K)	300	300	300	300	300	300
Space Group	$P3_221$	$P3_221$	$P3_221$	$P3_221$	$P3_221$	$P3_221$
a, b (Å)	21.6145(11)	21.562(5)	21.7195(11)	21.5308(11)	21.6988(12)	21.5752(8)
c (Å)	6.9369(4)	6.9281(7)	6.9035(8)	6.92570(10)	6.9356(6)	6.9888(4)
α, β, γ (°)	90, 90, 120	90, 90, 120	90, 90, 120	90, 90, 120	90, 90, 120	90, 90, 120
V (Å^3)	2806.6(4)	2790(2)	2820.3(4)	2780.5(5)	2828.0(4)	2817.4(3)
R_{wp}	2.649%	2.840%	3.632%	3.165%	3.329%	2.695%
R_{exp}	4.563%	1.881%	1.801%	1.795%	1.638%	1.687%
R_p	1.919%	1.999%	2.341%	2.088%	2.077%	1.769%
GoF	0.581	1.510	2.016	1.763	2.032	1.598

Table S5. Experimental conditions, unit cell parameters, and figures-of-merit as determined by performing a structureless Pawley refinement of powder X-ray diffraction patterns of 3-3- and 3-4-functionalized Mg_2(dobpdc) activated and dosed with CO_2.

	3-3 activated	3-3 CO_2-dosed	3-4 activated	3-4 CO_2-dosed
λ (Å)	0.45118	0.45118	0.45118	0.45118
Temp. (K)	300	300	300	300
Space Group	$P3_221$	$P3_1$	$P3_221$	$P3_1$
a, b (Å)	21.2887(19)	21.256(2)	21.3465(9)	21.5413(13)
c (Å)	6.9328(10)	6.9344(12)	6.9299(7)	6.9232(9)
α, β, γ (°)	90, 90, 120	90, 90, 120	90, 90, 120	90, 90, 120
V (Å^3)	2721.1(6)	2713.3(7)	2734.7(4)	2782.2(5)
R_{wp}	2.738%	2.601%	3.054%	3.542%
R_{exp}	1.777%	1.612%	2.819%	1.597%
R_p	1.925%	1.840%	2.025%	2.313%
GoF	1.541	1.614	1.083	2.218

Table S6. Experimental, unit cell, and refinement parameters obtained by Pawley refinement using synchrotron X-ray powder diffraction patterns of Mg_2(dobpdc)(3-4-3) dosed with CO_2 gas, at varying temperatures.

	Pre-step	1st step	2nd step
l (Å)	0.45415	0.45415	0.45415
Temp. (K)	453	424	415
Space Group	$P3_221$	$P3_221$	$P3_221$
a, b (Å)	21.665(10)	21.6653(16)	21.6017(16)
c (Å)	6.9279(3)	6.9100(5)	6.9622(5)
α, β, γ (°)	90, 90, 120	90, 90, 120	90, 90, 120
V (Å^3)	2816(2)	2808.9(5)	2813.6(5)
R_{wp}	2.223%	2.565%	2.485%
R_{exp}	2.186%	2.076%	2.073%
R_p	1.509%	1.780%	1.646%
GoF	1.017	1.236	1.199

Table S7. Parameters for DFT-optimized structures of Mg_2(dobpdc)(3-4-3), Mg_2(dobpdc)(3-4-3)(CO_2), and Mg_2(dobpdc)(3-4-3)$(CO_2)_2$. Experimentally determined Δh_{ads} were averaged over a loading of 0–1.8 mmol/g CO_2 for Mg_2(dobpdc)(3-4-3)(CO_2) and 1.8–3.6 mmol/g of Mg_2(dobpdc)(3-4-3)$(CO_2)_2$.

	a, b (Å)	*c* (Å)	Volume (Å^3)	ΔE_{ads} (kJ/mol)	Experimental Δh_{ads} (kJ/mol)
Mg_2(dobpdc)(3-4-3)	21.9061	6.8787	2858.71		
Mg_2(dobpdc)(3-4-3)(CO_2)	21.7679	7.0334	2886.23	−84	−95.7±4.0
Mg_2(dobpdc)(3-4-3)$(CO_2)_2$	21.3927	7.2339	2867.05	−60	−70.4±4.6

Table S8. Experimental and vdW-corrected DFT-Calculated Chemical Shifts of Mg_2(dobpdc)(3-4-3)$(CO_2)_2$.

	Iso_σ	Experimental Chemical Shift (ppm)	Calculated Chemical Shift (ppm)
δ^{13}C: **C**OO$^-$	5.1	165.2	162.6
δ^{1}H: HN**H**–COO$^-$	−17.3	14.1	14.5
δ^{1}H: N**H**COO$^-$	−25.2	6.2	4.0
δ^{15}N: **N**H	−124.6	91.3	86
δ^{15}N: **N**H_2	−158.6	57.3	50

Table S9. Experimental conditions, unit cell parameters, and figures-of-merit as determined by Rietveld refinement of powder X-ray diffraction patterns of Mg_2(dobpdc)(3-4-3) activated and under 1 bar of CO_2 gas.

Mg_2(dobpdc)(3-4-3)	Activated	Dosed with CO_2
λ (Å)	0.45415	0.45415
Temp. (C)	30	30
Space Group	$P3_121$	$P3_121$
a, b (Å)	21.6975(14)	21.569(3)
c (Å)	6.9008(6)	6.9679(10)
V (Å^3)	2813.5 (4)	2807.3(10)
R_{wp}	4.58%	7.04%
R_{exp}	3.08%	4.54%
R_p	2.45%	2.31%
R_{Bragg}	0.96%	3.36%
GoF	1.87	3.05

Table S10. Steam content was calculated by collecting condensed water vapor blown through the system at an outlet downstream of the IR cell. The amount of water was determined gravimetrically, then converted into an approximate gas phase volume and matched with the flow rate of carrier gas to determine steam content. As the flow rate of carrier gas varied throughout the course of the experiment, ranges were determined. The upper and lower bounds were then averaged (weighted by the number of cycles performed) to determine the average bounds.

	Cycles		**Average**
	5	**15**	
Time (minutes)	120	405	
H_2O lost (mL)	3.4	20	
H_2O lost (mole)	0.19	1.1	
Steam generated (mL)	4200	25000	
Steam flow rate (sccm)	35	61	
Carrier flow rate low (sccm)	25	25	
Carrier flow rate high (sccm)	45	45	
Steam % low	44	58	51
Steam % high	59	71	65

Table S11. Quantification of Mg_2(dobpdc)(3-4-3) in the mixture of diamond+Mg_2(dobpdc)(3-4-3) using thermogravimetric decomposition data.

	Cycles	
	5	**15**
diamond+Mg_2(dobpdc)(3-4-3) (weight)	20.75	22.13
MgO+diamond (weight)	19.74	20.51
MgO (weight)	0.17	0.31
diamond (weight)	19.57	20.19
Mg_2(dobpdc)(3-4-3) (weight)	1.18	1.94
% Mg_2(dobpdc)(3-4-3) in sample	5.69	8.75

Table S12. Tetraamine loadings of Mg_2(dobpdc)(3-4-3) after steam cycling were determined by ^{1}H NMR following digestion of the Mg_2(dobpdc)(3-4-3) materials as outlined above. Loadings are determined by comparing tetraamine peaks to framework ligand peaks and error is estimated to be ± 5%.

Steam Cycles	**3-4-3 Loading (% per 2 Mg^{2+})**
0	102
5	102
15	101

Table S13. Diamine loadings of $Mg_2(dobpdc)(e\text{-}2)_2$ after steam cycling were determined by ^1H NMR following digestion of the $Mg_2(dobpdc)(e\text{-}2)_2$ materials as outlined above. Loadings are determined by comparing tetraamine peaks to framework ligand peaks and error is estimated to be ± 5%.

Steam Cycles	e-2 Loading (% per Mg^{2+})
0	100
1	67
5	40

Table S14. Experimental conditions and relevant crystallographic data from single-crystal X-ray diffraction.

	$Zn_2(dobpdc)(3\text{-}3\text{-}3)_{0.423}$	$Zn_2(dobpdc)(3\text{-}4\text{-}3)_{0.847}$
Formula	$C_{17.81}H_{16.15}N_{1.69}O_6Zn_2$	$C_{22.47}H_{28.02}N_{3.39}O_6Zn_2$
Temperature (K)	100(2)	100(2)
Crystal System	Trigonal	Trigonal
Space Group	$P3_121$	$P3_221$
a, b, c (Å)	21.6453(9), 21.6453(9), 6.8099(3)	21.5717(6), 21.5717(6), 6.8266(2)
α, β, γ (°)	90, 90, 120	90, 90, 120
V (Å^3)	2763.1(3)	2751.08(17)
Z	3	3
Radiation, λ (Å)	Synchrotron, 0.7293	Synchrotron, 0.7288
2Θ Range for Data Collection (°)	3.862 to 62.890	4.472 to 56.472
Completeness to 2Θ	99.5% (2Θ = 51.900°)	99.9% (2Θ = 51.860°)
Data / Restraints / Parameters	5660 / 0 / 160	4209 / 35 / 182
Goodness of Fit on F^2	1.039	1.159
R_1[a], wR_2[b] (I>2σ(I))	0.0421, 0.1182	0.0824, 0.2200
R_1[a], wR_2[b] (all data)	0.0455, 0.1199	0.0925, 0.2266
Largest Diff. Peak and Hole (e Å^{-3})	0.768 and −0.572	1.775 and −0.797

[a]$R_1 = \sum||F_o| - |F_c||/\sum|F_o|$. [b]$wR_2 = \{\sum[w(F_o^2 - F_c^2)^2]/\sum[w(F_o^2)^2]\}^{1/2}$.

References

39. Bruker Analytical X-ray Systems Inc., SAINT, APEX2, and APEX3 Software for CCD Diffractometers.
40. G. M. Sheldrick, SADABS; University of Göttingen: Göttingen, Germany (1996).
41. G. M. Sheldrick, SHELXT - Integrated space-group and crystal-structure determination. *Acta Cryst. A*. **71**, 3–8 (2015).
42. G. M. Sheldrick, Crystal structure refinement with SHELXL. *Acta Cryst. C.* **71**, 3–8 (2015).
43. O. V. Dolomanov, L. J. Bourhis, R. J. Gildea, J. A. K. Howard, H. Puschmann, OLEX2: a complete structure solution, refinement and analysis program. *J. Appl. Crystallogr.* **42**, 339–341 (2009).
44. S. Øien-Ødegaard, G. C. Shearer, D. S. Wragg, K. P. Lillerud, Pitfalls in metal–organic framework crystallography: towards more accurate crystal structures. *Chem. Soc. Rev.* **50**, 4867–4876 (2017).
45. S. Lee, H.-B. Bürgi, S. A. Alshmimri, O. M. Yaghi, Impact of disordered guest–framework interactions on the crystallography of metal–organic frameworks. *J. Am. Chem. Soc*. **140**, 8958–8964 (2018).
46. A. Coelho, Topas Academic v4.1 (2007).
47. March, A. Mathematische Theorie Der Regelung Nach Der Korngestah Bei Affiner Deformation. *Z. Kristallogr. Cryst. Mater.* **81**, 285–297 (1932).
48. Dollase, W. A. Correction of Intensities for Preferred Orientation in Powder Diffractometry: Application of the March Model. *J. Appl. Crystallogr.* **19**, 267–272 (1986).
49. P. E. Blöchl, Projector augmented-wave method. *Phys. Rev. B*. **50**, 17953 (1994).
50. G. Kresse, D. Joubert, From ultrasoft pseudopotentials to the projector augmented-wave method. *Phys. Rev. B*. **59**, 1758–1775 (1999).
51. G. Kresse, J. Furthmüller, Efficient iterative schemes for ab initio total-energy calculations using a plane-wave basis set. *Phys. Rev. B*. **54**, 11169–11186 (1996).
52. G. Kresse, J. Furthmüller, Efficiency of ab-initio total energy calculations for metals and semiconductors using a plane-wave basis set. *Comput. Mater. Sci.* **6**, 15–50 (1996).
53. G. Kresse, J. Hafner, Ab initio molecular-dynamics simulation of the liquid-metal--amorphous-semiconductor transition in germanium. *Phys. Rev. B*. **49**, 14251–14269 (1994).
54. K. Lee, É. D. Murray, L. Kong, B. I. Lundqvist, D. C. Langreth, Higher-accuracy van der Waals density functional. *Phys. Rev. B*. **82**, 081101 (2010).
55. C. Elsässer, M. Fähnle, C. T. Chan, K. M. Ho, Density-functional energies and forces with Gaussian-broadened fractional occupations. *Phys. Rev. B*. **49**, 13975–13978 (1994).
56. C. T. Campbell, J. R. V. Sellers, Enthalpies and entropies of adsorption on well-defined oxide surfaces: experimental measurements. *Chem. Rev.* **113**, 4106–4135 (2012).
57. F. G. Helfferich, P. W. Carr, Non-Linear Waves in Chromatography. *J. Chromatogr. A.* **629**, 97–122 (1993).
58. W. Zhang, Y. Shan, A. Seidel-Morgenstern, Breakthrough Curves and Elution Profiles of Single Solutes in Case of Adsorption Isotherms with Two Inflection Points. *J. Chromatogr. A.* **1107**, 216–225 (2006).
59. M. Mazzotti, A. Rajendran, Equilibrium Theory-Based Analysis of Nonlinear Waves in Separation Processes. *Annu. Rev. Chem. Biomol. Eng.* **4**, 119–141 (2013).

60. M. Hefti, L. Joss, Z. Bjelobrk, M. Mazzotti, On the Potential of Phase-Change Adsorbents for CO_2 Capture by Temperature Swing Adsorption. *Faraday Discuss.* **192**, 153–179 (2016).
61. R. R. Krug, W. G. Hunter, R. A. Grieger, Statistical interpretation of enthalpy–entropy compensation. *Nature*. **261**, 566–567 (1976).